Università degli Studi di Roma "La Sapienza"
Dottorato di Ricerca in Fisica - XVIII Ciclo
Settore scientifico-disciplinare FIS/04

# Measurement of the angle $\gamma$ in $B^- \to D^{(*)0} K^-$ decays with the Dalitz analysis of $D^0 \to K_S \pi^+ \pi^-$

Tesi presentata da

**Luigi Li Gioi**

per il conseguimento del titolo di Dottore di Ricerca

Direttore della Ricerca:
**Prof. Fernando Ferroni**

**Dott. Riccardo Faccini**

Coordinatore del
Dottorato di Ricerca:
**Prof. Valeria Ferrari**

Anno Accademico 2004/2005

# Contents

# Introduction

The violation of the $CP$ symmetry was discovered in 1964 in the $K^0$ system and is one of the open problems in particle physics. $CP$ Violation in the Standard Model arises from the presence of an irreducible phase in the Cabibbo-Kobayashi-Maskawa ($CKM$) quark mixing matrix. The unitarity condition of the $CKM$ matrix can be written as a sum of three complex numbers equal to zero, that can be presented in a form of a triangle, called the "Unitarity Triangle", in the complex plane. The fact that the area of the Unitarity Triangle is different from zero is equivalent to the presence of $CP$ violation in the Standard Model.

$CP$ violation in the $B$ meson system has been clearly established in recent years. Although these results are in good agreement with the Standard Model expectations, other and more precise measurements of $CP$ violation in $B$ decays are needed to over-constrain the Cabibbo-Kobayashi-Maskawa quark mixing matrix and search for new physics effects. The angle $\gamma$ of the Unitarity Triangle of the $CKM$ matrix constitutes one of these crucial measurements.

Various methods using $B^- \to \tilde{D}^0 K^-$ decays have been proposed to measure $\gamma$. Here, $\tilde{D}$ indicates either a $D^0$ or a $\bar{D}^0$ meson. All methods exploit the fact that a $B^-$ can decay into a $D^0 K^-$ ($\bar{D}^0 K^-$) final state via $b \to c\bar{u}s$ ($b \to u\bar{c}s$) transitions. These decay amplitudes interfere when the $D^0$ and $\bar{D}^0$ decay into the same final state, which can lead to different $B^+$ and $B^-$ decay rates (direct $CP$ violation).

In this thesis a measurement of $\gamma$ in $B^- \to \tilde{D}^0 K^-$ decay with the Dalitz analysis of $\tilde{D}^0 \to K_S \pi^- \pi^+$ is presented. The primary advantage of this method is that it involves the entire resonant structure of the three-body $\tilde{D}$ decay, with interference of doubly Cabibbo-suppressed (DCS), Cabibbo-allowed (CA), and $CP$ eigenstate amplitudes, providing the sensitivity to $\gamma$.

The analysis is based on an integrated luminosity of 208 $fb^{-1}$ recorded at the $\Upsilon(4S)$ resonance, corresponding to $218 \cdot 10^6$ $B\bar{B}$ couples, and 21.6 $fb^{-1}$ collected at a center-

of-mass energy 40 MeV below with the *BaBar* detector at the SLAC PEP-II $e^+e^-$ asymmetric-energy $B$ Factory.

The $B^\mp \to \tilde{D}^0 K^\mp$, $\tilde{D}^0 \to K_S\pi^-\pi^+$ decay chains amplitudes $\mathcal{A}_\mp(m_-^2, m_+^2)$ can be written as

$$\mathcal{A}_\mp(m_-^2, m_+^2) = \mathcal{A}_{B\mp}(B^\mp \to \tilde{D}^0 K^\mp) \left[\mathcal{A}_D(m_\mp^2, m_\pm^2) + r_B e^{i(\delta \mp \gamma)} \mathcal{A}_D(m_\pm^2, m_\mp^2)\right] ,$$

where $m_-^2$ and $m_+^2$ are the squared invariant masses of the $K_S\pi^-$ and $K_S\pi^+$ combinations, respectively, $\mathcal{A}_{B\mp}$ is the $B^\mp \to \tilde{D}^0 K^\mp$ decay amplitude and $\mathcal{A}_D(m_-^2, m_+^2)$ is the $D^0 \to K_S\pi^-\pi^+$ decay amplitude. Here $r_B$ and $\delta$ are the amplitudes ratio and relative strong phase between the amplitudes $B^- \to \bar{D}^0 K^-$ and $B^- \to D^0 K^-$.

The $D^0$ decay amplitude $\mathcal{A}_D(m_-^2, m_+^2)$ is determined through a Dalitz analysis of a high-statistics sample of tagged $D^0$ mesons from inclusive $D^{*+} \to D^0\pi^+$ decays reconstructed in data.

Two models are used to parameterize the Dalitz structure: in the first model the Dalitz amplitude is parameterized with a sum of Breit-Wigner functions (Breit-Wigner model), in the second model the $\pi\pi$ S-wave component of the Dalitz amplitude is replaced with the $K$-matrix formalism ($K$-matrix model). Even if the $K$-matrix model takes better into account the case of overlapping resonances, to extract the $CP$ parameters the Breit-Wigner model is used since the $K$-matrix model is still preliminary and lacks a complete evaluation of the systematic error. The $K$-matrix model is used in this analysis to evaluate the contribution to the systematic error coming from the parameterization of the $\pi\pi$ S-wave of the Dalitz amplitude and in particular from the introduction of the non-established resonances $\sigma$ and $\sigma'$.

Having determined $\mathcal{A}_D(m_-^2, m_+^2)$, the $CP$ parameters are extracted with a simultaneous fit to the $|\mathcal{A}_-(m_-^2, m_+^2)|^2$ and $|\mathcal{A}_+(m_-^2, m_+^2)|^2$ distributions for the $B^\mp \to \tilde{D}^0 K^\mp$ sample. Both frequentist and Bayesian approach are used.

# Chapter 1

# $CKM$ angle $\gamma$ and $B^{\pm} \to D^{(*)0} K^{(*)\pm}$ decays

Forty years after its discovery in $K^0$ system [1], the violation of the $CP$ symmetry is one of the open problems in particle physics. $CP$ violation in the Standard Model arises from the presence of an irreducible phase in the Cabibbo-Kobayashi-Maskawa ($CKM$) quark mixing matrix. The unitarity condition of the $CKM$ matrix can be written as a sum of three complex numbers equal to zero, that can be presented in a form of a triangle, called the "Unitarity Triangle", in the complex plane. In recent years the $CP$ violation in the $B$ meson system has been clearly established [2], and although there is good agreement with the expectations of the Standard Model, further measurements of $CP$ violation in $B$ decays are needed to over-constrain the Unitarity Triangle and look for New Physics effects. Among those a crucial test will be represented by the measurement of $\gamma$.

## 1.1 $CP$ violation in the Standard Model

The electroweak sector of the Standard Model is a gauge theory based on the local group $SU_L(2) \otimes U_Y(1)$, which describes the symmetries of the matter fields. The Yang-Mills electroweak Lagrangian is [3]:

$$\mathcal{L} = -\frac{1}{4}\Sigma_A W^A_{\mu\nu} W^{A\mu\nu} - \frac{1}{4} B_{\mu\nu} B^{\mu\nu} + \bar{\Psi}_L i\gamma^\mu \mathcal{D}_\mu \Psi_L + \bar{\Psi}_R i\gamma^\mu \mathcal{D}_\mu \Psi_R \ , \tag{1.1}$$

where the spinors $\Psi_L$ and $\Psi_R$ represent the matter fields in their chiral components, and the field strength tensors are given by:

$$W^A_{\mu\nu} = \partial_\mu W^A_\nu - \partial_\nu W^A_\mu - g\epsilon_{ABC} W^B_\mu W^C_\nu \ \text{ and } \ B_{\mu\nu} = \partial_\mu B_\nu - \partial_\nu B_\mu \ . \tag{1.2}$$

| Family | | | Quantum Numbers | | | |
|---|---|---|---|---|---|---|
| 1 | 2 | 3 | $T$ | $T_3$ | $Y$ | $Q = Y/2 + T_3$ |
| $\begin{pmatrix} \nu_e \\ e \end{pmatrix}_L$ | $\begin{pmatrix} \nu_\mu \\ \mu \end{pmatrix}_L$ | $\begin{pmatrix} \nu_\tau \\ \tau \end{pmatrix}_L$ | 1/2 | +1/2 | −1 | 0 |
| | | | 1/2 | −1/2 | −1 | −1 |
| $e_R$ | $\mu_R$ | $\tau_R$ | 0 | 0 | −2 | −1 |
| $\begin{pmatrix} u \\ d \end{pmatrix}_L$ | $\begin{pmatrix} c \\ s \end{pmatrix}_L$ | $\begin{pmatrix} t \\ b \end{pmatrix}_L$ | 1/2 | +1/2 | +1/3 | +2/3 |
| | | | 1/2 | −1/2 | +1/3 | −1/3 |
| $u_R$ | $c_R$ | $t_R$ | 0 | 0 | 4/3 | +2/3 |
| $d_R$ | $s_R$ | $b_R$ | 0 | 0 | −2/3 | −1/3 |

Table 1.1: *Electroweak interaction multiplets.*

Here $W^A$ and $B$ are the SU(2) and U(1) gauge fields, with the coupling constants $g$ and $g'$, and $\epsilon_{ABC}$ is the totally anti-symmetric Levi-Civita tensor. The corresponding covariant derivate is:

$$\mathcal{D}_\mu \Psi_{L,R} = \left[ \partial_\mu + ig \Sigma t^A_{L,R} W_{A\mu} + ig' \frac{1}{2} Y_{L,R} B_\mu \right] \Psi_{L,R} \ , \tag{1.3}$$

where $t^A_{L,R}$ and $1/2 Y_{L,R}$ are the SU(2) (weak isospin) and U(1) (hypercharge) generators. The electric charge generator is related to the isospin and hypercharge by:

$$Q = t^3_L + \frac{1}{2} Y_L = t^3_R + \frac{1}{2} Y_R \ . \tag{1.4}$$

The left and the right fermion components have different properties under the gauge group: the left components behave as doublets while the right as singlets. In the symmetric limit the two chiral component cannot interact each other, and thus mass term for fermions (of the form $\bar{\Psi}_L \Psi_R$) are forbidden. To give mass terms to fermions as well as to gauge bosons, the electroweak theory is realized with a vacuum state only invariant under the $U_{EM}(1)$ electric charge gauge transformation (spontaneous symmetry breaking) [4].

Since the $SU_L(2) \otimes U_Y(1)$ symmetry is spontaneously broken into $U_{EM}(1)$, only the linear combination of gauge fields with the quantum numbers of the photon remains massless. A general linear combination between the gauge bosons associated to the generator in Eq. 1.4 can be written:

$$\begin{pmatrix} A_\mu \\ Z_\mu \end{pmatrix} = \begin{pmatrix} -\sin\theta_W & \cos\theta_W \\ \cos\theta_W & \sin\theta_W \end{pmatrix} \begin{pmatrix} W^3_\mu \\ B_\mu \end{pmatrix} \tag{1.5}$$

where the angle $\theta_W$ is known as the Weak or Weinberg mixing angle. Once the symmetry is spontaneously broken through the interaction with the Higgs field, $A_\mu$ remains massless

while $Z_\mu$, $W_\mu^+$ and $W_\mu^-$ acquire a mass term. $W_\mu^+$ and $W_\mu^-$ are defined as:

$$W_\mu^\pm = \frac{1}{\sqrt{2}}(W_\mu^1 \pm iW_\mu^2) \ . \tag{1.6}$$

The bilinear terms in the fields $Z_\mu$ and $W_\mu^\pm$ can be identified as the mass terms:

$$M_Z^2 = \frac{v^2 g^2}{2cos^2\theta_W} \ , \tag{1.7}$$

$$M_W^2 = cos^2\theta_W M_Z^2 \ , \tag{1.8}$$

which implies $\tan\theta_W = g'/gY_\phi$. In therms of these new fields the fermionic currents are:

$$J_\mu^\pm = \mathbf{\Sigma_f}\bar{\Psi}^f(1-\gamma_5)\gamma_\mu t^\pm \Psi^f \ , \tag{1.9}$$

$$J_\mu^0 = \Sigma_f \bar{\Psi}^f \gamma_\mu \left[(1-\gamma_5)t^3 - 2Q\sin^2\theta_W\right] \Psi^f \ , \tag{1.10}$$

$$J_\mu^{em} = \mathbf{\Sigma_f}\bar{\Psi}^f \gamma_\mu Q \ \Psi^f \ , \tag{1.11}$$

where $\Psi^f$ represents the isospin doublet for the fermions fields (Tab. 1.1) with $f$ acting as a family index, $(1-\gamma_5)$ is the left-handed chiral projector, and $t^\pm$ are the isospin generator associated to the fields $W^\pm$. The first current describes interactions which change the electric charge, while the other two, produce transitions charge-conserving. The Lagrangian 1.1 could be rewritten in two terms: one including interactions between the neutral current and the $A_\mu$ and $Z_\mu$ bosons, and another describing the interactions of the $W_\mu^\pm$ with the charged current:

$$\mathcal{L}_{\mathcal{ED}} = \mathcal{L}_{\mathcal{CC}} + \mathcal{L}_{\mathcal{NC}} \ , \tag{1.12}$$

$$\mathcal{L}_{\mathcal{CC}} = \frac{g_2}{2\sqrt{2}}(J_\mu^+ W_\mu^+ + J_\mu^- W_\mu^-) \ , \tag{1.13}$$

$$\mathcal{L}_{\mathcal{NC}} = -eJ_\mu^{em}A^\mu + \frac{g_2}{2\cos\theta_W}J_\mu^0 Z^\mu \ , \tag{1.14}$$

where $e$ is defined as $e = g_2\sin\theta_W$.

Starting from the same doublet which gives masses to the gauge bosons it is possible to introduce mass terms for the fermion fields. This imposes others restrictions on the Higgs field. To obtain fermion mass terms like:

$$-\bar{\Psi}_L\Gamma\Psi_R\phi - \bar{\Psi}_R\Gamma\Psi_L\tilde{\phi} \quad \text{where} \quad \tilde{\phi} = i\sigma^2\phi^\dagger \tag{1.15}$$

invariant under $SU_{L,R}(2)$ transformations, the Higgs field is required to have isospin equal to 1/2. The $\Gamma$ matrices contain the Yukawa constants, which determine the strength of the fermion couplings to the Higgs fields.

The fermion mass matrix is obtained from the Yukawa couplings expanding $\phi$ around the vacuum state:

$$M = \bar{\psi}_L \, \mathcal{M} \psi_R + \bar{\psi}_R \mathcal{M}^{\dagger} \psi_L \tag{1.16}$$

with

$$\mathcal{M} = \Gamma \cdot v \ . \tag{1.17}$$

It is important to observe that by a suitable change of basis it is always possible to make the matrix $\mathcal{M}$ Hermitian, $\gamma_5$-free, and diagonal. In fact, it is possible to make separate unitary transformations on $\psi_L$ and $\psi_R$ according to

$$\psi'_L = L\psi_L, \quad \psi'_R = R\psi_R \ , \tag{1.18}$$

and consequently

$$\mathcal{M} \to \mathcal{M}' = L^{\dagger} \mathcal{M} R \ . \tag{1.19}$$

This transformation does not alter the general structure of the fermion couplings in $\mathcal{L}$.

Weak charged currents are the only tree level interactions in the SM that may induce a change of flavor. By emission of a W an up-type quark is turned into a down-type quark, or a $\nu_l$ neutrino is turned into a $l^-$ charged lepton.

Starting from an up quark that is a mass eigenstate, emission of a W turns it into a down-type quark state $d'$ (the weak isospin partner of u) that in general is not a mass eigenstate. In general, the mass eigenstates and the weak eigenstates do not in fact coincide and a unitary transformation connects the two sets:

$$\begin{pmatrix} d' \\ s' \\ b' \end{pmatrix} = V \begin{pmatrix} d \\ s \\ b \end{pmatrix} \tag{1.20}$$

V is the Cabibbo-Kobayashi-Maskawa matrix [5, 6]. Thus in terms of mass eigenstates the charged weak current of quarks is of the form:

$$J^+_{\mu} \propto \bar{u} \gamma_{\mu} (1 - \gamma_5) t^+ V d \ . \tag{1.21}$$

With three fermion generations the matrix V could be expressed in terms of three angles and one irremovable complex phase [6]. The CKM matrix is usually represented as:

$$V = \begin{pmatrix} V_{ud} & V_{us} & V_{ub} \\ V_{cd} & V_{cs} & V_{cb} \\ V_{td} & V_{ts} & V_{tb} \end{pmatrix} \tag{1.22}$$

The irremovable phase in the CKM matrix allows possible $CP$ violation.

The measurement of the elements of the CKM matrix is fundamental to test the validity of the Standard Model. Many of them (actually the first two rows of the matrix) are measured directly, namely by tree-level processes. Using unitary relations one can put constraints on the top mixing $|V_{ti}|$. Moreover the $B$ mixing measurements, that involve box diagrams, can give information also about $V_{td}$ and $V_{tb}$.

The CKM-matrix can be expressed in terms of four Wolfenstein parameters $(\lambda, A, \rho, \eta)$ with $\lambda = |V_{us}| = 0.22$ playing the role of an expansion parameter and $\eta$ representing the $CP$-violating phase [7]:

$$V = \begin{pmatrix} 1 - \frac{\lambda^2}{2} & \lambda & A\lambda^3(\bar{\rho} - i\bar{\eta}) \\ -\lambda & 1 - \frac{\lambda^2}{2} & A\lambda^2 \\ A\lambda^3(1 - \bar{\rho} - i\bar{\eta}) & -A\lambda^2 & 1 \end{pmatrix} + O(\lambda^5) \tag{1.23}$$

which clearly shows how, for small values of $\lambda = \sin(\theta_C)$, the $CKM$ matrix tends to the unitary matrix. Here an improved parameterization is used, given in [8], which is obtained replacing the parameters $\rho$ and $\eta$ with:

$$\bar{\rho} = \rho\left(1 - \frac{\lambda^2}{2}\right) \qquad \bar{\eta} = \eta\left(1 - \frac{\lambda^2}{2}\right) \tag{1.24}$$

In this way the power expansion in $\lambda$ includes also $O(\lambda^4)$ contributions, so that the deviation from the unitarity of the matrix is negligible in practice.

## 1.2 The Unitarity Triangle

The Wolfenstein parameterization offers a transparent geometrical representation of the structure of the $CKM$ matrix. The unitarity of the CKM matrix, $VV^\dagger = \mathbf{1}$, requires that for any choice of $i, j, k, l = 1, 2, 3$

$$\Im[V_{ij}V_{kl}V_{il}^*V_{kj}^*] = J\sum_{m,n=1}^{3}\epsilon_{ikm}\epsilon_{jln}\ , \tag{1.25}$$

where $J$ is called the Jarlskog invaraint. The unitarity of the matrix implies also various relations among its rows and columns. Three of them are very useful for understanding the Standard Model predictions for $CP$ violation:

$$V_{ud}V_{us}^* + V_{cd}V_{cs}^* + V_{td}V_{ts}^* = 0, \tag{1.26}$$

$$V_{us}V_{ub}^* + V_{cs}V_{cb}^* + V_{ts}V_{tb}^* = 0, \tag{1.27}$$

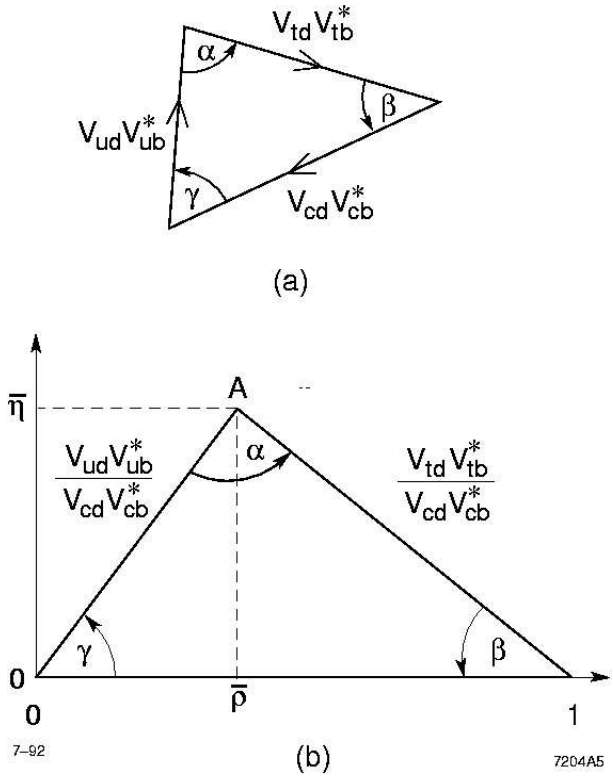


Figure 1.1: *The rescaled Unitarity Triangle, all sides divided by* $V_{cb}^* V_{cd}$.

$$V_{ud}V_{ub}^* + V_{cd}V_{cb}^* + V_{td}V_{tb}^* = 0. \tag{1.28}$$

Each of these three relations requires the sum of three complex quantities to vanish and so can be geometrically represented in the complex plane as a triangle. These are "the unitarity triangles". Eq. 1.25 implies that the all the unitarity triangles are equal in area and that the area is equal to $|J|/2$. If the $CP$ symmetry is violated the area of the triangles is not zero. The $B$ physics is related to the third triangle at least for what the B-Factories can access. The study of the parameters of this triangle encompasses the physics of $CP$ violation in Standard Model. The openness of this triangle, due to the fact that all the three sides are of the same order of magnitude, predicts large $CP$ asymmetries.

The rescaled Unitarity Triangle (Fig. 1.1) is derived from Eq. 1.28 by:

- choosing a phase convention such that $(V_{cd}V_{cb}^*)$ is real,
- dividing the lengths of all sides by $V_{cd}V_{cb}^*$,
- aligns one side of the triangle with the real axis,

- makes the length of this side 1.

The form of the triangle is unchanged. Two vertexes of the rescaled Unitarity Triangle are thus fixed at (0,0) and (1,0). The coordinates of the remaining vertex are denoted by $(\bar{\rho}, \bar{\eta})$.

This triangle is very important in $B$ Physics. Both angles and sides can be measured in a $B$ factory and they can offer an independent test of the Standard Model. The incompatibility of the new measurements with a triangle would be a proof of new Physics.

Depicting the rescaled Unitarity Triangle in the $(\bar{\rho}, \bar{\eta})$ plane, the lengths of the two complex sides are:

$$R_b \equiv \sqrt{\bar{\rho}^2 + \bar{\eta}^2} = \frac{1 - \lambda^2/2}{\lambda} \left| \frac{V_{ub}}{V_{cb}} \right| \quad R_t \equiv \sqrt{(1-\bar{\rho})^2 + \bar{\eta}^2} = \frac{1}{\lambda} \left| \frac{V_{td}}{V_{cb}} \right| \tag{1.29}$$

and the three angles are defined as:

$$\alpha \equiv \arg \left[ -\frac{V_{td} V_{tb}^*}{V_{ud} V_{ub}^*} \right] \quad \beta \equiv \arg \left[ -\frac{V_{cd} V_{cb}^*}{V_{td} V_{tb}^*} \right] \quad \gamma \equiv \arg \left[ -\frac{V_{ud} V_{ub}^*}{V_{cd} V_{cb}^*} \right] \equiv \pi - \alpha - \beta \tag{1.30}$$

It is possible to perform various independent measurements of the angles and the sides which can over-constrain the Unitarity Triangle and then test the Standard Model. Moreover, if the Standard Model holds, it is possible to obtain informations on a particular quantity from the constraints coming from the other quantities.

Various analysis exist differing mainly in the statistical approach. Fig 1.2 shows the selected $(\bar{\rho}, \bar{\eta})$ region from the approach proposed in [9]. This analysis uses a Bayesian approach and the following constraints:

- The relative rate of charmed and charmless $b$-hadron semileptonic decays which allows to measure the ratio

$$\left| \frac{V_{ub}}{V_{cb}} \right| = \frac{\lambda}{1 - \frac{\lambda^2}{2}} \sqrt{\bar{\rho}^2 + \bar{\eta}^2} \, . \tag{1.31}$$

  The constraint from this quantity results in a circle in the plane centered at $(0, 0)$.

- The $B_d^0 - \bar{B}_d^0$ time oscillation period which can be related to the mass difference between the light and heavy mass eigenstates of the $B_d^0 - \bar{B}_d^0$ system

$$\Delta m_d = \frac{G_F^2}{6\pi^2} m_W^2 \; \eta_c S(x_t) \; A^2 \lambda^6 \; [(1-\bar{\rho})^2 + \bar{\eta}^2] \; m_{B_d} \; f_{B_d}^2 \hat{B}_{B_d} \; , \tag{1.32}$$

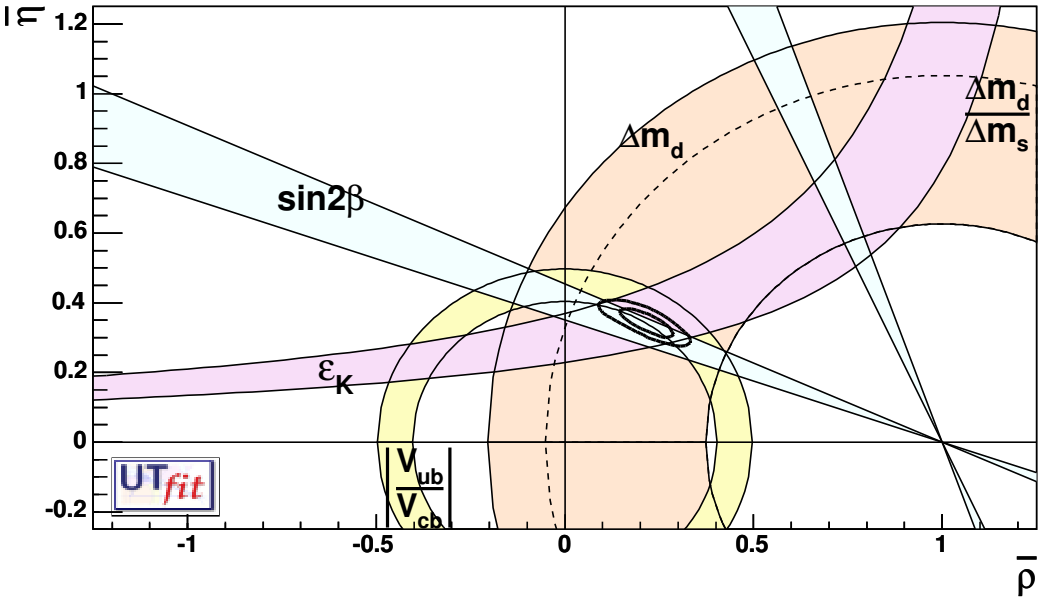


Figure 1.2: *Analysis of the Unitarity Triangle proposed in [9]. The used constraints are:* $|V_{ub}/V_{cb}|$, $\Delta m_d$, $\Delta m_d/\Delta m_s$ *and* $sin(2\beta)$.

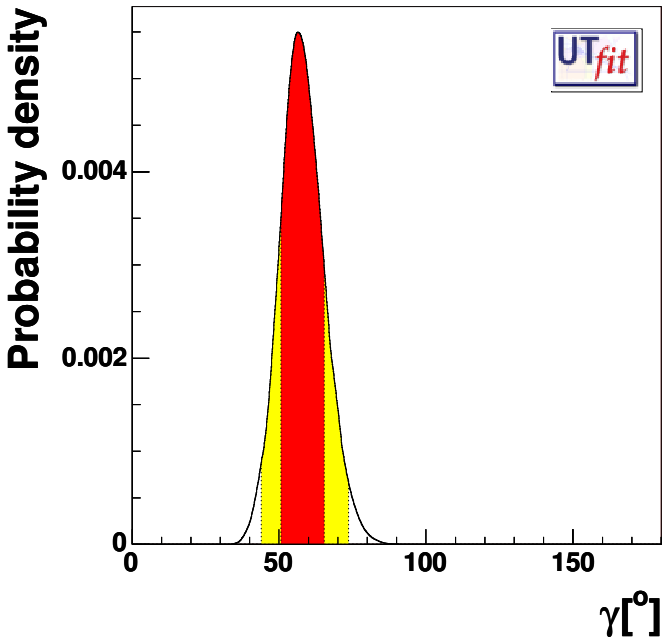


Figure 1.3: $\gamma$ *posterior probability density function obtained from the analysis of the Unitarity Triangle proposed in [9]. The expected value of* $\gamma$ *is* $(57.9 \pm 7.4)^{\circ}$.

where $S(x_t)$ is the Inami-Lim function [10] and $x_t = m_t^2/M_W^2$. $m_t$ is the top mass in the $\overline{MS}$ regularization scheme, $m_t^{\overline{MS}}$, and $\eta_c$ is the perturbative QCD short-distance NLO correction. The remaining factor, $f_{B_d}^2 \hat{B}_{B_d}$, encodes the information of non-perturbative QCD. The $\Delta m_d$ constraint can be represented by a circle centered at $(1, 0)$.

- The limit on the lower value for the time oscillation period of the $B_s^0 - \bar{B}_s^0$ system is transformed into a limit on $\Delta m_s$ and compared with $\Delta m_d$

$$\frac{\Delta m_d}{\Delta m_s} = \frac{m_{B_d} f_{B_d}^2 \hat{B}_{B_d}}{m_{B_s} f_{B_s}^2 \hat{B}_{B_s}} \left( \frac{\lambda}{1 - \frac{\lambda^2}{2}} \right)^2 \left[ (1 - \bar{\rho})^2 + \bar{\eta}^2 \right]. \tag{1.33}$$

  This give again a circle centered at $(1, 0)$.

- CP violation in the kaon system which is expressed by $|\varepsilon_K|$

$$|\varepsilon_K| = C_\varepsilon \; A^2 \lambda^6 \; \bar{\eta} \left[ -\eta_1 S(x_c) + \eta_2 S(x_t) \left( A^2 \lambda^4 \left( 1 - \bar{\rho} \right) \right) + \eta_3 S(x_c, x_t) \right] \; \hat{B}_K \,, \tag{1.34}$$

  where

$$C_\varepsilon = \frac{G_F^2 f_K^2 m_K m_W^2}{6\sqrt{2}\pi^2 \Delta m_K} \,. \tag{1.35}$$

  $S(x_i)$ and $S(x_i, x_j)$ are the appropriate Inami-Lim functions [10] of $x_q = m_q^2/m_W^2$, including the next-to-leading order QCD corrections [11, 12]. $f_K$ is the kaon decay constant and $\Delta m_K$ the neutral kaon system mixing frequency.

- The measurement of $\sin(2\beta)$ from the mixing induced $CP$ asymmetry in $B_d \to J/\psi K_{S,L}$.

The Input values for parameters and constraints entering in the fit have been agreed at the CKM Workshops [13], HFAG [14] and LP05 [15]

This constraint select the region on the $(\bar{\rho}, \bar{\eta})$ plane:

$$\begin{aligned} \bar{\rho} &= 0.214 \pm 0.047 \\ \bar{\eta} &= 0.343 \pm 0.028 \end{aligned} \tag{1.36}$$

Fig 1.3 shows the $\gamma$ posterior probability density function obtained with a Bayesian approach, from the constraint used in Fig. 1.2. The expected value of $\gamma$ is $(57.9 \pm 7.4)^\circ$.

## 1.3 $\gamma$ measurement using $B^{\pm} \to \tilde{D}^{(*)0}K^{(*)\pm}$ decays

The decay amplitudes of the channels $B^+ \to D^0K^+$ and $B^+ \to \bar{D}^0K^+$ are proportional respectively to the element $V_{ub}$ and $V_{cb}$ of the $CKM$ matrix and therefore their interference is sensitive to the weak phase $\gamma = arg(\frac{V_{ud}V_{ub}^*}{V_{cd}V_{cb}^*})$ [16]. The amplitude of the $B^+ \to D^0K^+$ decay is suppressed with respect to the amplitude of $B^+ \to \bar{D}^0K^+$ since, as shown in Fig. 1.4, the ratio between the two amplitudes is small due to the $CKM$ factors:

$$|\frac{V_{ub}^*V_{cs}}{V_{cb}^*V_{us}}| = \frac{1}{\lambda} \cdot |\frac{V_{ub}}{V_{cb}}| \sim 0.39 \tag{1.37}$$

with $|\frac{V_{ub}}{V_{cb}}| \sim 0.086$ and $\lambda = sin\theta_C \sim 0.22$.

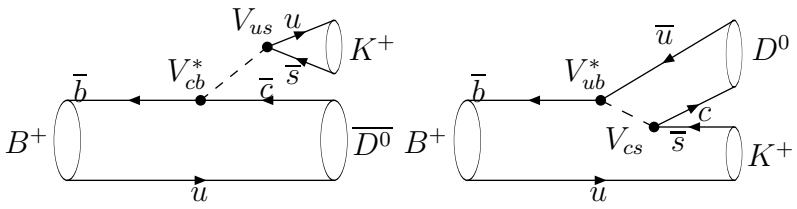


Figure 1.4: *Diagrams of the* $B^+ \to \bar{D}^0K^+$ *and* $B^+ \to D^0K^+$ *decays.*

Moreover in the case of $B^+ \to \bar{D}^0K^+$ decay the quarks forming the kaon can assume any color, while in the other case they need to have the same color of the initial quarks in the B meson. This reduces the amplitude of the $B^+ \to D^0K^+$ by a factor 3.

If we define the quantity $r_B$ as the ratio of the two amplitudes:

$$r_B = \frac{|A(B^+ \to D^0K^+)|}{|A(B^+ \to \overline{D^0}K^+)|} \tag{1.38}$$

the expected values for $r_B$ is $\sim 0.1$ from the current measurements.

The phase between the two diagrams contains two contributions: the strong phase that preserves $CP$ and the weak phase of the element $V_{ub}$ (the phase $\gamma$) that violates $CP$.

Different methods have been proposed for the measurement of $\gamma$ from the interference of the channels $b \to c\overline{u}s$ and $b \to u\overline{c}s$, The most important are the GLW, the ADS and the Dalitz method.

### 1.3.1 The GLW method

The Gronau-London-Wyler (GLW) method [17, 18] is the first method proposed for the measurement of $\gamma$ with the $B^{\pm} \to D^0K^{\pm}$ decays. It presents small theoretical uncertainty

but it is strongly limited by the statistics. This method uses for the determination of $\gamma$ the decays $B^{\pm} \to D^0_{\pm} K^{\pm}$ where $D^0_{\pm}$ are $D^0$ $CP$ eigenstates: they are reconstructed from final states with even $CP$, like $\pi^+\pi^-$ and $K^+K^-$ and odd $CP$, like $K_s\pi^0$. The states $D^0_{\pm}$ are defined as:

$$|D^0_{\pm}\rangle = \frac{1}{\sqrt{2}}(|D^0\rangle \pm |\overline{D^0}\rangle) \ . \tag{1.39}$$

It is possible to write the following relations between the amplitudes:

$$\begin{aligned} A(B^+ \to D^0 K^+) &= e^{2i\gamma} \cdot A(B^- \to \overline{D^0} K^-) \ , \\ A(B^+ \to \overline{D^0} K^+) &= A(B^- \to D^0 K^-) \ . \end{aligned} \tag{1.40}$$

Moreover from Eq. 1.39:

$$\sqrt{2} \cdot A(B^+ \to D^0_{\pm} K^+) = A(B^+ \to D^0 K^+) \pm A(B^+ \to \overline{D^0} K^+) \ . \tag{1.41}$$

These relations can be represented as two triangles in the complex plane:

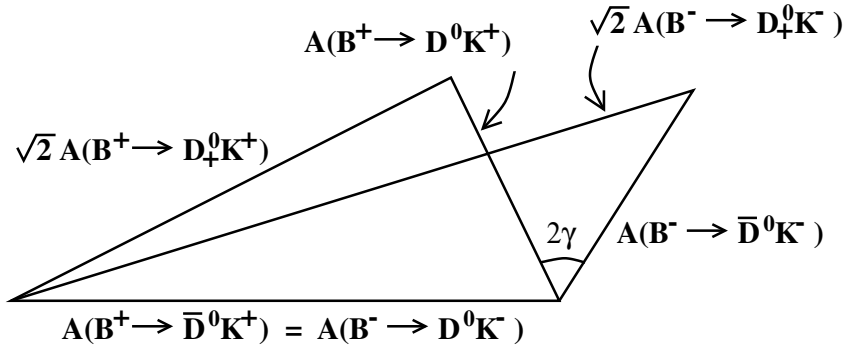


Figure 1.5: *Representation on the complex plane of the relation 1.41 between the amplitudes used for the GLW method.*

For the measurement of $\gamma$ the following observables are used:

$$\begin{aligned} R_{CP^{\pm}} &= \frac{\Gamma(B^+ \to D^0_{CP^{\pm}} K^+) + \Gamma(B^- \to D^0_{CP^{\pm}} K^-)}{\Gamma(B^+ \to D^0 K^+) + \Gamma(B^- \to \overline{D}^0 K^-)} = 1 + {r_B}^2 \pm 2 r_B \cos\gamma \cos\delta_B \\ A_{CP^{\pm}} &= \frac{\Gamma(B^+ \to D^0_{CP^{\pm}} K^+) - \Gamma(B^- \to D^0_{CP^{\pm}} K^-)}{\Gamma(B^+ \to D^0_{CP^{\pm}} K^+) + \Gamma(B^- \to D^0_{CP^{\pm}} K^-)} = \frac{\pm 2 r_B \sin\gamma \sin\delta_B}{R_{CP^{\pm}}} \end{aligned} \tag{1.42}$$

where $\delta_B$ the strong phase between the two amplitudes, $\gamma$ the weak phase and $r_B$ the ratio of the two amplitudes.

Since $r_B$ is expected $\sim 0.1$ the triangle of Fig. 1.5 tends to be degenerate. Very high statistics is then required to use this method for the measurement of $\gamma$.

### 1.3.2 The ADS method

The Atwood-Dunietz-Soni (ADS) method [19, 20] uses the $B^+ \to D^0 K^+$ and $B^+ \to \bar{D}^0 K^+$ decays with the $D^0$ decaying in flavor eigenstates. $B$ meson decays in final states that can be reached in two ways are considered: decay chains via the color allowed $B$ decay followed by the double Cabibbo suppressed $D$ decay or via color suppressed $B$ decay followed by the Cabibbo allowed $D$ decay. Fig. 1.6 shows the two possible decay chains. In this way the two complete amplitudes has comparable amplitudes and so larger interfere terms can be seen.

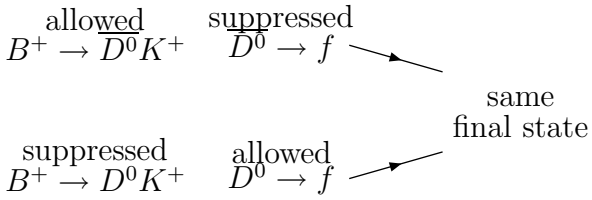


Figure 1.6: *Decay chain used by the ADS method*

The amplitudes of the favored and suppressed $B$ decays are related by the equation:

$$A(B^+ \to D^0 K^+) = r_B A(B^+ \to \overline{D^0} K^+) e^{i\gamma} e^{i\delta_B} \ , \tag{1.43}$$

where $\delta_B$ is the strong phase between the two amplitudes, $\gamma$ the weak phase and $r_B$ the ratio of the two amplitudes.

For the $D^0$ decay:

$$A(\overline{D^0} \to f) = r_D A(D^0 \to f) e^{i\delta_D} \ , \tag{1.44}$$

with $\delta_D$ the phase between the amplitude of the two $D$ decays and $r_D$ the ratio between them:

$$r_D \ = \ \frac{|A(\overline{D^0} \to f)|}{|A(D^0 \to f)|} \ . \tag{1.45}$$

For the measurement of $\gamma$ the following observables are used:

$$\begin{aligned} R_{ADS} &= \frac{\Gamma(B^- \to [f]_D K^-) + \Gamma(B^+ \to [\overline{f}]_D K^+)}{\Gamma(B^- \to [\overline{f}]_D K^-) + \Gamma(B^+ \to [f]_D K^+)} \\ &= r_D^2 + {r_B}^2 + 2 r_B r_D \cos\gamma \cos(\delta_B + \delta_D) \\ A_{ADS} &= \frac{\Gamma(B^- \to [f]_D K^-) - \Gamma(B^+ \to [\overline{f}]_D K^+)}{\Gamma(B^- \to [f]_D K^-) + \Gamma(B^+ \to [\overline{f}]_D K^+)} \\ &= 2 r_B r_D \sin\gamma \sin(\delta_B + \delta_D)/R_{ADS} \end{aligned} \tag{1.46}$$

where $\delta = \delta_B + \delta_D$ is the sum of the relative strong phases. A particular final states $f$ of the $D^0$ decays is $K^-\pi^+$. The limit of this method is that the product of the Branching ratios of the $B$ and $D$ decays is very small, so the method is limited from the statistics.

## 1.4 The Dalitz method

The Dalitz [21] method [22],proposed by Giry, Grossman, Soffer and Zupan, uses the $B^\pm \to \tilde{D}K^\pm$ decays followed by a multi body $D$ decay. The primary advantage of this method is that it involves the entire resonant structure of the three-body $D$ decay, with interference of doubly Cabibbo-suppressed (DCS), Cabibbo-allowed (CA), and $CP$ eigenstate amplitudes, providing the sensitivity to $\gamma$. The $\gamma$ analysis with the Dalitz model is performed using the $D^0 \to K_S\pi^-\pi^+$ decay but other $D$ decays, such $D^0 \to K_S K^- K^+$ can be used. The advantage of using $D^0 \to K_S\pi^-\pi^+$ arises from the complex resonant structure of Dalitz amplitude that gives large interference regions in the Dalitz plot.

To perform the measurement of the angle $\gamma$ the two CP-conjugate decay modes must be measured: $B^\pm \to \tilde{D}K^\pm \to (K_S\pi^-\pi^+)_{\tilde{D}}K^\pm$, and a Dalitz plot analysis of the $K_S\pi^-\pi^+$ final state originating from the intermediate $D$ meson must be performed. In the following $D^0 - \bar{D}^0$ mixing will be neglected, which is a good approximation in the context of the Standard Model [23].

Considering the following cascade decay

$$B^- \to \tilde{D}K^- \to (K_S\pi^-\pi^+)_{\tilde{D}}K^- \ , \tag{1.47}$$

the amplitudes:

$$A(B^- \to D^0 K^-) \equiv A_B \ , \tag{1.48}$$

$$A(B^- \to \bar{D}^0 K^-) \equiv A_B r_B e^{i(\delta_B - \gamma)} \ . \tag{1.49}$$

The same definitions apply to the amplitudes for the $CP$ conjugate cascade $B^+ \to \tilde{D}K^+ \to (K_S\,\pi^+\pi^-)_{\tilde{D}}K^+$, with the change of weak phase sign $\gamma \to -\gamma$ in Eq. 1.49. Since the strong phase of $A_B$ is set to zero by convention, $\delta_B$ is the difference of strong phases between the two amplitudes. For the $CKM$ elements, the usual convention of the weak phases is used.

For the three-body $D$ meson decay the following quantity is defined:

$$\begin{aligned} A_D(s_{12}, s_{13}) \equiv A_{12,13}\, e^{i\delta_{12,13}} &\equiv A(D^0 \to K_S(p_1)\pi^-(p_2)\pi^+(p_3)) \\ &= A(\bar{D}^0 \to K_S(p_1)\pi^+(p_2)\pi^-(p_3)) \ , \end{aligned} \tag{1.50}$$

where $s_{ij} = (p_i + p_j)^2$, and $p_1, p_2, p_3$ are the four-momenta of the $K_S, \pi^-, \pi^+$ respectively. The magnitude $A_{12,13}$ is by definition positive, so that $\delta_{12,13}$ can vary between 0 and $2\pi$. In the last equality the $CP$ symmetry of the strong interaction together with the fact that the final state is a spin zero state is used. With the above definitions, the amplitude for the cascade decay is:

$$A(B^- \to (K_S\pi^-\pi^+)_{\tilde{D}}K^-) = A_B \mathcal{P}_D\big(A_D(s_{12}, s_{13}) + r_B e^{i(\delta_B - \gamma)} A_D(s_{13}, s_{12})\big) \ , \tag{1.51}$$

where $\mathcal{P}_D$ is the $D$ meson propagator. The expression for the reduced partial decay width is:

$$\begin{aligned} d\hat{\Gamma}(B^- \to (K_S\pi^-\pi^+)_{\tilde{D}}K^-) = \Big(&A^2_{12,13} + r_B^2\, A^2_{13,12} \\ &+ 2r_B Re\left[A_D(s_{12}, s_{13})\, A_D^*(s_{13}, s_{12})\, e^{-i(\delta_B - \gamma)}\right]\Big) dp \ , \end{aligned} \tag{1.52}$$

where $dp$ denotes the phase space variables, and the extremely accurate narrow width approximation for the $D$ meson propagator is used.

In general, there is no symmetry between the two arguments of $A_D$ in Eq. (1.51), and thus in the rates over the Dalitz plot. A symmetry would be present if, for instance, the three-body $D$ decay proceeded only through $\rho$-like resonances. However, the product $A_D(s_{12}, s_{13})\, A_D^*(s_{13}, s_{12})$ in the interference term in Eq. (1.52) is symmetric under the exchange $s_{12} \leftrightarrow s_{13}$ followed by complex conjugation. This fact is used to simplify the analysis.

The moduli of the $D$ decay amplitude $A_{12,13}$ can be measured from the Dalitz plot of the $D^0 \to K_S\pi^-\pi^+$ decay. To perform this measurement the flavor of the decaying neutral $D$ meson has to be tagged. This can be best achieved by using the charge of the

soft pion in the decay $D^{*+} \to D^0\pi^+$. However, the phase $\delta_{12,13}$ of the $D$ meson decay amplitude is not measurable without further model dependent assumptions.

The Dalitz analysis needed to extract $\gamma$ can be performed either in a model independent way or utilizing a model which can be verified on control samples. The advantage of introducing a model dependence is the reduction in statistical error due to the limited number of free parameters. The price to pay is that a complete Dalitz plot analysis of the data is needed and uncertainties on the Dalitz amplitude give large systematic errors in the measurement of $\gamma$.

### 1.4.1 Model independent determination of $\gamma$

To perform a model independent determination of the angle $\gamma$ it is useful to write the last term of Eq. 1.52 using the trigonometric relation $\cos(a+b) = \cos a\, \cos b - \sin a\, \sin b$:

$$\begin{aligned} &Re\left[A_D(s_{12}, s_{13})\, A_D^*(s_{13}, s_{12})\, e^{-i(\delta_B - \gamma)}\right] = \\ &A_{12,13}\, A_{13,12}\left[\cos(\delta_{12,13} - \delta_{13,12})\cos(\delta_B - \gamma) + \sin(\delta_{12,13} - \delta_{13,12})\sin(\delta_B - \gamma)\right] \ . \end{aligned} \tag{1.53}$$

To compare with the data, an integration over at least some part of the Dalitz plot has to be performed. Therefore a partition of the Dalitz plot into $n$ bins is necessary:

$$c_i \equiv \int_i dp A_{12,13}\, A_{13,12}\, \cos(\delta_{12,13} - \delta_{13,12}) \ , \tag{1.54a}$$

$$s_i \equiv \int_i dp A_{12,13}\, A_{13,12} \sin(\delta_{12,13} - \delta_{13,12}) \ , \tag{1.54b}$$

$$T_i \equiv \int_i dp A_{12,13}^2 \ , \tag{1.54c}$$

where the integrals are done over the phase space of the $i$-th bin. The variables $c_i$ and $s_i$ contain differences of strong phases and are therefore unknowns in the analysis. The variables $T_i$, on the other hand, can be measured from the flavor tagged $D$ decays as discussed above, and are assumed to be known inputs into the analysis.

Due to the symmetry of the interference term, it is convenient to use pairs of bins that are placed symmetrically about the $12 \leftrightarrow 13$ line, as shown in Fig. 1.7. Consider an even, $n = 2k$, number of bins. The $k$ bins lying below the symmetry axis are denoted by index $i$, while the remaining bins are indexed with $\bar{i}$. The $\bar{i}$-th bin is obtained by mirroring the $i$-th bin over the axis of symmetry. The variables $c_i, s_i$ of the $i$-th bin are related to the variables of the $\bar{i}$-th bin by

$$c_{\bar{i}} = c_i \qquad s_{\bar{i}} = -s_i \tag{1.55}$$

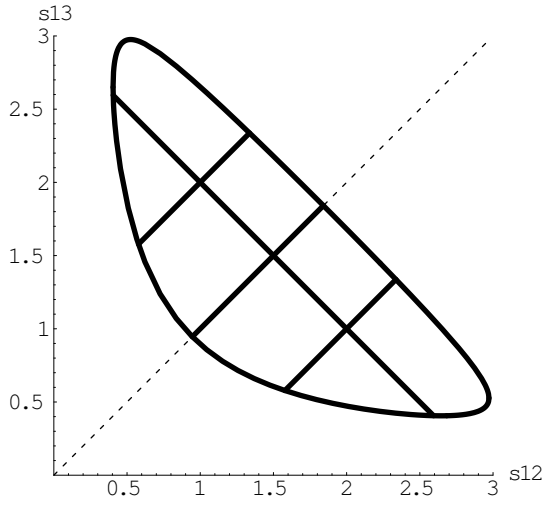


Figure 1.7: *The partitions of Dalitz plot. The symmetry axis is the dashed line. On the axes* $s_{12} = m^2_{K_s\pi^-}$ *and* $s_{13} = m^2_{K_s\pi^+}$ *in* $GeV^2$.

while there is no relation between $T_i$ and $T_{\bar{i}}$. That had one used $12 \leftrightarrow 13$ symmetric bins centered on the symmetry axis, one would have had $s_i = 0$.

Together with the information available from the $B^+$ decay, a set of $4k$ equations is obtained:

$$\hat{\Gamma}_i^- \equiv \int_i d\hat{\Gamma}(B^- \to (K_S\pi^-\pi^+)_{\tilde{D}} K^-) = T_i + r_B^2 T_{\bar{i}} + 2r_B[\cos(\delta_B - \gamma)c_i + \sin(\delta_B - \gamma)s_i], \tag{1.56a}$$

$$\hat{\Gamma}_{\bar{i}}^- \equiv \int_{\bar{i}} d\hat{\Gamma}(B^- \to (K_S\pi^-\pi^+)_{\tilde{D}} K^-) = T_{\bar{i}} + r_B^2 T_i + 2r_B[\cos(\delta_B - \gamma)c_i - \sin(\delta_B - \gamma)s_i], \tag{1.56b}$$

$$\hat{\Gamma}_i^+ \equiv \int_i d\hat{\Gamma}(B^+ \to (K_S\pi^-\pi^+)_{\tilde{D}} K^+) = T_{\bar{i}} + r_B^2 T_i + 2r_B[\cos(\delta_B + \gamma)c_i - \sin(\delta_B + \gamma)s_i], \tag{1.56c}$$

$$\hat{\Gamma}_{\bar{i}}^+ \equiv \int_{\bar{i}} d\hat{\Gamma}(B^+ \to (K_S\pi^-\pi^+)_{\tilde{D}} K^+) = T_i + r_B^2 T_{\bar{i}} + 2r_B[\cos(\delta_B + \gamma)c_i + \sin(\delta_B + \gamma)s_i]. \tag{1.56d}$$

These equations are related to each other through $12 \leftrightarrow 13$ and/or $\gamma \leftrightarrow -\gamma$ exchanges. All in all, there are $2k + 3$ unknowns in (1.56),

$$c_i,\ s_i,\ r_B,\ \delta_B,\ \gamma \tag{1.57}$$

so that the $4k$ relations (1.56) are solvable for $k \geq 2$. In other words, a partition of the $D$

meson Dalitz plot to four or more bins allows for the determination of $\gamma$ without hadronic uncertainties.

### 1.4.2 Measurement of $c_i$ and $s_i$ at a charm factory

So far, the $B$ decay sample has been used to obtain all the unknowns, including $c_i$ and $s_i$, which are parameters of the charm system. A measurement of the parameters $c_i$ and $s_i$ can be obtained from a charm factory as CLEO-C. Doing so will reduce the number of unknowns that need to be determined from the relatively low-statistics $B$ sample reducing the error in the measurement of $\gamma$.

The $c_i$ can be independently measured at a charm factory [24, 25, 26]. This can be done by running the machine at the $\psi(3770)$ resonance, which decays into a $D\bar{D}$ pair. If one $D$ meson is detected in a $CP$ eigenstate decay mode, it tags the other $D$ as an eigenstate of the opposite $CP$ eigenvalue. The amplitude and partial decay width for this state to decay into the final state of interest are:

$$\begin{aligned} A(D^0_\pm \to K_S(p_1)\pi^-(p_2)\pi^+(p_3)) &= \frac{1}{\sqrt{2}}\left(A_D(s_{12},s_{13}) \pm A_D(s_{13},s_{12})\right) , \\ d\Gamma(D^0_\pm \to K_S(p_1)\pi^-(p_2)\pi^+(p_3)) &= \frac{1}{2}\left(A^2_{12,13} + A^2_{13,12}\right) \pm A_{12,13}A_{13,12}\cos(\delta_{12,13}-\delta_{13,12})dp , \end{aligned} \tag{1.58}$$

where $D^0_\pm \equiv (D^0 \pm \bar{D}^0)/\sqrt{2}$. With these relations, one readily obtains

$$c_i = \frac{1}{2}\left[\int_i d\Gamma(D^0_+ \to K_S(p_1)\pi^-(p_2)\pi^+(p_3)) - \int_i d\Gamma(D^0_- \to K_S(p_1)\pi^-(p_2)\pi^+(p_3))\right] . \tag{1.59}$$

Obtaining this independent measurements reduces the error in the measurement of $\gamma$ by removing $k$ of the $2k+3$ unknowns.

In addition, if one of the $D$ mesons decays into a non-$CP$ eigenstate, it is possible to measure the parameters $s_i$. If the $\psi(3770)$ decays into a $D\bar{D}$ pair of which one decays into $K_S\pi^-\pi^+$ and the other decays into some general state $g$ the partial decay width corresponding to the $i^{th}$ bin of the $K_S\pi^-\pi^+$ Dalitz plot and the $j^{th}$ bin of the $g$ final state's phase space is

$$\Gamma_{i,j} \propto T_i T^g_{\bar{j}} + T_{\bar{i}} T^g_j - 2(c_i c^g_j + s_i s^g_j) , \tag{1.60}$$

where $T^g_j$, $c^g_j$, $s^g_j$ are defined in Eq. 1.54. If, in particular, $g = K_S\pi^-\pi^+$ and $j = i$ (or $j = \bar{i}$) it is possible to measure $s_i^2$.

If the $i^{th}$ bin is divided it into $n_i$ sub-bins, such that the quantities $A_{12,13}$, $\cos(\delta_{12,13} - \delta_{13,12})$, and $\sin(\delta_{12,13} - \delta_{13,12})$ do not change significantly within each sub-bin $i'$ Eq. (1.54a)

may be written as

$$c_i = \sum_{i'} c_{i'} \;\; = \;\; \sum_{i'} A_{i'} \, A_{\overline{i'}} \cos(\delta_{i'} - \delta_{\overline{i'}}) \Delta p_{i'} = \sum_{i'} \sqrt{T_{i'} T_{\overline{i'}}} \, \cos(\delta_{i'} - \delta_{\overline{i'}}) \; , \quad (1.61)$$

where the $\overline{i'}$-th sub-bin is the $12 \leftrightarrow 13$ mirror image of the $i'$-th sub-bin, $A_{i'}$ and $\delta_{i'}$ are the values of $A_{12,13}$ and $\delta_{12,13}$ on sub-bin $i'$, taken to be constant throughout the sub-bin, and $\Delta p_{i'}$ is the area of sub-bin $i'$.

This statement appears to introduce model dependence. In practice, however, the high statistics in the tagged $D$ sample and the charm factory $\psi(3770)$ sample allow its verification up to a statistical error, which can be measured and propagated to the final measurement of $\gamma$.

Analogously to Eq. (1.54c), the quantities $T_{i'} = A^2_{12,13} \Delta p_{i'}$ are defined, which are measured using the tagged $D$ sample. The $c_{i'}$'s are assumed to be measured at the charm factory, applying Eq. 1.59 to the sub-bin $i'$. Similarly, Eq. (1.54b) becomes

$$s_i = \sum_{i'} \sqrt{T_{i'} T_{\overline{i'}}} \, \sin(\delta_{i'} - \delta_{\overline{i'}}) = \sum_{i'} \pm \sqrt{T_{i'} T_{\overline{i'}} - c^2_{i'}} \; . \quad (1.62)$$

Eq. (1.62) removes the $k$ unknowns $s_i$, and replaces them with the two-fold ambiguity associated with the sign of the square root. Thus, the best approach is to have the signs of $s_i$ determined by the fit, while constraining their absolute values to satisfy Eq. (1.62). Doing so will reduce the "strain" on the $B$ decay sample, reducing the error on $\gamma$.

### 1.4.3 Model dependent determination of $\gamma$

If the functional dependence of both the moduli and the phases of the $D^0$ meson decay amplitudes $A_D(s_{12}, s_{13})$ were known, then the analysis would be simplified. There would be only three variables, $r_B, \delta_B$, and $\gamma$, that need to be fit to the reduced partial decay widths in Eq. (1.52).

It is important to stress that the assumption on $D^0$ meson decay amplitudes can be tested. By making use of the high statistics tagged $D$ sample, one can test that the assumed shapes of the resonances are consistent with the data. While the error introduced by using a particular Dalitz model is theoretical, it is expected to be much smaller than the statistical error in the measurement of $\gamma$. It will become a problem only when the $B$ sample will be large enough to provide a precision measurement of $\gamma$. By then the tagged $D$ sample will have increased as well allowing even more precise tests of these assumptions.

A detailed description of the $D^0$ meson decay amplitude parameterization is discussed in Chapter 3.

### 1.4.4 Use of $B^{\pm} \to \tilde{D}^{*0} K^{\pm}$ decays

The $\gamma$ analysis can also be performed using $B^- \to \tilde{D}^{*0} K^-$ [27] decay, and $\gamma$ can be extracted along with the amplitude ratio $r_B^*$ and strong phase difference $\delta_B^*$. In this case the different $\delta_B^*$ values depending on the $D^{*0}$ decay mode has to be considered. Considering in fact the decay mode $B^- \to D^* K^-$, the $D^*$ meson (denoted as $\tilde{D}^*$) can be written as:

$$\tilde{D}^* = D^{*0} + r_B^* e^{i\left(\delta_B^* - \gamma\right)} \bar{D}^{*0} \ . \tag{1.63}$$

Defining the $D^*$ $CP$ eigenstates as (using the phase convention $CP(D^{*0}) = \bar{D}^{*0}$ and $CP(\bar{D}^{*0}) = D^{*0}$ that does not affect observable quantities):

$$D_+^* = \frac{D^{*0} + \bar{D}^{*0}}{\sqrt{2}} \qquad D_-^* = \frac{D^{*0} - \bar{D}^{*0}}{\sqrt{2}} \ . \tag{1.64}$$

$\tilde{D}^*$ results:

$$\tilde{D}^* = \frac{D_+^* + D_-^*}{\sqrt{2}} + r_B^* e^{i(\delta_B - \gamma)} \frac{D_+^* - D_-^*}{\sqrt{2}} \ . \tag{1.65}$$

Considering the $D_+^*$ and $D_-^*$ decays in $D\pi^0$ and $D\gamma$ and using $\eta_X$ to denote the $CP$ eigenvalue of $X = (\pi^0, \gamma)$, $\eta_{D^*} = \eta_D \times \eta_X \times (-1)^l$ where $l$ is the angular momentum between $D$ and $X$. In the $D\pi^0$ decay mode $l = 1$ for the angular moment conservation, then $\eta_{D^*} = \eta_D$ and $D_\pm^* \to D_\pm \pi^0$. In the $D\gamma$ decay mode again $l = -1$ for parity conservation then $\eta_{D^*} = -1 \times \eta_D$ and $D_\pm^* \to D_\mp \gamma$. Then the $D$ neutral meson (denoted as $\tilde{D}$) coming from the decay $\tilde{D}^* \to \tilde{D}\pi^0$ can be written as:

$$\begin{aligned} \tilde{D} &= \frac{D_+ + D_-}{\sqrt{2}} + r_B^* e^{i\left(\delta_B^* - \gamma\right)} \frac{D_+ - D_-}{\sqrt{2}} \\ &= D^0 + r_B^* e^{i\left(\delta_B^* - \gamma\right)} \bar{D}^0 \ , \end{aligned} \tag{1.66}$$

but the one coming from the decay $\tilde{D}^* \to \tilde{D}\gamma$ is:

$$\begin{aligned} \tilde{D} &= \frac{D_- + D_+}{\sqrt{2}} + r_B^* e^{i\left(\delta_B^* - \gamma\right)} \frac{D_- - D_+}{\sqrt{2}} \\ &= D^0 - r_B^* e^{i\left(\delta_B^* - \gamma\right)} \bar{D}^0 \\ &= D^0 + r_B^* e^{i\left(\delta_B^* + \pi - \gamma\right)} \bar{D}^0 \ . \end{aligned} \tag{1.67}$$

Thus there is a shift of the strong phase of $\pi$ between the to cases.

The decay chain $B^{\mp} \to \tilde{D}^{(*)0}K^{\mp}$ rate can than be written as:

$$\Gamma_{\mp} \propto |A_D(m^2_{\mp}, m^2_{\pm})|^2 + r_B^{(*)2}|A_D(m^2_{\pm}, m^2_{\mp})|^2 + 2\kappa r_B^{(*)} Re(A_D(m^2_{\mp}, m^2_{\pm})A_D^*(m^2_{\pm}, m^2_{\mp})e^{i(\delta_B^{(*)} \mp \gamma)}) \,, \tag{1.68}$$

where $m^2_{\mp}$ is the squared invariant mass of the $K_S\pi^{\mp}$ combination, $A_D(m^2_-, m^2_+)$ is the $D^0 \to K_S\pi^-\pi^+$ decay amplitude, $r_B^{(*)}$ and $\delta_B^{(*)}$ are the amplitude ratio and relative strong phase between the amplitudes $B^- \to \bar{D}^{(*)0}K^-$ and $B^- \to D^{(*)0}K^-$ and $\kappa$ takes the value $+1$ for $B^- \to \tilde{D}^0K^-$ and $B^- \to \tilde{D}^{*0}(\tilde{D}^0\pi^0)K^-$, and $-1$ for $B^- \to \tilde{D}^{*0}(\tilde{D}^0\gamma)K^-$.

### 1.4.5 Use of $B^{\pm} \to \tilde{D}^0K^{*\pm}$ decays

To use $B^{\pm} \to \tilde{D}^0K^{*\pm}$ [28] decays it must be taken in account the fact that the natural width of the $K^{*-}$ is not small ($\sim$50 MeV) and the interference with the non-resonant $B^- \to D^0(K\pi)^-_{\text{non}-\text{K}^*}$ processes may not be negligible. This changes the relationships between the unitarity angle $\gamma$ and the experimental observables.

The amplitudes of the $B^- \to (D^0X_s^-)_p$ and $B^- \to (\bar{D}^0X_s^-)_p$ processes, where $p$ indicates a point in the phase space of the final state and $X_s^-$ is a state with strangeness, is:

$$A(B^- \to (D^0X_s^-)_p) = A_{cp}e^{i\delta_{cp}} \,, \tag{1.69}$$

$$A(B^- \to (\bar{D}^0X_s^-)_p) = A_{up}e^{i\delta_{up}}e^{-i\gamma} \,, \tag{1.70}$$

$$A(D^0 \to f) = A_f e^{i\delta_f} \,, \tag{1.71}$$

$$A(D^0 \to \bar{f}) = A_{\bar{f}} e^{i\delta_{\bar{f}}} \,, \tag{1.72}$$

where $A_{cp}$, $A_{up}$, $A_f$ and $A_{\bar{f}}$ are real and positive. The index $p$ indicates the position in the phase space of $DX_s^-$, that is, $A_c$, $A_u$, $\delta_c$ and $\delta_u$ generally vary as a function of $p$. The subscript $c$ and $u$ refer to the $b \to c$ and $b \to u$ transitions, respectively. The amplitudes $A_{cp}e^{i\delta_{cp}}$ and $A_{up}e^{i\delta_{up}}e^{-i\gamma}$ generally include both the resonant $B^- \to D^0/\bar{D}^0K^{*-}$ processes and the non-resonant contributions. The amplitudes for the $D^0$ decay can generally include the case where $D^0 \to$3-body, for instance $D^0 \to K^0_S\pi^-\pi^+$; in this case $A_f e^{i\delta_f} = f(m^2_-, m^2_+)$ and $A_{\bar{f}}e^{i\delta_{\bar{f}}} = f(m^2_+, m^2_-)$, that is, $A_f$, $A_{\bar{f}}$, $\delta_f$ and $\delta_{\bar{f}}$ are functions of the Dalitz plot coordinates $m^2_{\pm}$, where $m^2_-$ and $m^2_+$ are the squared masses of the $K^0_S\pi^-$ and $K^0_S\pi^+$ combinations.

The amplitude of the process $B^- \to D[\to f]X_s^-$ can be written as:

$$A(B^- \to (D[\to f]X_s^-)_p) = A_{cp}A_f e^{i(\delta_{cp}+\delta_f)} + A_{up}A_{\bar{f}}e^{i(\delta_{up}+\delta_{\bar{f}}-\gamma)} \,. \tag{1.73}$$

From Eq. (1.73) the rate of the process $B^- \to D[\to f]X_s^-$ is:

$$\Gamma(B^- \to D[\to f]X_s^-) = \int dp \left( A_{cp}^2 A_f^2 + A_{up}^2 A_{\bar{f}}^2 + 2A_{cp}A_f A_{up}A_{\bar{f}} Re(e^{i(\delta_p+\delta_D-\gamma)}) \right) , \quad (1.74)$$

where $\delta_p = \delta_{up} - \delta_{cp}$ and $\delta_D = \delta_{\bar{f}} - \delta_f$. The rate for the charge-conjugated mode is the one in Eq. (1.74) with $\gamma \to -\gamma$. Analogously, the partial rates $\Gamma(B^- \to D^0 X_s^-)$ and $\Gamma(B^- \to \bar{D}^0 X_s^-)$ are:

$$\Gamma(B^- \to D^0 X_s^-) = \int dp \; A_{cp}^2 \, , \quad (1.75)$$

$$\Gamma(B^- \to \bar{D}^0 X_s^-) = \int dp \; A_{up}^2 \, . \quad (1.76)$$

Following the same notation as in [28], the quantities $r_s$, $k$ and $\delta_s$ are introduced, that will be useful for the $\gamma$ analysis:

$$r_s^2 = \frac{\Gamma(B^- \to \bar{D}^0 X_s^-)}{\Gamma(B^- \to D^0 X_s^-)} = \frac{\int dp \; A_{up}^2}{\int dp \; A_{cp}^2} \quad (1.77)$$

$$k e^{i\delta_s} = \frac{\int dp \; A_{cp} A_{up} e^{i\delta_p}}{\sqrt{\int dp \; A_{cp}^2 \int dp \; A_{up}^2}} \quad (1.78)$$

where $0 \leq k \leq 1$ for the Schwartz inequality and $\delta_s \in [0, 2\pi]$. In the limit of a $B \to$2-body decay, such as $B^- \to DK^-$:

$$\begin{aligned} & r_s \to r_B \equiv \frac{|A(B^- \to \bar{D}^0 K^-)|}{|A(B^- \to D^0 K^-)|} \, , \\ & \delta_s \to \delta_B \equiv \text{strong phase of } \frac{\mathrm{A(B^- \to \bar{D}^0 K^-)}}{\mathrm{A(B^- \to D^0 K^-)}} \, . \\ & k \to 1 \end{aligned} \quad (1.79)$$

In the case of the $D^0 \to K_S \pi^- \pi^+$ decay, $A_f e^{i\delta_f} = f(m_-^2, m_+^2)$ and $A_{\bar{f}} e^{i\delta_{\bar{f}}} = f(m_+^2, m_-^2)$. The amplitude for the process $B^\mp \to D[\to K_S^0 \pi^- \pi^+]X_s^\mp$ can be written as:

$$A(B^\mp \to D[\to K_S^0 \pi^- \pi^+]X_s^\mp) = A_{cp} e^{i\delta_{cp}} f(m_\mp^2, m_\pm^2) + A_{up} e^{i\delta_{up} \mp \gamma} f(m_\pm^2, m_\mp^2) \, , \quad (1.80)$$

and the rate is

$$\begin{aligned} \Gamma(B^\mp \to D[\to K_S^0 \pi^- \pi^+]X_s^\mp) \; & \propto \; |f_\mp|^2 + r_s^2 |f_\pm|^2 + \\ & \quad 2kr_s \left\{ \cos(\delta_s \mp \gamma) Re[f_\mp f_\pm^*] + \sin(\delta_s \mp \gamma) Im[f_\mp f_\pm^*] \right\} \\ & \equiv \; |f_\mp|^2 + r_s^2 |f_\pm|^2 + \\ & \quad 2kr_s |f_\mp| |f_\pm| \cos(\delta_s + \delta_D(m_\mp^2, m_\pm^2) \mp \gamma) \, , \end{aligned} \quad (1.81)$$

where $\delta_D(m^2_{\mp}, m^2_{\pm})$ is the strong phase difference between $f(m^2_{\pm}, m^2_{\mp})$ and $f(m^2_{\mp}, m^2_{\pm})$ and $r_s$, $k$ and $\delta_s$ are defined in Eqs. (1.77) and (1.78).

The notation has been simplified using $f_{\pm} \equiv f(m^2_{\pm}, m^2_{\mp})$ and $f_{\mp} \equiv f(m^2_{\mp}, m^2_{\pm})$. The parameterization given in Eq. (1.81) includes both resonant and non-resonant $(K\pi)^{\mp}$ contributions, since the amplitudes in Eqs. (1.69) and (1.70) include both.

## 1.5 Dalitz plot model

The $K$-matrix formalism provides an elegant way of dealing with strongly overlapping resonances and multi-channel dynamics (resonances). It allows to generalize two-body channel amplitudes to resonance production with final-state interaction. It was originally introduced by Wigner [29] and Wigner and Eisbud [30] for the study of resonances in nuclear reactions. The first use in particle physics goes back to an analysis of resonance production in $K\pi$ scattering by Dalitz and Tuan [31]. $K$-Matrix formalism arises in the context of two-body scattering processes for which unitarity is a strong requirement and then is extended to describe production decay processes.

### 1.5.1 Two body scattering

$S$-matrix formalism was developed by Heisenberg in 1942 [32]. In general, the amplitude for an initial state $|i>$ to be found in the final state $|f>$ is written as:

$$S_{fi} =< f|S|i > \ , \tag{1.82}$$

where $S$ is called the scattering operator. One may remove the probability that the initial and final states do not interact at all, by defining the transition operator $T$ through:

$$S = I + 2i\sqrt{\rho}T\sqrt{\rho} \ , \tag{1.83}$$

where $I$ is the identity operator. The factors 2 and i are introduced for convenience. $\rho$ represents the phase-space matrix and is diagonal by definition.

From conservation of probability, the scattering operator S is unitary:

$$SS^{\dagger} = S^{\dagger}S = I \ . \tag{1.84}$$

From the unitarity of S it follows:

$$(T^{-1} + i\rho)^{\dagger} = (T^{-1} + i\rho) \tag{1.85}$$

which leads to the definition of the $K$-matrix:

$$K^{-1} = (T^{-1} + i\rho) \ . \tag{1.86}$$

From Eq. 1.85 one finds that the $K$ operator is Hermitian:

$$K = K^{\dagger} \ . \tag{1.87}$$

From time reversal invariance of $S$ and $T$ it follows that the $K$ operator must be symmetric, i.e. the corresponding $K$-matrix is real and symmetric.

It is possible to eliminate the inverse operators in Eq. 1.86 by multiplying by $K$ and $T$ from left and right and vice versa, to obtain:

$$T = K + iK\rho T = K + iT\rho K \ , \tag{1.88}$$

obtaining for $T$:

$$T = K(I - i\rho K)^{-1} = (I + iK\rho)^{-1}K \ . \tag{1.89}$$

### 1.5.2 Resonances in the K-matrix formalism

There are two possibilities for parameterizing resonances in the $K$-matrix formalism: (1) Resonances can arise from constant $K$-matrix elements with the energy variation supplied by phase space or (2) from strongly varying pole terms corresponding to a phase motion [33]. They differ in their dynamical character. In case (1) they are assumed to arise from exchange forces in the corresponding hadronic channels (molecular resonances), so that dominant effects are expected near corresponding thresholds. The latter (2) (normal resonances) correspond to dynamical sources at the constituent level, coupling to the observed hadrons through decay [33]. The dynamical origin of resonances has to be determined experimentally. In the approximation that the transition amplitude is dominated by resonance production (scattering) one form for the $K$-matrix is the following:

$$K_{ij} = \sum_{\alpha} \frac{g_{\alpha i}(m) g_{\alpha j}(m)}{(m_{\alpha}^2 - m^2)\sqrt{\rho_i \rho_j}} + c_{ij} \ , \tag{1.90}$$

where $i$ and $j$ are referred to the initial and final states, the sum on $\alpha$ runs over the number of poles with masses $m_{\alpha}$ and the coupling (or residual functions, expressed in units of energy; $s = m^2$) are given by:

$$g_{\alpha i}^2(m) = m_{\alpha}\Gamma_{\alpha i} \ , \tag{1.91}$$

where $g_{\alpha i}(m)$ is real (but could be negative) above the threshold channel $i$. The constant $K$-matrix elements have to be unit-less and real to preserve unitarity. The corresponding width $\Gamma_\alpha(m)$ is

$$\Gamma_\alpha(m) = \sum_i \Gamma_{\alpha i}(m) \tag{1.92}$$

for each pole $\alpha$. In the simplest case of an isolated resonance and one single channel open it reproduces the Lorentz-invariant Breit-Wigner resonance formula.

Let us consider a single, well isolated resonance $\alpha$ coupling to n open two-body channels, where the mass $m_\alpha$ far above the thresholds of all two-body channels. The partial widths may be given by the expression:

$$\Gamma_{\alpha i}(m) = \frac{g_{\alpha i}^2(m)}{m_\alpha} = \gamma_{\alpha i}^2 \Gamma_\alpha^0 B_{l;\alpha i}^2(q_i, q_{\alpha i}) \rho_i \tag{1.93}$$

and the residual function by:

$$g_{\alpha i}(m) = \gamma_{\alpha i} \sqrt{m_\alpha \Gamma_\alpha^0} B_{l;\alpha i}(q_i, q_{\alpha i}) \sqrt{\rho_i} \ . \tag{1.94}$$

It is $q_{\alpha i} = q_i(m_\alpha)$ the breakup momentum [34] in channel $i$ at the $K$-matrix pole $m = m_\alpha$.

The $B_{l;\alpha i}(m)$ are ratios of centrifugal barrier factors in terms of the momentum in channel $i$ and the resonance breakup momentum for the orbital angular momentum l,

There are several parameterizations where some will be discussed in Sec. 1.5.3.

The $\gamma$'s are real constants (but they can be negative) and fulfill the normalization:

$$\sum_i \gamma_{\alpha i}^2 = 1 \tag{1.95}$$

which is motivated by unitarity. In practice, not all possible open channels are available so that this normalization condition is difficult to implement. As fit variable is preferred:

$$g_{\alpha i}^0 = \gamma_{\alpha i} \sqrt{m_\alpha \Gamma_\alpha^0} \tag{1.96}$$

The residual function is then given by:

$$g_{\alpha i}(m) = g_{\alpha i}^0 B_{l;\alpha i}(q_i, q_{\alpha i}) \sqrt{\rho_i} \ . \tag{1.97}$$

The $K$-matrix total width $\tilde{\Gamma}_\alpha$ and the $K$-matrix partial widths $\tilde{\Gamma}_{\alpha i}$ are defined by:

$$\tilde{\Gamma}_\alpha = \sum \tilde{\Gamma}_{\alpha i} = \Gamma_\alpha^0 \sum_i \gamma_{\alpha i}^2 \rho_i(m_\alpha) \ . \tag{1.98}$$

From these it is:

$$\begin{aligned} g^0_{\alpha i} &= \sqrt{\frac{m_\alpha \tilde{\Gamma}_{\alpha i}}{\rho_i(m_\alpha)}} \,, \\ \Gamma^0_\alpha &= \sum \tilde{\Gamma}_{\alpha i} \rho_i(m_\alpha) \,, \\ \gamma^2_{\alpha i} &= \frac{\tilde{\Gamma}_{\alpha i}}{\Gamma^0_\alpha \rho_i(m_\alpha)} \,. \end{aligned} \tag{1.99}$$

It is important to notice, that the $K$-matrix total width $\tilde{\Gamma}_\alpha$ does not need to be identical with the width which is observed in an experimental mass distribution nor with the width of the $T$-matrix pole in the complex energy plane.

In the simple case of a Breit-Wigner resonance far above the threshold for one possible open channel, in which the different definitions of widths coincide. In the limit the masses of the decay particles can be neglected compared to $m_\alpha$. it is $\Gamma(m_\alpha) \simeq \Gamma^0_\alpha$. In terms of $g^0_{\alpha i}$ the invariant $K$-matrix has the simple form:

$$K_{ij} = \sum_\alpha \frac{g^0_{\alpha i} g^0_{\alpha j} B_{l;\alpha i}(q_i, q_{\alpha i}) B_{l;\alpha j}(q_j, q_{\alpha j})}{m^2_\alpha - m^2} + c_{ij} \,. \tag{1.100}$$

In particular the possibility that the $g^0$'s can be negative is allowed.

### 1.5.3 Penetration factors

The threshold behavior of low energy scattering of hadrons may be studied in terms of a non-relativistic potential $V$ of range $R$, where $V(r > R) = 0$ the typical behavior of strong interaction. Assuming purely elastic scattering of spin zero particles the potential in its radial form is given as:

$$V = V(r) + \frac{l(l+1)}{r^2} \tag{1.101}$$

the second term being the centrifugal potential. For the condition $qR \ll l$ near threshold the solutions of the Schrodinger equation approximately can be written in terms of the phase shift $\delta_l$ of the partial wave $l$

$$\tan(\delta_l)(qR \ll l) = 2q \cdot a_l \cdot (q)^{2l} \,. \tag{1.102}$$

The factor $(q)^{2l}$ arises here due to the presence of the centrifugal potential and is accordingly called "penetration factor". The factor $a_l$ is constant and is the "scattering length".

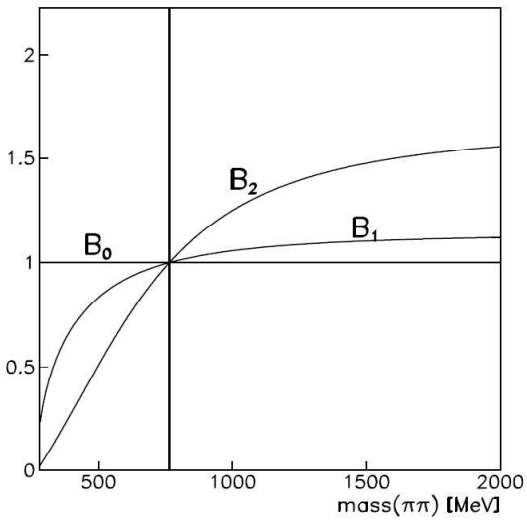


Figure 1.8: *Ratios $B_l(m, m_\alpha) = F_l(m)/F_l(m_\alpha)$ of Blatt-Weisskopf factors using a resonance mass $m_\alpha = 765\ MeV/c^2$ (marked by the line) for $l = 0, 1, 2$.*

The pion creation of nuclear resonances is inadequately described by only $q^{2l}$. Hence, Blatt-Weisskopf [35] proposed the more general form of the penetration factor which is obtained by solving the radial equation for all $qR$. With these factors, the fits to the (low-energy) cross sections become more reasonable. Widely used are Blatt-Weisskopf barrier factors according to Ref. [36]. They are given in terms of the ratio $z = (q/q_R)^2$, where $q_R$ corresponds to the range of the interaction. The factors $F_l(z)$, normalized to $F_l(1) = 1$, up to angular momenta $l = 2$ are:

$$\begin{aligned} F_0(z) &= 1\ , \\ F_1(z) &= \sqrt{\frac{2z}{z+1}}\ , \\ F_2(z) &= \sqrt{\frac{13z^2}{(z-3)^2+9z}}\ . \end{aligned} \tag{1.103}$$

In general, the penetration factors are part of a more complex form factor. The form factors parameterize the underlying interaction (vertexes) (as already here a strong potential is assumed). Hence, they introduce a model dependence in the analysis. In many formulations phenomenological corrections are added to the penetration factors, which due to their small in influence on the lineshape of resonances in practice are indistinguishable on data.

Fig. 1.8 shows the ratios $B_l(m, m_\alpha) = \frac{F_l(m)}{F_l(m_\alpha)}$ of Blatt-Weisskopf factors using a reso-

nance mass $m_\alpha = 765$ MeV/$c^2$ for $l = 0, 1, 2$.

### 1.5.4 One channel resonances

In the case of a single resonance with one single channel opened, the $K$-matrix assumes the form:

$$K = \frac{m_0 \Gamma(m)}{(m_0^2 - m^2)\rho} \tag{1.104}$$

where $m_0$ if the mass of the resonance. The mass dependent width is given by:

$$\Gamma(m) = \Gamma_0 \left( \frac{\rho(m)}{\rho_0} \right) B(q(m), q_0)^2 \ , \tag{1.105}$$

where $\Gamma_0$ is the $K$-matrix width and $q(q_0)$ is the breakup momentum for the mass $m(m_0)$. Neglecting the angular momentum dependence of the amplitude, the invariant scattering amplitude is:

$$T = \frac{m_0 \Gamma_0}{m_0^2 - m^2 - i m_0 \Gamma(m)} B(q(m), q_0)^2 \frac{1}{\rho_0} \ . \tag{1.106}$$

Eq. 1.106 contains the usual Breit-Wigner form. In this simple case observed width and $K$-matrix width are identical. The Breit-Wigner lineshape and the phase shift for the $\rho(770)$ ( $\pi\pi$ elastic scattering) ($m_0 = 765$ MeV/$c^2$, $\Gamma_0 = 110$ MeV/$c^2$) are shown in Fig. 1.9 (a) and (b), respectively. The phase in degree is calculated from the complex amplitude $T$ the following:

$$\delta = 180 \cdot atan(Im(T)/Re(T))/\pi \ . \tag{1.107}$$

Unitarity in the elastic case means, that the amplitude $\rho T$ can be identified with a unitarity circle in the complex plane $(Re(\rho T); Im(\rho T))$ centered at $(0; 0.5)$, which reaches the maximum $i$ at the resonance position. This is the so called Argand diagram displayed in Fig. 1.10. The quantity inelasticity measures the deviation from the unitary circle inwards corresponding to intensity vanishing in the other channels the amplitude couples to. It can be calculated from $T$:

$$\eta = 2 \cdot \sqrt{(Re(\rho T))^2 + (Im(\rho T) - 0.5)^2} \ . \tag{1.108}$$

### 1.5.5 Overlapping resonances

In the case of two resonances of masses $m_A$ and $m_B$ in $\pi\pi$ scattering at mass $m$ the formulation of the $K$-matrix is:

$$K = \frac{m_A \Gamma_A(m)}{m_A^2 - m^2} + \frac{m_B \Gamma_B(m)}{m_B^2 - m^2} \ . \tag{1.109}$$

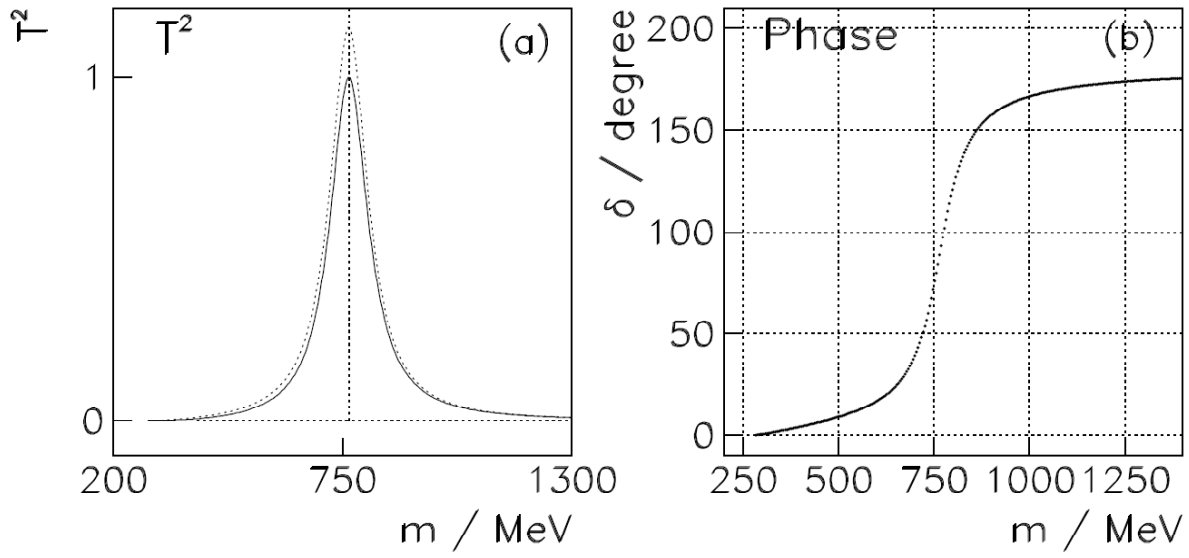


Figure 1.9: **(a):** *Breit-Wigner amplitude squared* ($|\rho T|^2$) *as function of invariant* $\pi\pi$ *mass. The invariant amplitude* $|T|^2$ *is superimposed as dotted line.* **(b):** $\pi\pi$ *phase shift* $\delta$ *which reaches* $90°$ *at the resonance mass.*

The mass dependent widths are given by:

$$\Gamma_\alpha(m) = \Gamma_{\alpha 0} \left(\frac{m_\alpha}{m}\right) \left(\frac{q}{q_\alpha}\right) B(q, q_\alpha)^2 \ . \tag{1.110}$$

In the case $|m_B - m_A| \gg |\Gamma_B + \Gamma_A|$ the $K$-matrix is dominated by either the first or the second resonance, depending whether $m$ is near $m_A$ or $m_B$. The transition amplitude $T$ is then approximately:

$$T \simeq \left[\frac{m_A \Gamma_A(m)}{m_A^2 - m^2 - i m_A \Gamma_A(m)}\right] + \left[\frac{m_B \Gamma_B(m)}{m_B^2 - m^2 - i m_B \Gamma_B(m)}\right] \tag{1.111}$$

that is the sum of two Breit-Wigner.

In the case of $m_0 = m_A = m_B$

$$T = \frac{m_0(\Gamma_A(m) + \Gamma_B(m))}{m_0^2 - m^2 - i m_0(\Gamma_A(m) + \Gamma_B(m))} \tag{1.112}$$

that is a single Breit-Wigner form with the total width being the sum of the individuals widths.

Fig. 1.11 shows that the unitarity is violated when two Breit-Wigner amplitude are added: $T_A + T_B$ instead of $T$ from $(K_A + K_B)$.

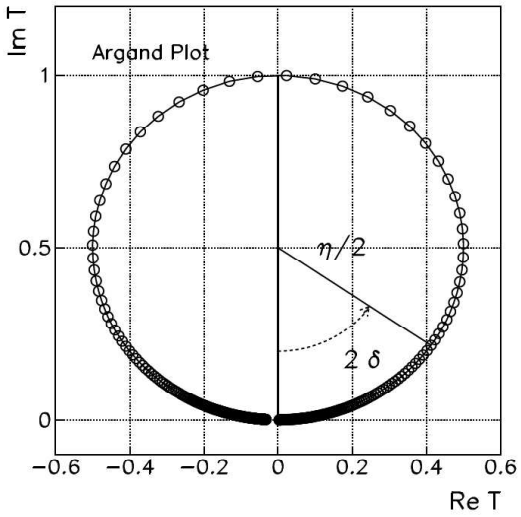


Figure 1.10: *Argand diagram of the Breit-Wigner amplitude $\rho T$: $(Re(\rho T); Im(\rho T))$. Since the process is completely elastic unitarity demands that the amplitude follows the unity circle. The dots are plotted at equidistant $\pi\pi$ masses. The circle starts at (0,0). The phase shift $\delta$ and the inelasticity are marked.*

### 1.5.6 The P-vector formalism

So far "formation" of resonances, observed in two-body scattering $ab \to cd$ has been considered. The $K$-matrix formalism can be generalized to describe the case of "production" of resonances in more complex reactions. The key assumption is that the two-body system in the final state does not simultaneously interact with the rest of the final state. This model is called "isobar model" (See Fig. 1.12). One of the most important approach is the $P$-vector formalism.

To preserve the two-body unitarity an approach was proposed by Aitchison [37]. The Lorentz invariant amplitude, $F$, is given as:

$$F = (I - iK\rho)^{-1}P = TK^{-1}P \ . \tag{1.113}$$

This introduces the production vector $P$ parameterizing the resonance production in the open channels. For n contributing channels $P$ and $F$ are n-dimensional column vectors.

If the $K$-matrix is given as a sum of poles (Eq. 1.90), then the corresponding $P$-vector is:

$$P_i = \sum_\alpha \frac{\beta_\alpha B_{L;\alpha i}(p_i, p_{\alpha i}) g^0_{\alpha i} B_{l;\alpha i}(q_i, q_{\alpha i})}{m^2_\alpha - m^2} \ , \tag{1.114}$$

where $\beta_\alpha$ (expressed in units of energy) carries the coupling of the resonance $\alpha$ to the initial

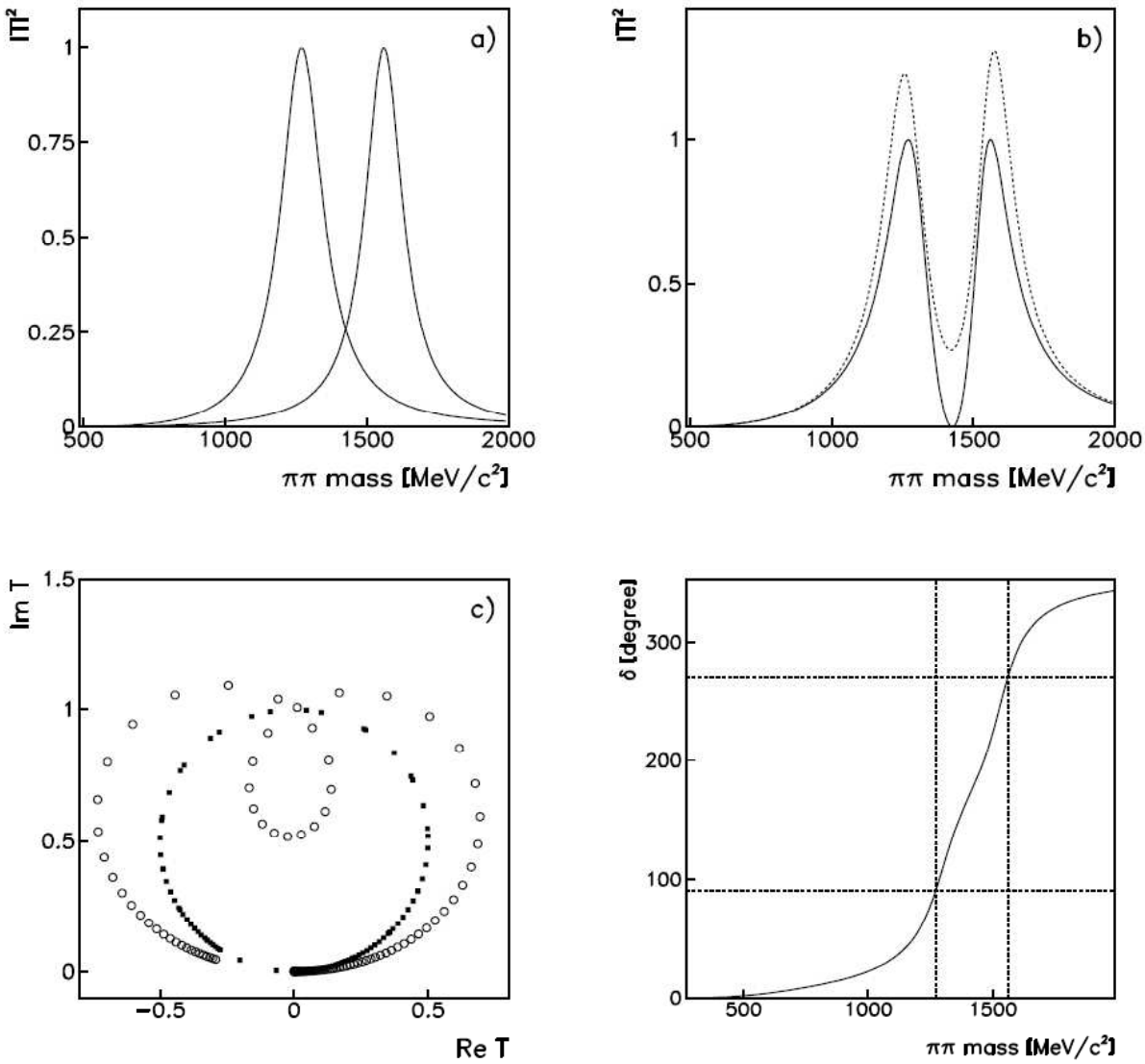


Figure 1.11: *Two overlapping resonances with the parameters:* $m_A = 1270\ MeV/c^2$, $\Gamma_A = 180\ MeV/c^2$, $m_B = 1560\ MeV/c^2$, $\Gamma_B = 160\ MeV/c^2$. *The plot (a) shows the amplitude squared,* $|T|^2$, *for the two individual Breit-Wigner resonances. Plot (b) shows the result of adding the resonance poles in the K-matrix (solid line). The dashed line corresponds to the naive sum of the two Breit-Wigner amplitudes* $|T_A + T_B|^2$, *which exceeds 1 close to the resonance positions. Also the intensity does not drop to zero between the resonance peaks. Plot (c) shows the corresponding Argand diagrams for the naive summation (open circles) and the K-matrix parameterization (black squares). While the latter follows the unitarity circle the Breit-Wigner summation clearly is outside the unity circle in contradiction to the unitarity requirement. Plot (d) shows the phase motion for the K-matrix parameterization, where dashed lines mark the 900 and 2700 steps which cross the phase shift at the masses* $m_A$ *and* $m_B$.

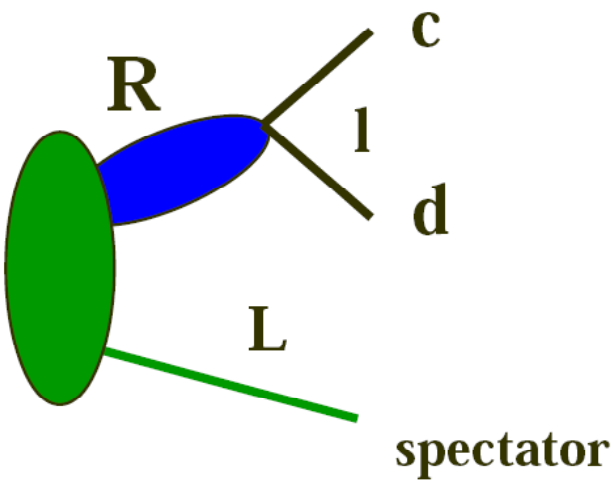


Figure 1.12: *Isobar model: the two-body system in the final state does not simultaneously interact with the rest of the final state.*

state. The centrifugal barrier factor, $B_{L;\alpha i}(p_i, p_{\alpha i})$, is introduced ad hoc and depends on the angular momentum in the production $L$. It is a function of the recoil momentum $p_i$ of the resonance against the spectator.

The constant $\beta_\alpha$ is in general complex ( $\beta_\alpha = b_\alpha e^{i\phi}$, $\phi$ is a phase due to the initial production process). For convenience $\beta_\alpha$ is formulated in terms of the dimensionless $\beta^0_\alpha$

$$\beta_\alpha = \beta^0_\alpha \sqrt{\sum_i (g^0_{\alpha i})^2} \ . \tag{1.115}$$

In the Case of an isolated resonance in a single channel, the P-vector is parameterized as:

$$P = \beta_0 \cdot B_L(p, p_0) \cdot \frac{g_0^2 B_l(q, q_0)}{m_0^2 - m^2} \tag{1.116}$$

and Eq. 1.90 is written as:

$$K = \frac{g_0^2 B_l^2(q, q_0)}{m_0^2 - m^2} \ . \tag{1.117}$$

The Lorentz invariant amplitude, $F$, is given as:

$$F(m) = \beta_0 \cdot B_L(p, p_0) \cdot \frac{m_0 \Gamma_0}{m_0^2 - m^2 - i m_0 \Gamma(m)} \frac{B_l(q, q_0)}{\rho_0} \ . \tag{1.118}$$

This is the relativistic Breit-Wigner form multiplied by an arbitrary complex constant (production strength) $\beta_0$ and the centrifugal factor $B_L(p, p_0)$. This form obtained with the $K$-matrix model is equivalent to the one obtained with the Breit-Wigner model.

# Chapter 2

# BaBar Experiment at PEP-II

## 2.1 Introduction

The primary goal of the *BaBar* experiment is the study of $CP$-violating asymmetries in the decay of the $B$ meson. Secondary goals are precision measurement of decays of bottom and charm mesons and of $\tau$ leptons, searches for rare processes accessible because of the high luminosity of PEP-II $B$-Factory.

The PEP-II $B$-Factory is an $e^+e^-$ asymmetric collider running at a center of mass energy of 10.58 GeV corresponding to the mass of the $\Upsilon(4S)$ resonance. The small Q-value of the $\Upsilon(4S) \to B\bar{B}$ decay results in $B$ mesons almost at rest in the center of mass frame. The electron beam in the High Energy Ring (HER) has 9.0 GeV and the positron beam in the Low Energy Ring (LER) has 3.1 GeV. The $\Upsilon(4S)$ is therefore produced with a Lorentz boost of $\beta\gamma = 0.56$. This boost makes it possible to reconstruct the decay vertexes of the two $B$ mesons, to determine their relative decay times $\Delta t$, and thus to measure the time dependence of their decay rates, since, without boost, this distance would be too small ($\sim 30\ \mu$) to be measured by any vertex tracker.

The *BaBar* detector [38] has been optimized to reach the primary goal of the $CP$ asymmetry measurement. This measurement needs the complete reconstruction of a $B$ decay in a $CP$ eigenstate, the flavor identification (tagging) of the non-$CP$ $B$ and a measure of the distance of the two decay vertexes. To fulfill these needs, a very good vertex resolution, both transverse and parallel to the beam direction, excellent reconstruction efficiency for charged particles and a very good momentum resolution, efficient electron and muon identification, with low misidentification probabilities for hadrons, are required.

A longitudinal section of the *BaBar* detector is shown in Fig. 2.1. The detector inner

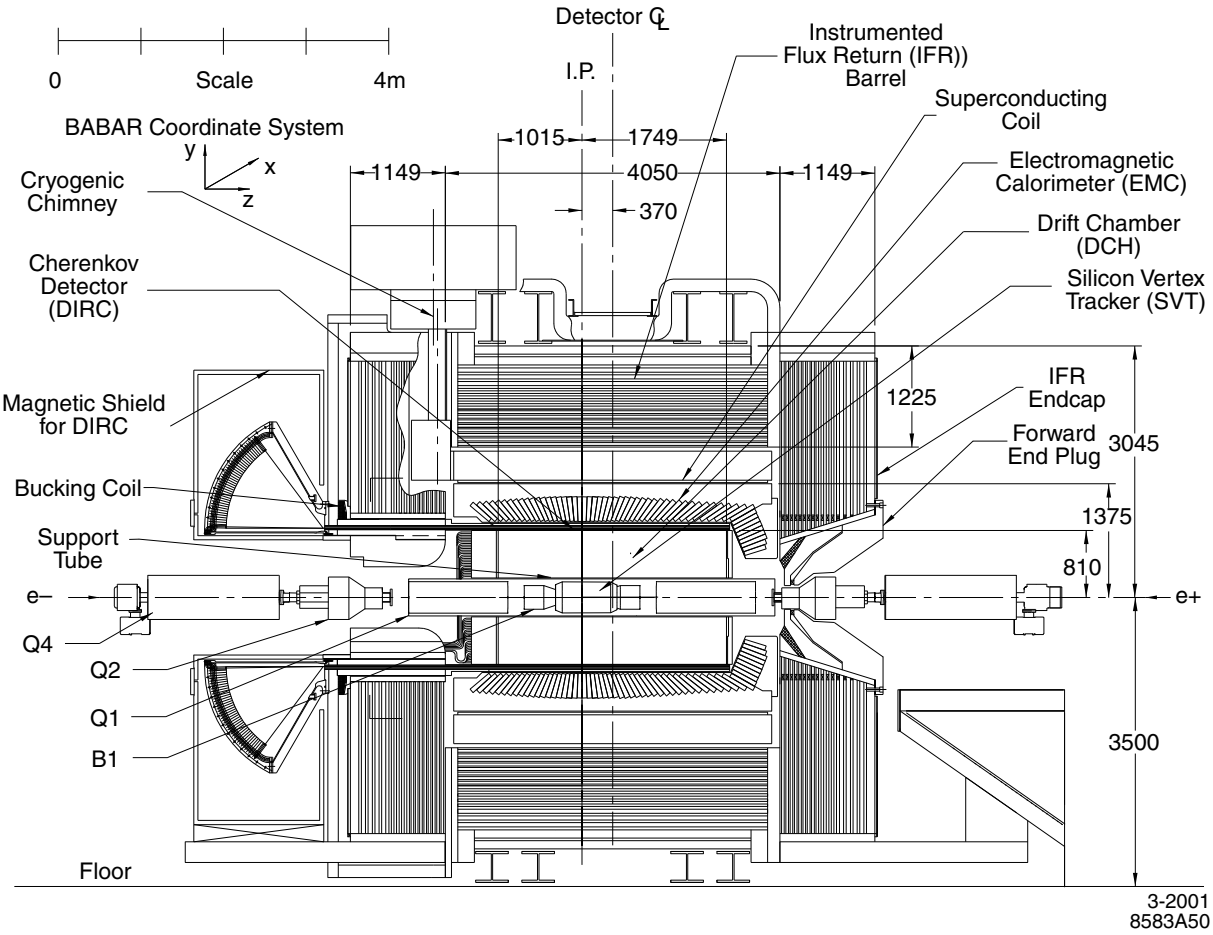


Figure 2.1: *BaBar detector longitudinal section.*

most part is reserved for the silicon vertex tracker (SVT), then there is the drift chamber (DCH), the Cerenkov light detector (DIRC) and the CsI electromagnetic calorimeter (EMC). All those detector sub-systems are surrounded by a solenoidal superconductor magnetic field. The iron used for the return flux has been instrumented (IFR) for muons and neutral hadrons, like $K_L$ and neutrons, detection.

The detector geometry is cylindrical in the inner zone and hexagonal in the outermost zone: the central part of the structure is called *barrel* and it's closed forward and backward by *end caps*. The covered polar angle ranges from 350 mrad, in the forward, to 400 mrad in the backward directions (defined with respect to the high energy beam direction). The *BaBar* coordinate system has the $z$ axis along the boost direction (or the beam direction): the $y$ axis is vertical and the $x$ axis is horizontal and goes toward the external part of the ring. In order to maximize the geometrical acceptance for $\Upsilon(4S)$ decays the whole

detector is offset, with respect to the beam-beam interaction point (IP), by 0.37 m in the direction of the lower energy beam.

A trigger system is used to separate collisions producing interesting events from those that constitutes the noise, or the background, for instance, beam interactions with residual gas. The trigger system is divided in two consequent levels: the level one trigger ($L1$) is hardware based and is designed to have a maximum output rate of 2 $kHz$ and a maximum time delay of 12 $\mu$s, while the other level ($L3$), software based, has a throughput rate limited to 120$Hz$ in order to permit an easy storage and processing of collected data.

## 2.2 PEP-II B Factory

PEP-II is a system consisting of two accumulating asymmetric rings designed in order to operate at a center of mass energy of the $\Upsilon(4S)$ resonance mass, 10.58 GeV. Tab. 2.1 shows the various sub-systems parameters: a comparison between typical and design values is presented. As can be easily seen from the table, PEP-II parameters have exceeded the project ones in terms of instant luminosity and daily integrated luminosity achieving recently the peak value of $1 \times 10^{34}$ $cm^{-2}$ $s^{-1}$ with a daily integrated luminosity of 700 $pb^{-1}$.

| Parameters | Design | Typical |
|---|---|---|
| Energy HER/LER (GeV) | 9.0/3.1 | 9.0/3.1 |
| Current HER/LER (A) | 0.75/2.15 | 1.48/2.5 |
| # of bunch | 1658 | 553-829 |
| bunch time separation (ns) | 4.2 | 6.3-10.5 |
| $\sigma_{Lx}$ ($\mu m$) | 110 | 120 |
| $\sigma_{Ly}$ ($\mu m$) | 3.3 | 5.6 |
| $\sigma_{Lz}$ ($\mu m$) | 9000 | 9000 |
| Luminosity ($10^{33}$ $cm^{-2}s^{-1}$) | 3 | 9 |
| Daily average integrated luminosity ($pb^{-1}/d$) | 135 | 700 |

Table 2.1: *PEP-II beam parameters. Design and typical values are quoted.*

Data is mostly collected at $\Upsilon(4S)$ peak energy. Tab. 2.2 shows the active processes cross sections breakdown at peak energy. From now on the production of light quark pairs $(u, d, s)$ and *charm* quark pairs will be referred to as "continuum production". In order to study this non-resonant production $\sim 12\%$ of data is collected with a center of mass energy 40 MeV below the $\Upsilon(4S)$ mass value.

PEP-II measures radiative Bhabha scattering to provide a luminosity fast monitor

| $e^+e^- \rightarrow$ | Cross section (nb) |
|---|---|
| $b\bar{b}$ | 1.05 |
| $c\bar{c}$ | 1.30 |
| $s\bar{s}$ | 0.35 |
| $u\bar{u}$ | 1.39 |
| $d\bar{d}$ | 0.35 |
| $\tau^+\tau^-$ | 0.94 |
| $\mu^+\mu^-$ | 1.16 |
| $e^+e^-$ | $\sim 40$ |

Table 2.2: *Various processes cross sections at* $\sqrt{s} = M_{\Upsilon(4S)}$. *Bhabha cross section is an effective cross section, within the experimental acceptance.*

useful for operations. *BaBar* derives the absolute luminosity offline from other QED processes, mainly $e^+e^-$ and $\mu^+\mu^-$ pairs: the systematic uncertainty on the absolute value of the luminosity is estimated to be about 1.5%. This error is dominated by uncertainties in the Monte Carlo generator and the simulation of the detector.

The beam energies of the two beams are calculated from the total magnetic bending strength and the average deviations of the accelerating frequencies from their central values. The systematic error on the PEP-II calculation of the absolute beam energies is estimated to be $5 - 10$ MeV, while the relative energy setting for each beam is accurate and stable to about 1 MeV.

The interaction region design, with the two beams crossing in a single interaction point with particles trajectories modified in order to have head on collisions, is realized with a magnetic field, produced by a dipole magnetic system, acting near the interaction point. The collision axis is off-set from the $z$-axis of the *BaBar* detector by about 20 mrad in the horizontal plane to minimize the perturbation of the beams by the solenoidal field. In this configuration the particles and the beams are kept far apart in the horizontal plane outside the interaction region and parasite collisions are minimized. Magnetic quadrupoles included inside the detector's magnetic field, and hence realized in Samarium-Cobalt, are strongly focusing the beams inside the interaction region.

In order to keep track of PEP-II beams displacement with respect to the *BaBar* detector, the interaction point position is computed on periodic intervals, using two-track events. Interaction region dimensions (beam-spot) computed in that way are $\sim 150\ \mu m$ along $x$, $\sim 50\ \mu m$ along $y$ and $1\ cm$ along $z$ axis. The $y$ dimension estimate is completely

dominated by tracking resolution and can be improved by looking at luminosity variations as a function of relative beams position. In particular, knowing the beam currents and the $x$ beam-spot dimension, it is possible to get a resolution on $y$ ($\sigma_y$) $\sim 5\ \mu m$, value that remain stable within 10% in a one hour time scale. Those measurements can be also verified offline by measuring the primary vertex of multi-hadron events [1].

Fig. 2.2 shows the integrated luminosity obtained by PEP-II and collected by *BaBar* from the beginning of data taking (November 1999) to the end of September 2005. This analysis will make use only of data collected in **Run 1-4** data taking periods (before August 2004). This data sample corresponds to an integrated luminosity of 208 $fb^{-1}$ recorded at the $\Upsilon(4S)$ resonance, corresponding to $218 \cdot 10^6$ $B\bar{B}$ couples, and 21.6 $fb^{-1}$ collected at a center-of-mass energy 40 MeV below.

## 2.3 Tracking system

The charged particle tracking system consists of two different components: the silicon vertex tracker (SVT) and the drift chamber (DCH). The main purpose of this tracking system is the efficient detection of charged particles and the measurement of their momentum and angles with high precision. These track measurements are important for the extrapolation to the DIRC, the EMC and the IFR. At lower momenta, the SVT measurements are more important while at higher momenta the DCH dominates.

### 2.3.1 The Silicon Vertex Tracker: SVT

The vertex detector has a radius of 20 $cm$ from the primary interaction region: it is placed inside the support tube of the beam magnets and consists of five layers of double-sided silicon strip sensors detectors to provide five measurements of the positions of all charged particles with polar angles in the region $20.1 < \theta < 150$. Because of the presence of a $1.5\,T$ magnetic field, the charged particle tracks with transverse momenta lower than $\sim 100$ MeV/$c$ cannot reach the drift chamber active volume. So the SVT has to provide stand-alone tracking for particles with transverse momentum less than 120 MeV/$c$, the minimum that can be measured reliably in the DCH alone. This feature is essential for

[1] By reconstructing all the tracks in one event it is possible to have an estimate of primary vertex position: $\Upsilon(4S)$ decay point in transversal plane. Given that the boost along the $z$ axis produces a relative displacement of the two $B$ mesons this method has a relative poor resolution that get worse in presence of long-lived particles.

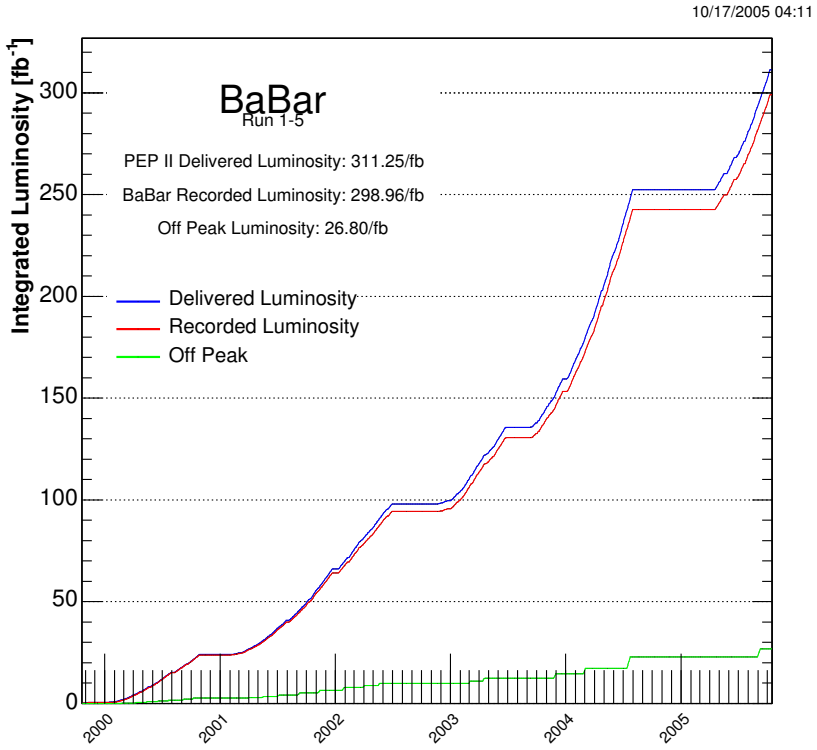


Figure 2.2: *Integrated luminosity and obtained by PEP-II and collected by BaBar from November 1999 to September 2005.*

the identification of slow pions from $D^{*-}$ meson decays. Because of these, the SVT has to provide redundant measurements.

Beyond the stand-alone tracking capability, the SVT provides the best measurement of track angles which is required to achieve design resolution for the Cerenkov angle for high momentum tracks. The SVT is very close to the production vertex in order to provide a very precise measure of points on the charged particles trajectories on both longitudinal ($z$) and transverse directions. The longitudinal coordinate information is necessary to measure the decay vertex distance, while the transverse information allows a better separation between secondary vertexes coming from decay cascades.

More precisely, the design of the SVT was carried out according to some important guidelines:

- The number of impact points of a single charged particle has to be greater than 3 to make a stand-alone tracking possible, and to provide an independent momentum

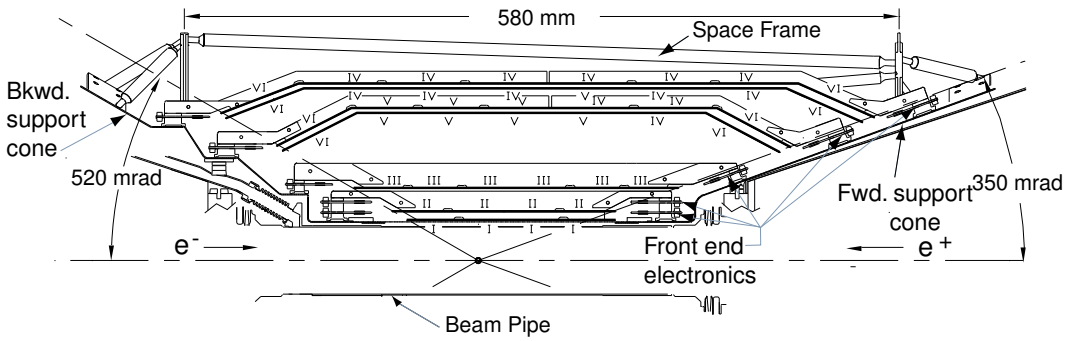


Figure 2.3: *SVT schematic view: longitudinal section*

measure.

- The first three layers are placed as close as possible to the impact point to achieve the best resolution on the $z$ position of the $B$ meson decay vertexes.

- The two outer layers are close to each other, but comparatively far from the inner layers, to allow a good measurement of the track angles.

- The SVT must withstand 2 MRad of ionizing radiation: the expected radiation dose is 1 Rad/day in the horizontal plane immediately outside the beam pipe and 0.1 Rad/day on average.

- Since the vertex detector is inaccessible during normal detector operations, it has to be reliable and robust.

These guidelines have led to the choice of a SVT made of five layers of double-sided silicon strip sensors. The spatial resolution, for perpendicular tracks must be $10 - 15\,\mu m$ in the three inner layers and about $40\,\mu m$ in the two outer layers. The three inner layers perform the impact parameter measurement, while the outer layers are necessary for pattern recognition and low $p_t$ tracking. The silicon detectors are double-sided (contain active strips on both sides) because this technology reduces the thickness of the materials the particles have to cross, thus reducing the energy loss and multiple scattering probability compared to single-sided detectors. The sensors are organized in modules (Fig. 2.3). The SVT five layers contain 340 silicon strip detectors with AC-coupled silicon strips.

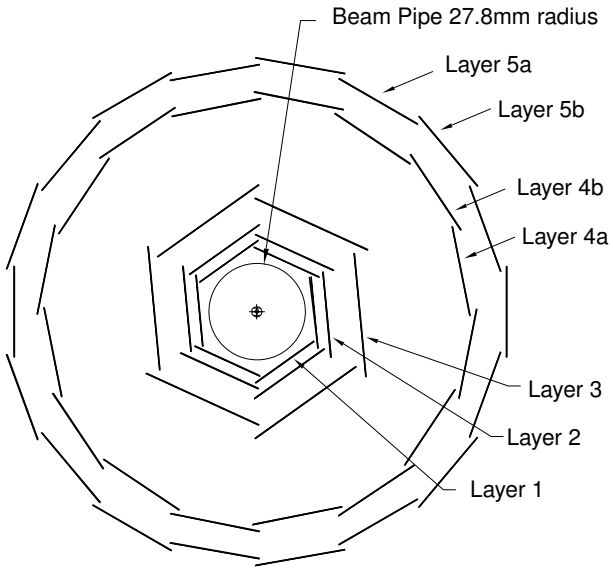


Figure 2.4: *Cross-sectional view of the SVT in a plane perpendicular to the beam axis.*

Each detector is $300\,\mu m$-thick but sides range from $41\,mm$ to $71\,mm$ and there are 6 different detector types. Each of the three inner layers has a hexagonal transverse cross-section and it is made up of 6 detector modules, arrayed azimuthally around the beam pipe, while the outer two layers consist of 16 and 18 detector modules, respectively. The inner detector modules are barrel-style structures, while the outer detector modules employ the novel arch structure in which the detectors are electrically connected across an angle. This arch design was chosen to minimize the amount of silicon required to cover the solid angle while increasing the solid angle for particles near the edges of acceptance: having incidence angles on the detector closer to 90 degrees at small dip angles insures a better resolution on impact points. One of the main features of the SVT design is the mounting of the readout electronics entirely outside the active detector volume.

The strips on the two sides of the rectangular detectors in the barrel regions are oriented parallel ($\phi$ strips) or perpendicular ($z$ strips) to the beam line: in other words, the inner sides of the detectors have strips oriented perpendicular to the beam direction to measure the $z$ coordinate ($z$-size), whereas the outer sides, with longitudinal strips, allow the $\phi$-coordinate measurement ($\phi$-side). In the forward and backward regions of the two outer layers, the angle between the strips on the two sides of the trapezoidal detectors is approximately 90 and the $\phi$ strips are tapered.

The inner modules are tilted in $\phi$ by 5, allowing an overlap region between adjacent

modules: this provide full azimuthal coverage and is convenient for alignment. The outer modules are not tilted, but are divided into sub-layers and placed at slightly different radii (see Fig. 2.4).

The total silicon area in the SVT is $0.94\,m^2$ and the number of readout channels is about 150 000. The geometrical acceptance of SVT is 90% of the solid angle in the c.m. system and typically 80% are used in charged particle tracking.

The $z$-side strips are connected to the read-out electronics with flexible *Upilex* fanout circuits glued to the inner faces of half-modules: as a matter of fact, each module is divided into two electrically separated forward and backward half-modules. The fanout circuits consist of conductive traces on a thin flexible insulator (copper traces on Kapton): the traces are wire-bonded to the end of the strips.

In the two outer layers, in each module the number of $z$ strips exceeds the number of read-out channels, so that a fraction of the strips is "ganged", i.e., two strips are connected to the same read-out channel. The "ganging" is performed by the fanout circuits. The length of a $z$ strip is about $50\,\mu m$ (case of no ganging) or $100\,\mu m$ (case of two strip connected): the ganging introduces an ambiguity on the $z$ coordinate measurement, which must be resolved by the pattern recognition algorithms. The $\phi$ strips are daisy-chained between detectors, resulting in a total strip length of up to $26\,cm$. Also, for the $\phi$-side, a short fanout extension is needed to connect the ends of the strips to the read-out electronics.

| | 1st layer | 2nd layer | 3rd layer | 4th layer | 5th layer |
|---|---|---|---|---|---|
| radius ($mm$) | 32 | 40 | 54 | 91-127 | 114-144 |
| modules/layer | 6 | 6 | 6 | 16 | 18 |
| wafers/module | 4 | 4 | 6 | 7 | 8 |
| read-out pitch ($\mu m$) | | | | | |
| $\phi$ | 50-100 | 55-110 | 55-110 | 100 | 100 |
| $z$ | 100 | 100 | 100 | 210 | 210 |

Table 2.3: *Parameters of the SVT layout: these characteristics are shown for each layer.*

The signals from the read-out strips are processed using a new technique, bringing in several advantages. After amplification and shaping, the signals are compared to a preset threshold and the time they exceed this threshold (time over threshold, or ToT) is

measured. This time interval is related to the charge induced in the strip by the charged particle crossing it. Unlike the traditional peak-amplitude measurement in the shaper output, the ToT has the advantage of an approximately logarithmic relation of the time interval to the charge signal. This compresses the active dynamic range of the signal, ensuring a good sensitivity in the lower range. When a particle crosses a silicon detector a cluster of adjoining strips producing a signal is formed. The good signal resolution in the lower range ensures a good determination of the tails of the cluster thus improving the resolution on the impact point measurement.

The electronic noise measured is found to vary between 700 and 1500 electrons ENC (equivalent noise charge), depending on the layer and the readout view: this can be compared to the typical energy deposition for a minimum ionizing particle at normal incidence, which is equivalent to $\sim 24000$ electrons.

During normal running conditions, the average occupancy of the SVT in a time window of $1\,\mu s$ is about 2% for the inner layers, where it is dominated by machine backgrounds, and less than 1% for the outer layers, where noise hits dominate.

The cluster reconstruction is based on a cluster finding algorithm: first the charge pulse height of a single pulse is calculated form the ToT value and clusters are formed grouping adjacent strips with consistent times. The position $x$ of a cluster formed by $n$ strips is evaluated with an algorithm called "head-to-tail" algorithm:

$$x = \frac{(x_1 + x_n)}{2} + \frac{p}{2}\frac{(Q_n - Q_1)}{(Q_n + Q_1)} \tag{2.1}$$

where $x_i$ and $Q_i$ are the position and the collected charge of i-th strip and $p$ is the read-out pitch. This formula always gives a cluster position within $p/2$ of the geometrical center of the cluster. The cluster pulse height is simply the sum of the strip charges, while the cluster time is the average of the signal times.

The SVT efficiency can be calculated for each half-module by comparing the number of associated hits to the number of tracks crossing the active area of the half-module. Excluding defective readout sections (9 over 208), the combined hardware and software efficiency is 97%.

The spatial resolution of SVT hits is calculated by measuring the distance (in the plane of the sensor) between the track trajectory and the hit, using high-momentum tracks in two prong events: the uncertainty due to the track trajectory is subtracted from the width of the residual distribution to obtain the hit resolution. The track hit residuals are

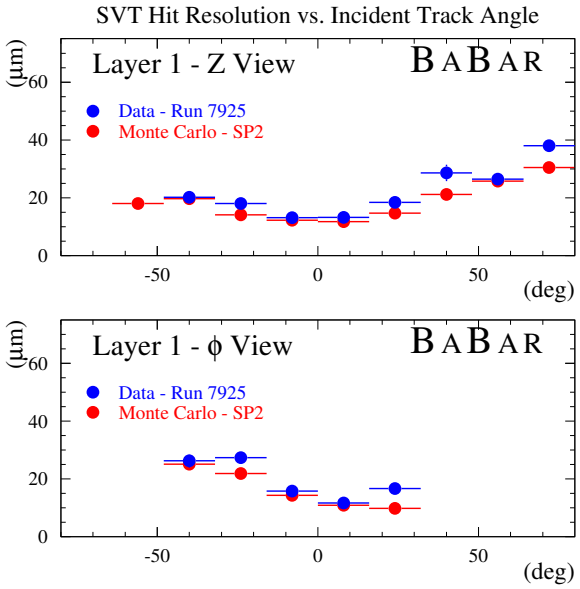


Figure 2.5: *SVT hit resolution in the $z$ and $\phi$ coordinate in microns, plotted as functions of the track incident angle in degrees.*

defined as the distance between track and hit, projected onto the wafer plane and along either the $\phi$ or $z$ direction. The width of this residual distribution is then the SVT hit resolution. Fig. 2.5 shows the SVT hit resolution for $z$ and $\phi$ side hits as a function of the track incident angle: the measured resolutions are in very good agreement with the Monte Carlo expected ones. Over the whole SVT, resolutions are raging from $10-15\,\mu m$ (inner layers) to $30-40\,\mu m$ (outer layers) for normal tracks.

For low-momentum tracks ($p_t < 120$ MeV/$c$), the SVT provides the only particle identification information. The measure of the ToT value enables to obtain the pulse height and hence the ionization $dE/dx$: the value of ToT are converted to pulse height using a look-up table computed from the pulse shapes. The double-sided sensors provide up to ten measurements of $dE/dx$ per track: with signals from at least four sensors, a 60% truncated mean $dE/dx$ is calculated. For MIPs, the resolution on the truncated mean $dE/dx$ is approximately 14%: a $2\sigma$ separation between kaons and pions can be achieved up to momentum of 500 MeV/$c$ and between kaons and protons beyond 1 GeV/$c$.

### 2.3.2 The drift chamber: DCH

The drift chamber is the second part of *BaBar* tracking system. Its principal purpose is the efficient detection of charged particles and the measurement of their momenta and angles with high precision. The DCH complements the measurements of the impact parameter and the directions of charged tracks provided by the SVT near the impact point (IP). At lower momenta, the DCH measurements dominate the errors on the extrapolation of charged tracks to the DIRC, EMC and IFR. The reconstruction of decay and interaction vertexes outside of the SVT volume, for instance the $K_S^0$ decays, relies only on the DCH. For these reasons, the chamber should provide maximal solid angle coverage, good measurement of the transverse momenta and positions but also of the longitudinal positions of tracks with a resolution of $\sim 1\,mm$, efficient reconstruction of tracks at momenta as low as 100 MeV/$c$ and it has to minimally degrade the performance of the calorimeter and particle identification devices (the most external detectors). The DCH also needs to supply information for the charged particle trigger. For low momentum particles, the DCH is required to provide particle identification by measuring the ionization loss ($dE/dx$). A resolution of about 7% allows $\pi/K$ separation up to 700 MeV/$c$. This particle identification (PID) measurement is complementary to that of the DIRC in the barrel region, while in the extreme backward and forward region, the DCH is the only device providing some discrimination of particles of different mass. The DCH should also be able to operate in presence of large beam-generated backgrounds having expected rates of about $5\,kHz$/cell in the innermost layers.

To meet the above requirements, the DCH is a $280\,cm$-long cylinder (see left plot in Fig. 2.6), with an inner radius of $23.6\,cm$ and an outer radius of $80.9\,cm$. It is bounded by the support tube at its inner radius and the particle identification device at its outer radius. The flat end-plates are made of aluminum. Since the *BaBar* events will be boosted in the forward direction, the design of the detector is optimized to reduce the material in the forward end. The forward end-plate is made thinner ($12\,mm$) in the acceptance region of the detector compared to the rear end-plate ($24\,mm$), and all the electronics is mounted on the rear end-plate. The device is asymmetrically located with respect to the IP: the forward length of 174.9 cm is chosen so that particles emitted at polar angles of 17.2° traverse at least half of the layers of the chamber before exiting through the front end-plate. In the backward direction, the length of $101.5\,cm$ means that particles with

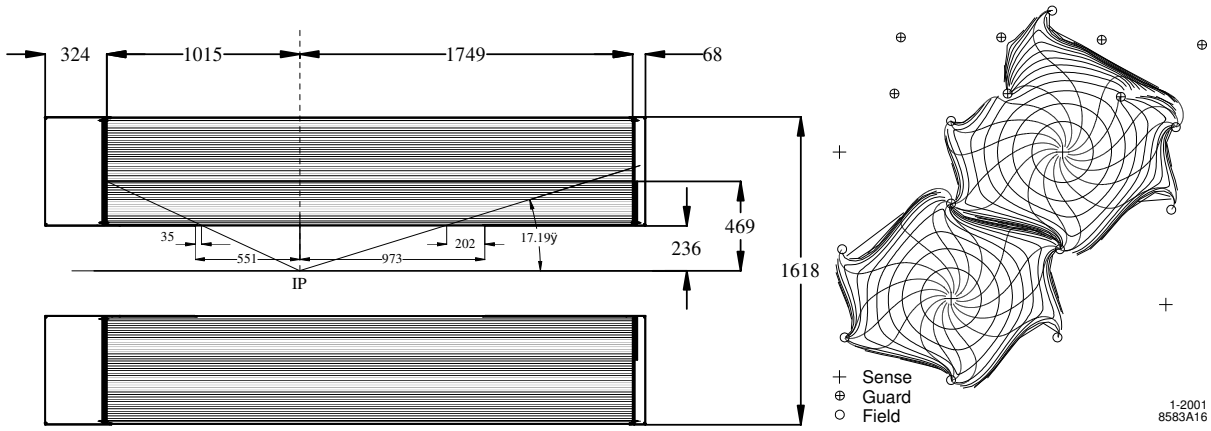


Figure 2.6: *Side view of the BaBar drift chamber (the dimensions are in mm) and isochrones (i.e. contours of equal drift time of ions) in cells of layer* 3 *and* 4 *of an axial super-layer. The isochrones are spaced by* 100 *ns.*

polar angles down to 152.6° traverse at least half of the layers.

The inner cylinder is made of 1 *mm* beryllium and the outer cylinder consists of two layers of carbon fiber glued on a Nomex core: the inner cylindrical wall is kept thin to facilitate the matching of SVT and DCH tracks, to improve the track resolution for high momentum tracks and to minimize the background from photon conversions and interactions. Material in the outer wall and in the forward direction is also minimized in order not to degrade the performance of the DIRC and the EMC.

The region between the two cylinders is filled up by a gas mixture consisting of Helium-isobutane (80% : 20%): the chosen mixture has a radiation length that is five times larger than commonly used argon-based gases. 40 layers of wires fill the DCH volume and form 7104 hexagonal cells with typical dimensions of $1.2 \times 1.9\, cm^2$ along the radial and azimuthal directions, respectively (see right plot in Fig. 2.6). The hexagonal cell configuration has been chosen because approximate circular symmetry can be achieved over a large portion of the cell. Each cell consist of one sense wire surrounded by six field wires: the sense wires are 20 $\mu m$ gold-plated tungsten-rhenium, the field wires are 120 $\mu m$ and 80 $\mu m$ gold-plated aluminum. By using the low-mass aluminum field wires and the helium-based gas mixture, the multiple scattering inside the DCH is reduced to a minimum, representing less than $0.2\% X_0$ of material. The total thickness of the DCH at normal incidence is $1.08\% X_0$.

The drift cells are arranged in 10 super-layers of 4 cylindrical layers each: the super-

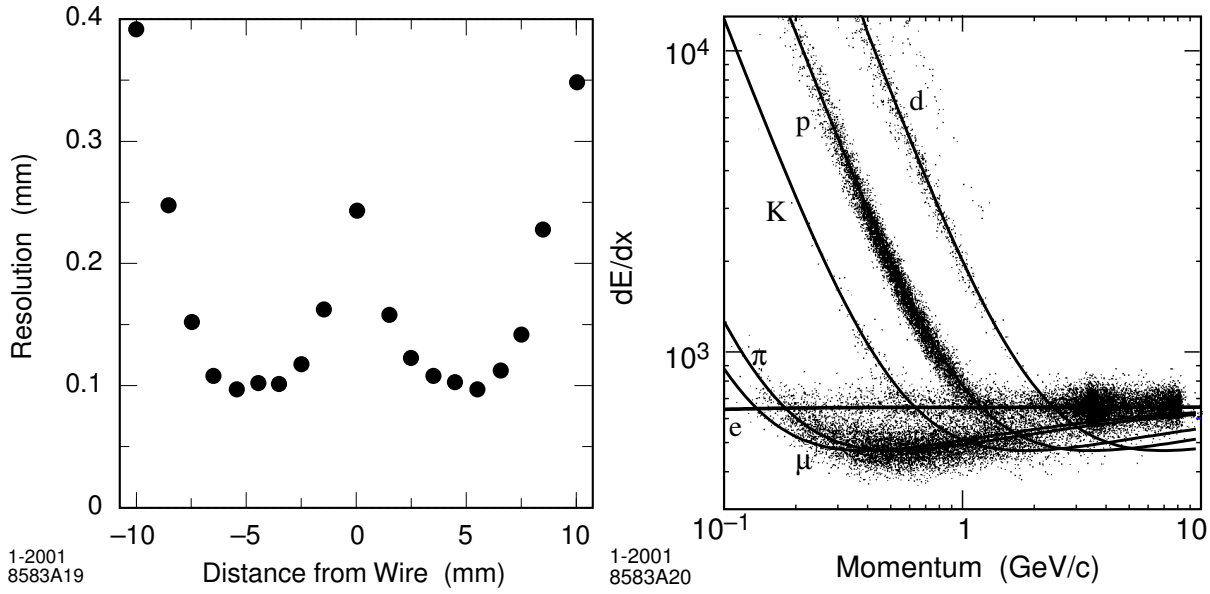


Figure 2.7: **Left plot:** *DCH position resolution as a function of the drift chamber in layer* 18*, for tracks on the left and right side of the sense wire. The data are averaged over all cells in the layer.* **Right plot:** *measurement of $dE/dx$ in the DCH as a function of the track momenta. The data include large samples of beam background triggers as evident from the high rate of protons. The curves show the Bethe-Bloch predictions derived from selected control samples of particles of different masses.*

layers contain wires oriented in the same direction: to measure the $z$ coordinate, axial wire super-layers and super-layers with slightly rotated wires (*stereo*) are alternated. In the stereo super-layers a single wire corresponds to different $\phi$ angles and the $z$ coordinate is determined by comparing the $\phi$ measurements from axial wires and the measurements from rotated wires. The stereo angles vary between $\pm 45 mrad$ and $\pm 76 mrad$.

While the field wires are at ground potential, a positive high voltage is applied to the sense wires: an avalanche gain of approximately $5 \times 10^4$ is obtained at a typical operating voltage of $1960\,V$ and a 80 : 20 helium:isobutane gas mixture.

In each cell, the track reconstruction is obtained by the electron time of flight: the precise relation between the measured drift time and drift distance is determined from sample of $e^+e^-$ and $\mu^+\mu^-$ events. For each signal, the drift distance is estimated by computing the distance of closest approach between the track and the wire. To avoid bias, the fit does not include the hit of the wire under consideration. The estimated drift distances and the measured drift times are averaged over all wires in a layer.

The DCH expected position resolution is lower than $100\,\mu m$ in the transverse plane,

while it is about $1\,mm$ in the $z$ direction. The minimum reconstruction and momentum measure threshold is about 100 MeV/$c$ and it is limited by the DCH inner radius. The design resolution on the single hit is about $140\,\mu m$ while the achieved weighted average resolution is about $125\,\mu m$. Left plot in Fig. 2.7 shows the position resolution as a function of the drift distance, separately for the left and the right side of the sense wire. The resolution is taken from Gaussian fits to the distributions of residuals obtained from unbiased track fits. The results are based on multi-hadron events for data averaged over all cells in layer 18.

The specific energy loss ($dE/dx$) for charged particles through the DCH is derived from the measurement of the total charge collected in each drift cell. The specific energy loss per track is computed as a truncated mean from the lowest 80% of the individual $dE/dx$ measurements. Various corrections are applied to remove sources of bias: these corrections include changes in gas pressure and temperature ($\pm 9\%$ in $dE/dx$), differences in cell geometry and charge collection ($\pm 8\%$), signal saturation due to space charge buildup ($\pm 11\%$), non-linearities in the most probable energy loss at large dip angles ($\pm 2.5\%$) and variation of cell charge collection as a function of the entrance angle ($\pm 2.5\%$).

Right plot in Fig. 2.7 shows the distribution of the corrected $dE/dx$ measurements as a function of track momenta: the superimposed Bethe-Bloch predictions have been determined from selected control samples of particles of different masses. The achieved $dE/dx$ rms resolution for Bhabha events is typically 7.5%, limited by the number of samples and Landau fluctuations, and it is close to the expected resolution of 7%.

## 2.4 Track reconstruction

The reconstruction of charged particle is based on the SVT and the DCH detectors.charged particle tracking has been studied with large samples of cosmic ray muons, $e^+e^-$, $\mu^+\mu^-$ and $\tau^+\tau^-$ events, as well as multi-hadrons.

Charged tracks are defined by five parameters $(d_0, \phi_0, \omega, z_0, \tan\lambda)$ and their associated error matrix. These parameters are measured at the point of closest approach to the $z$-axis; $d_0$ and $z_0$ are the distances of this point from the origin of the coordinate system in the $x$–$y$ plane and along the $z$-axis, respectively. The angle $\phi_0$ is the azimuth of the track, $\lambda$ the dip angle relative to the transverse plane, and $\omega$ is the curvature. $d_0$ and $\omega$ are signed variables; their sign depends on the charge of the track.

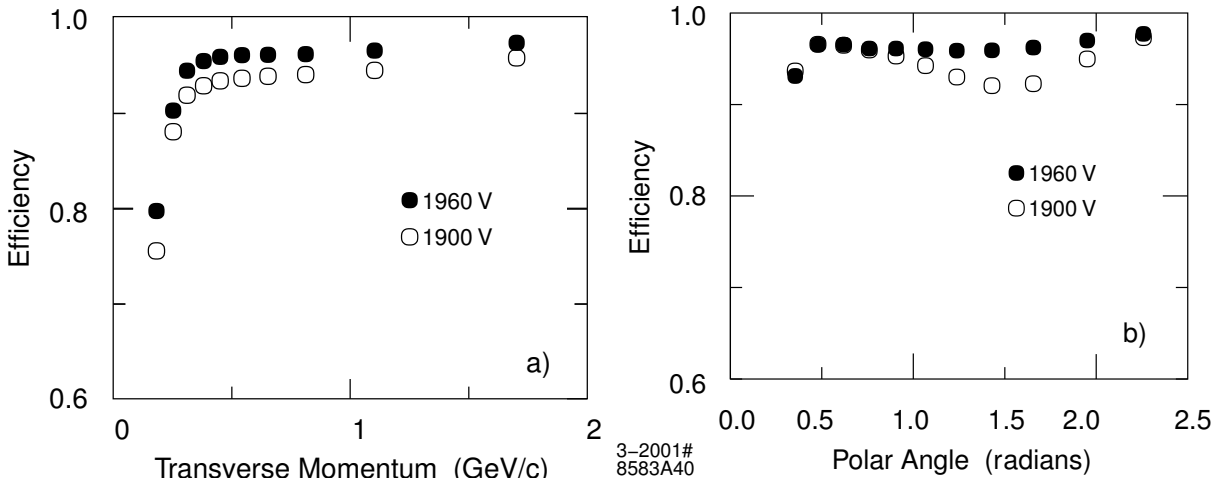


Figure 2.8: *Track reconstruction efficiency in the DCH at operating voltages of* $1960\,V$ *and* $1900\,V$ *as a function of transverse momentum (left plot) and of polar angle (right plot). The efficiency is measured in multi-hadron events.*

The track finding and the fitting procedures make use of Kalman filter algorithm [39] [40] that takes into account the detailed distribution of material in the detector and the full map of the magnetic field. First of all, tracks are reconstructed with DCH hits through a stand-alone DCH algorithm, the resulting tracks are then extrapolated into the SVT and SVT track segments are added and a Kalman fit is performed to the full set of DCH and SVT hits. Any remaining SVT are passed to the SVT stand-alone track finding algorithms. Finally, an attempt is made to combine tracks that are only found by one of the two tracking systems and thus recover tracks scattered in the material of the support tube.

The efficiency for track reconstruction in the DCH has been measured as a function of transverse momentum, polar and azimuthal angles in multi-track events. These measurement rely on specific final states and exploit the fact that the track reconstruction can be performed independently in the SVT and the DCH. The absolute DCH tracking efficiency is determined as the ratio of the number of reconstructed DCH tracks to the number of tracks detected in the SVT with the requirement that they fall within the acceptance of the DCH. Left plot in Fig. 2.8 shows the efficiency in the DCH as a function of transverse momentum in multi-hadron events.

At design voltage of $1960\,V$, the efficiency averages $98\pm1\%$ per track above $200\ \mathrm{MeV}/c$: the data recorded at $1900\,V$ show a reduction in efficiency by about 5% for tracks almost

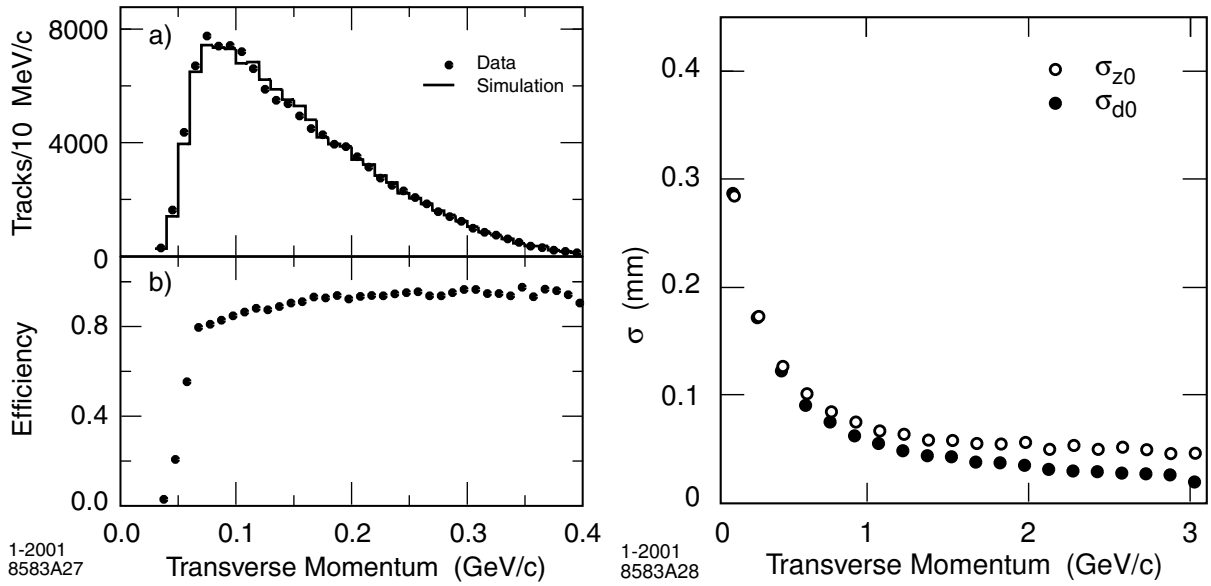


Figure 2.9: **Left plot:** *Monte Carlo studies of low momentum tracks in the SVT on* $D^{*+} \to D^0\pi^+$ *events. a) comparison with data in* $B\bar{B}$ *events and b) efficiency for slow pion detection derived from simulated events.* **Right plot:** *resolution in the parameters* $d_0$ *and* $z_0$ *for tracks in multi-hadron events as a function of the transverse momentum.*

at normal incidence, indicating that the cells are not fully efficient at this voltage (see right plot in Fig. 2.8).

The stand-alone SVT tracking algorithms have a high efficiency for tracks with low transverse momentum: to estimate the tracking efficiency for these low momentum tracks, a detailed Monte Carlo study was performed. The pion spectrum was derived from simulation of the inclusive $D^*$ production in $B\bar{B}$ events and Monte Carlo events were selected in the same way as the data: since the agreement with Monte Carlo is very good, the detection efficiency has been derived from Monte Carlo simulation. The SVT extends the capability of the charge particle reconstruction down to transverse momenta of $\sim 50$ MeV/$c$ (see left plot in Fig. 2.9).

The resolution in the five track parameters is monitored using $e^+e^-$ and $\mu^+\mu^-$ pair events: the resolution is derived from the difference of the measured parameters for the upper and lower halves of the cosmic ray tracks traversing the DCH and the SVT. On this sample with transverse momenta above 3 GeV/$c$, the resolution for single tracks is $23\,\mu m$ in $d_0$ and $29\,\mu m$ in $z_0$. To study the dependence of resolution from transverse momentum, a sample of multi-hadron events is used: the resolution is determined from the width of the distribution of the difference between the measured parameters ($d_0$ and $z_0$) and the

coordinates of the vertex reconstructed from the remaining tracks in the event: right plot in Fig. 2.9 shows the dependence of the resolution in $d_0$ and $z_0$ as a function of $p_t$. The measured resolutions are about $25\,\mu m$ in $d_0$ and $40\,\mu m$ in $z_0$ for $p_t$ of 3 GeV/$c$: these values are in good agreement with the Monte Carlo studies and in reasonable agreement also with the results from cosmic rays.

Besides the criteria described above the tracks selected for this analysis are requested to satisfy additional requests:

- A cut on the distance of closest approach to the beam spot in the $x - y$ plane ($|d_{xy}| < 1.5\ cm$) and along the $z$ axis ($|d_z| < 10\ cm$) is applied. This reduces fake tracks and background tracks not originating from the vicinity of the interaction point. This cut is not applied to the tracks coming from the $K_S$ decay since the $K_S$ decay vertex is distant from the interaction point.

- For tracks with $p_\perp > 0.2$ GeV/$c$ at least one DCH hit is required. This cut is not used for low momentum tracks since slow pions produced (for instance in the $D^* \to D^0\pi$ decays) would be rejected.

- A cut on the maximum momentum of $p_{lab} < 10$ GeV/$c$, where $p_{lab}$ is the laboratory momentum of the track is applied. This removes tracks not compatible with the beam energies.

- Tracks are required to be within the polar angle acceptance of the detector: $0.410 < \theta_{lab} < 2.54$ rad. This ensures a well-understood tracking efficiency.

- Tracks with transverse momentum $p_\perp < 0.18$ GeV/$c$ do not reach the EMC and therefore they will spiral inside the drift chamber ("loopers"). The tracking algorithms of *BaBar* will not combine the different fragments of these tracks into a single track. Therefore dedicated cuts have been developed to reject track fragments compatible with originating from a looper based on their distance from the beam spot. In order to identify looper candidates, the minimal difference in $p_\perp$, $\phi$ and $\theta$ to all other tracks in the event is determined. Tracks passing selection criteria (see Tab. 2.4), different for same-sign and opposite-sign track pairs, are flagged as loopers and only the track fragment with $|d_z|$ closest to the beam spot is retained.

  These criteria remove roughly 13% of all low-momentum tracks in the central part

of the detector. On average, they lower the mean charged multiplicity per $B$ meson by less than 1%.

- Two tracks very closely aligned to each other are called "ghosts". These cases arise when the tracking algorithms splits the DCH hits in two track fragments. If two tracks are very close in phase space (as defined in Tab. 2.4), only the track with the largest number of DCH hits is retained. This ensures that the fragment with the better momentum measurement is kept in the analysis.

| Select tracks with | Selection criteria |
|---|---|
| distance in $x-y$ plane | $\|d_{xy}\| < 1.5\ cm$ |
| distance in $z$ axis | $\|d_z\| < 10\ cm$ |
| minimum number of DCH hits | $N_{DCH} > 0$ if $p_\perp > 0.2$ GeV/$c$ |
| maximum momentum | $p_{lab} < 10$ GeV/$c$ |
| geometrical acceptance | $0.410 < \theta_{lab} < 2.54$ rad |
| Reject tracks if | $\Delta p_t = 100$ MeV/$c$ to other tracks and |
| loopers ($p_\perp < 0.18$ GeV/$c$) | Same sign: $\|\Delta\phi\| < 220$ & $\|\Delta\theta\| < 215$ mrad<br>Opposite sign: $\|\Delta\phi\| < 190$ & $\|\Delta\theta\| < 300$ mrad |
| ghosts ($p_\perp < 0.35$ GeV/$c$) | $\|\Delta\phi\| < 220$ & $\|\Delta\theta\| < 215$ mrad |

Table 2.4: *Summary of track selection criteria.*

## 2.5 Cerenkov light detector: DIRC

The particle identification system is crucial for *BaBar* since the $CP$ violation analysis requires the ability to fully reconstruct one of the $B$ meson and to tag the flavor of the other $B$ decay: the momenta of the kaons used for flavor tagging extend up to about 2 GeV/$c$ with most of them below 1 GeV/$c$. On the other hand, pions and kaons from the rare two-body decays $B^0 \to \pi^+\pi^-$ and $B^0 \to K^+\pi^-$ must be well separated: they have momenta between 1.7 and 4.2 GeV/$c$ with a strong momentum-polar angle correlation of the tracks (higher momenta occur at more forward angles because of the c.m. system boost). So the particle identification system should be:

- thin and uniform in term of radiation lengths to minimize degradation of the calorimeter energy resolution
- small in the radial dimension to reduce the volume (cost) of the calorimeter

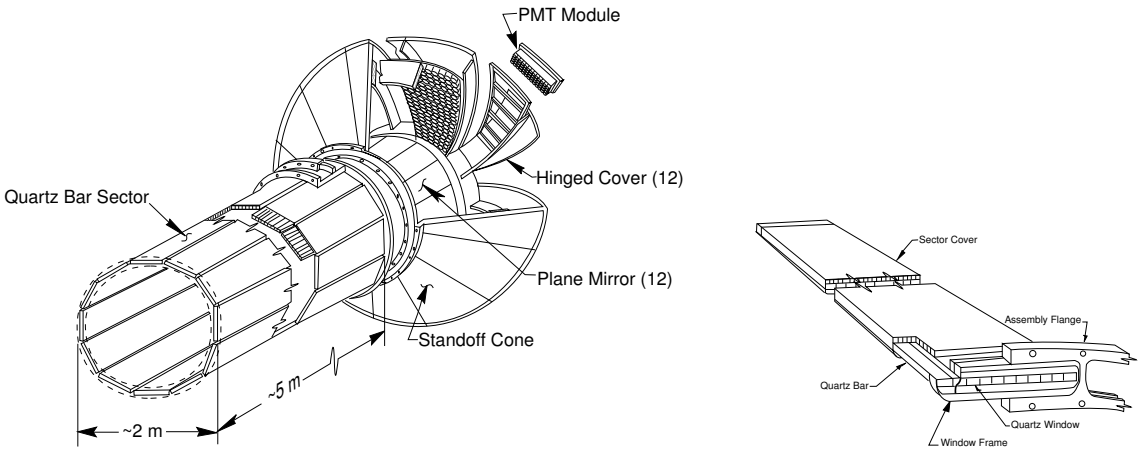


Figure 2.10: *Mechanical elements of the DIRC and schematic view of bars assembled into a mechanical and optical sector.*

- with fast signal response
- able to tolerate high background

DIRC stands for Detection of Internally Reflected Cerenkov light and it refers to a new kind of ring-imaging Cerenkov detector which meets the above requirements. The particle identification in the DIRC is based on the Cerenkov radiation produced by charged particles crossing a material with a speed higher than light speed in that material. The angular opening of the Cerenkov radiation cone depends on the particle speed:

$$\cos\theta_c = \frac{1}{n\beta} \tag{2.2}$$

where $\theta_c$ is the Cerenkov cone opening angle, $n$ is the refractive index of the material and $\beta$ is the particle velocity over $c$. The principle of the detection is based on the fact that the magnitudes of angles are maintained upon reflection from a flat surface.

Since particles are produced mainly forward in the detector because of the boost, the DIRC photon detector is placed at the backward end: the principal components of the DIRC are shown in Fig. 2.10. The DIRC is placed in the barrel region and consists of 144 long, straight bars arranged in a 12-sided polygonal barrel. The bars are $1.7\,cm$-thick, $3.5\,cm$-wide and $4.90\,m$-long: they are placed into 12 hermetically sealed containers, called *bar boxes*, made of very thin aluminum-hexcel panels. Within a single bar box, 12 bars are optically isolated by a $\sim 150\,\mu m$ air gap enforced by custom shims made from aluminum foil.

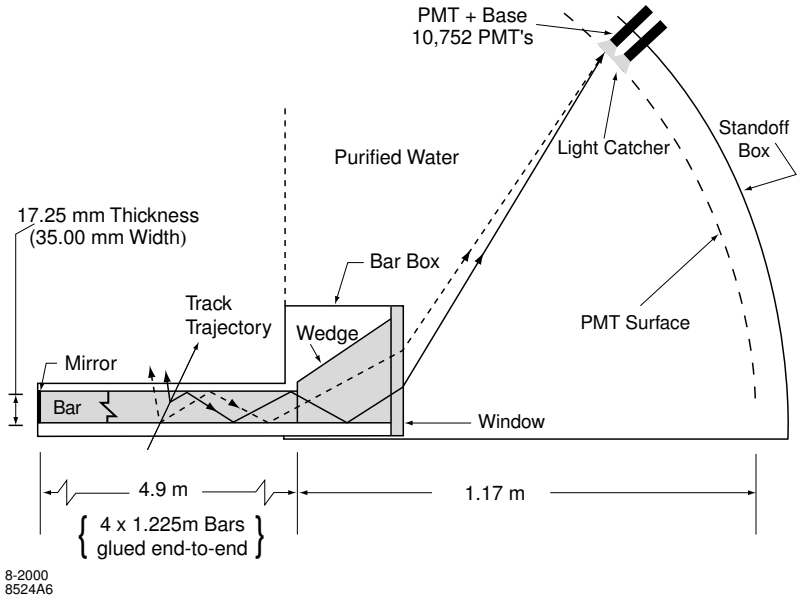


Figure 2.11: *Schematics of the DIRC fused silica radiator bar and imaging region. Not shown is a 6 mrad angle on the bottom surface of the wedge.*

The radiator material used for the bars is synthetic fused silica: the bars serve both as radiators and as light pipes for the portion of the light trapped in the radiator by total internal reflection. Synthetic silica has been chosen because of its resistance to ionizing radiation, its long attenuation length, its large index of refraction, its low chromatic dispersion within its wavelength acceptance.

The Cerenkov radiation is produced within these bars and is brought, through successive total internal reflections, in the backward direction outside the tracking and magnetic volumes: only the backward end of the bars is instrumented. A mirror placed at the other end on each bar reflects forward-going photons to the instrumented end. The Cerenkov angle at which a photon was produced is preserved in the propagation, modulo some discrete ambiguities (the forward-backward ambiguity can be resolved by the photon arrival-time measurement, for example). The DIRC efficiency grows together with the particle incidence angle because more light is produced and a larger fraction of this light is totally reflected. To maximize the total reflection, the material must have a refractive index (fused silica index is $n = 1.473$) higher than the surrounding environment (the DIRC is surrounded by air with index $n = 1.0002$).

Once photons arrive at the instrumented end, most of them emerge into a water-filled expansion region (see Fig. 2.11), called the *Standoff Box*: the purified water, whose

refractive index matches reasonably well that of the bars ($n_{H_2O} = 1.346$), is used to minimize the total internal reflection at the bar-water interface.

The standoff box is made of stainless steel and consists of a cone, cylinder and 12 sectors of PMTs: it contains about 6000 liters of purified water. Each of the 12 PMTs sectors contains 896 PMTs in a close-packed array inside the water volume: the PMTs are linear focused 2.9 $cm$ diameter photo-multiplier tubes, lying on an approximately toroidal surface.

The DIRC occupies only 8 $cm$ of radial space, which allows for a relatively large radius for the drift chamber while keeping the volume of the CsI Calorimeter reasonably low: it corresponds to about 17% $X_0$ at normal incidence. The angular coverage is the 94% of the $\phi$ azimuthal angle and the 83% of $\cos\theta_{CM}$.

Cerenkov photons are detected in the visible and near-UV range by the PMT array. A small piece of fused silica with a trapezoidal profile glued at the back end of each bar allows for significant reduction in the area requiring instrumentation because it folds one half of the image onto the other half. The PMTs are operated directly in water and are equipped with light concentrators: the photo-multiplier tubes are about 1.2 $m$ away from the end of the bars. This distance from the bar end to the PMTs, together with the size of the bars and PMTs, gives a geometric contribution to the single photon Cerenkov angle resolution of about 7 $mrad$. This is a bit larger than the resolution contribution from Cerenkov light production (mostly a 5.4 $mrad$ chromatic term) and transmission dispersions. The overall single photon resolution expected is about 9 $mrad$.

The image from the Cerenkov photons on the sensitive part of the detector is a cone cross-section whose opening angle is the Cerenkov angle modulo the refraction effects on the fused silica-water surface. In the most general case, the image consists of two cone cross-sections out of phase one from the other by a value related to an angle which is twice the particle incidence angle. In order to associate the photon signals with a track traversing a bar, the vector pointing from the center of the bar end to the center of each PMT is taken as a measure of the photon propagation angles $\alpha_x$, $\alpha_y$ and $\alpha_z$. Since the track position and angles are known from the tracking system, the three $\alpha$ angles can be used to determine the two Cerenkov angles $\theta_C$ and $\phi_C$. In addition, the arrival time of the signal provides an independent measurement of the propagation of the photon and can be related to the propagation angles $\alpha$. This over-constraint on the angles and the signal timing are useful in dealing with ambiguities in the signal association and high

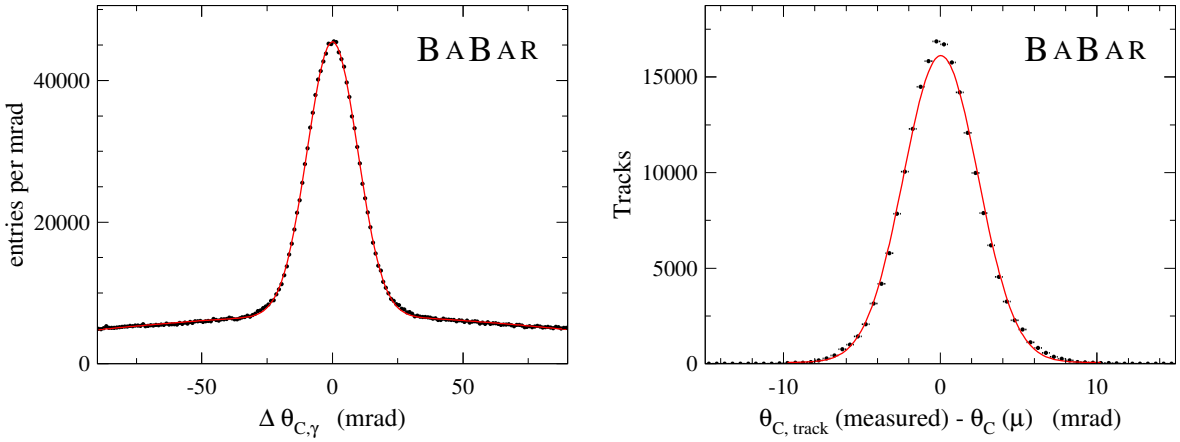


Figure 2.12: *From di-muon data events,* **left plot:** *single photon Cerenkov angle resolution. The distribution is fitted with a double-Gaussian and the width of the narrow Gaussian is* 9.6 *mrad.* **Right plot:** *reconstructed Cerenkov angle for single muons. The difference between the measured and expected Cerenkov angle is plotted and the curve represents a Gaussian distribution fit to the data with a width of* 2.4 *mrad.*

background rates.

The expected number of photo-electrons ($N_{pe}$) is $\sim$ 28 for a $\beta = 1$ particle entering normal to the surface at the center of a bar and increases by over a factor of two in the forward and backward directions.

The time distribution of real Cerenkov photons from a single event is of the order of 50 $ns$ wide and during normal data taking they are accompanied by hundreds of random photons in a flat background distribution within the trigger acceptance window. The Cerenkov angle has to be determined in an ambiguity that can be up to 16-fold: the goal of the reconstruction program is to associate the correct track with the candidate PMT signal with the requirement that the transit time of the photon from its creation in the bar to its detection at the PMT be consistent with the measurement error of about 1.5 $ns$.

### 2.5.1 Particles identification

An unbinned maximum likelihood formalism is used to take into account all information provided by the DIRC: the reconstruction routine provides a likelihood value for each of the five stable particle types ($e$, $\mu$, $\pi$, $K$ and $p$) if the track passes through the active volume of the DIRC. These likelihood probabilities are calculated in an iterative process by maximizing the likelihood value for the entire event while testing different hypotheses

for each track. If enough photons are found, a fit of $\theta_C$ and the number of observed signal and background photons are calculated. For Kaon identification different criteria (called $VeryLoose$, $Loose$, $Tight$, $VeryTight$ ) are established, each one corresponding to different efficiency and different pion misidentification probability.

In the absence of correlated systematic errors, the resolution ($\sigma_{C,\mathrm{track}}$) on the track Cerenkov angle should scale as

$$\sigma_{C,\mathrm{track}} = \frac{\sigma_{C,\gamma}}{\sqrt{N_{pe}}} \tag{2.3}$$

where $\sigma_{C,\gamma}$ is the single photon angle resolution. This angular resolution (obtained from di-muon events) can be estimated to be about 10.2 $mrad$, in good agreement with the expected value (see left plot in Fig. 2.12). The measured time resolution is 1.7 $ns$ close to the intrinsic 1.5 $ns$ time spread of the PMTs. In di-muon event data, the number of photo-electrons varies between 20 for small polar angles at the center of the barrel and 65 at large polar angles: this variation is well reproduced by Monte Carlo and can be understood by the fact that the number of Cerenkov photons varies with the path length of the track in the radiator (smaller path length at perpendicular incidence at the center of the barrel). Also the fraction of photons trapped by total internal reflection rises with larger values of $|\cos(\theta_{\mathrm{track}})|$. This increase in the number of photons for forward going tracks corresponds also to an increase in momentum of the tracks and thus an improvement of the DIRC performance.

The width of the track Cerenkov angle resolution for di-muon events is 2.4 $mrad$ compared to the design goal of 2.2 $mrad$ (see right plot in Fig. 2.12). From the measured single track resolution versus momentum in di-muon events and from the difference between the expected Cerenkov angles of charged pions and kaons, the pion-kaon separation power of the DIRC can be evaluated: the expected separation between pions and kaons at 3 GeV/$c$ is about 4.2$\sigma$, within 15% of the design goal.

The charged kaon efficiency is compared to the charged pion misidentification in Fig. 2.13. In the reconstruction of the invariant mass of the hadronic system, given the difference in the kaon momentum spectrum, Fig. 2.13, a charged track is identified as kaon if $p_K > 300$ MeV/$c$.

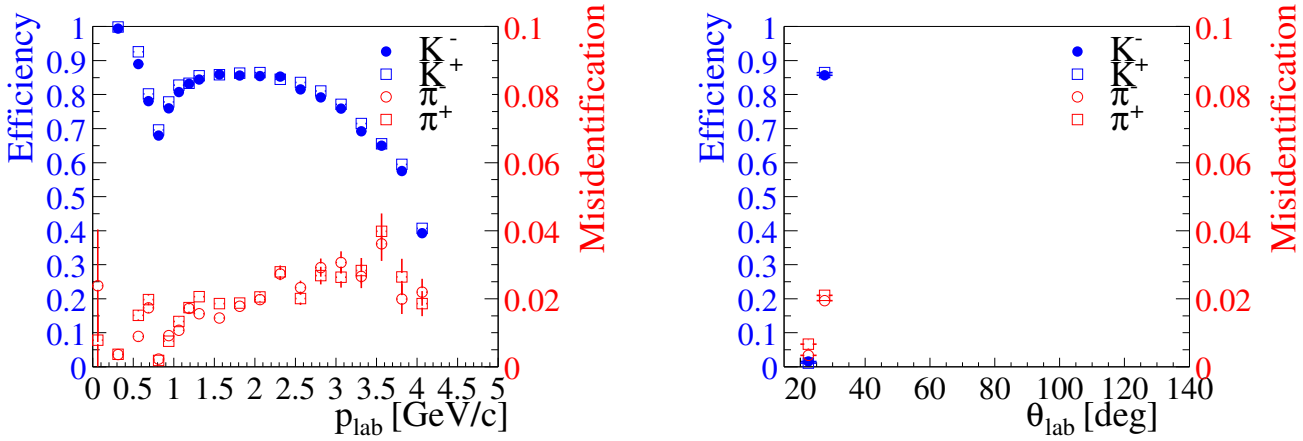


Figure 2.13: *Charged kaon identification and pion misidentification probability for the tight kaon micro selector as a function of momentum (left) and polar angle (right). The solid markers indicate the efficiency for positive particles, the empty markers the efficiency for negative particles. Note the different scales for identification and misidentification on the left and right ordinates, respectively.*

## 2.6 Electromagnetic calorimeter: EMC

The understanding of $CP$ violation in the $B$ meson system requires the reconstruction of final state containing a direct $\pi^0$ or that can be reconstructed through a decay chain containing one or more daughter $\pi^0$s. The electromagnetic calorimeter is designed to measure electromagnetic showers with excellent efficiency and energy and angular resolution over the energy range from 20 MeV to 9 GeV. This capability should allow the detection of photons from $\pi^0$ and $\eta$ decays as well as from electromagnetic and radiative processes. By identifying electrons, the EMC contributes to the flavor tagging of neutral $B$ mesons via semi-leptonic decays. The upper bound of the energy range is given by the need to measure QED processes like $e^+e^- \to e^+e^-(\gamma)$ and $e^+e^- \to \gamma\gamma$ for calibration and luminosity determination. The lower bound is set by the need for highly efficient reconstruction of $B$-meson decays containing multiple $\pi^0$s and $\eta^0$s. The measurement of very rare decays containing $\pi^0$s in the final state (for example, $B^0 \to \pi^0\pi^0$) puts the most stringent requirements on energy resolution, expected to be of the order of $1-2\%$. Below 2 GeV energy, the $\pi^0$ mass resolution is dominated by the energy resolution, while at higher energies, the angular resolution becomes dominant and it is required to be of the order of few *mrad*. The EMC is also used for electron identification and for completing the IFR output on $\mu$ and $K^0_L$ identification. It also has to operate in a $1.5\,T$ magnetic

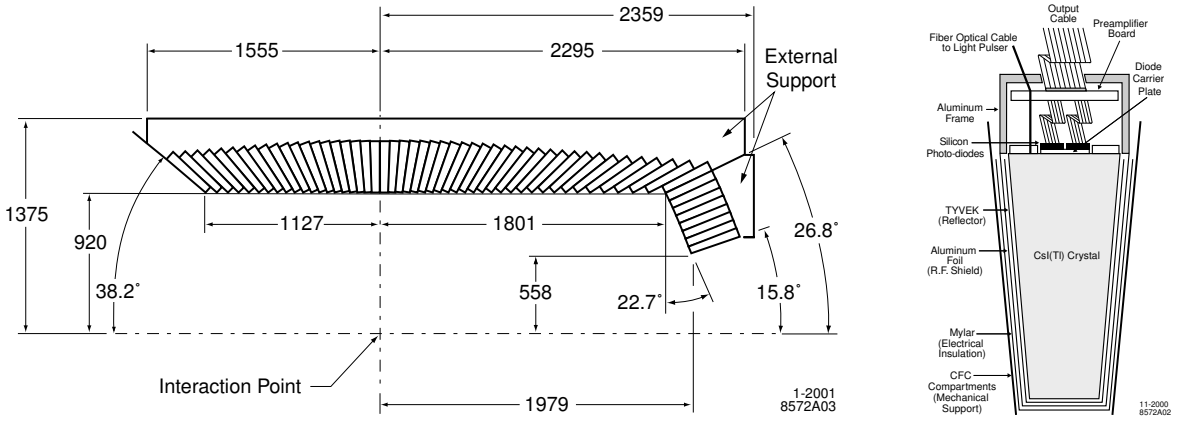


Figure 2.14: *The electromagnetic calorimeter layout in a longitudinal cross section and a schematic view of the wrapped CsI(Tl) crystal with the front-end readout package mounted on the rear face (not to scale).*

field.

The EMC has been chosen to be composed of a finely segmented array of thallium-doped cesium iodide (CsI(Tl)) crystals. The crystals are read out with silicon photo-diodes that are matched to the spectrum of scintillation light. The energy resolution of a homogeneous crystal calorimeter can be described empirically in terms of a sum of two terms added in quadrature:

$$\frac{\sigma_E}{E} = \frac{a}{\sqrt[4]{E(GeV)}} \oplus b \tag{2.4}$$

where $E$ and $\sigma_E$ refer to the energy of a photon and its rms error, measured in GeV. The energy dependent term $a(\sim 2\%)$ arises basically from the fluctuations in photon statistics, but also from the electronic noise of the photon detector and electronics and from the beam-generated background that leads to large numbers of additional photons. This first term dominates at low energy, while the constant term $b(\sim 1.8\%)$ is dominant at higher energies ($> 1$ GeV). It derives from non-uniformity in light collection, leakage or absorption in the material in front of the crystals and uncertainties in the calibration.

The angular resolution is determined by the transverse crystal size and the distance from the interaction point: it can be empirically parameterized as a sum of an energy dependent and a constant term

$$\sigma_\theta = \sigma_\phi = \frac{c}{\sqrt{E(GeV)}} + d \tag{2.5}$$

where $E$ is measured in GeV and with $c \sim 4\ mrad$ and $d \sim 0\ mrad$.

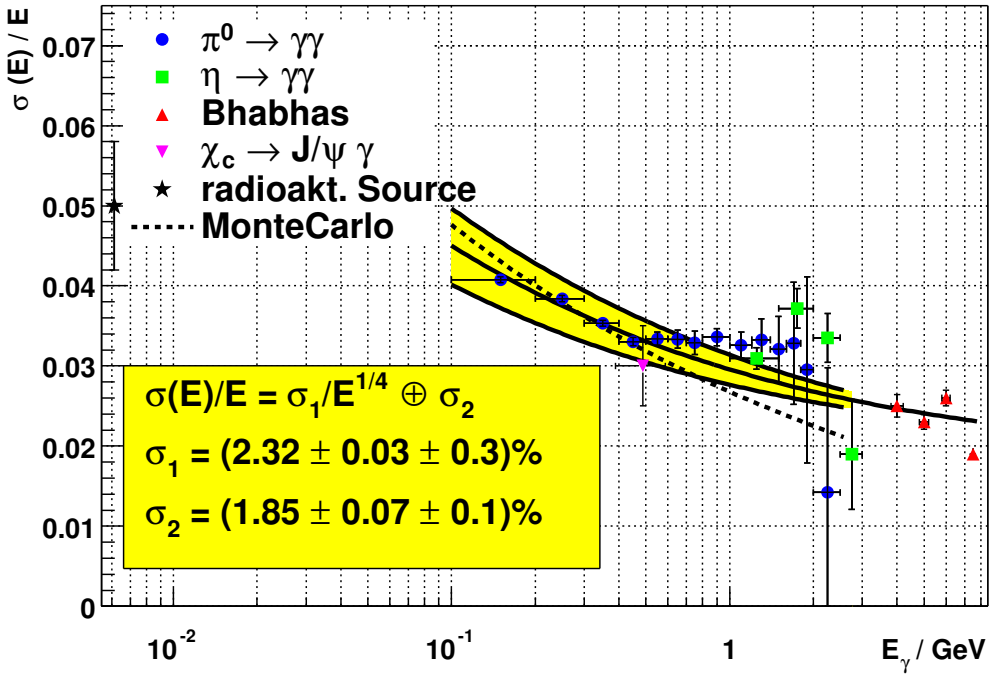


Figure 2.15: *EMC resolution as a function of the energy.*

In CsI(Tl), the intrinsic efficiency for the detection of photons is close to 100% down to a few MeV, but the minimum measurable energy in colliding beam data is about 20 MeV for the EMC: this limit is determined by beam and event-related background and the amount of material in front of the calorimeter. Because of the sensitivity of the $\pi^0$ efficiency to the minimum detectable photon energy, it is extremely important to keep the amount of material in front of the EMC to the lowest possible level.

Thallium-doped CsI has high light yield and small Molière radius in order to allow for excellent energy and angular resolution. It is also characterized by a short radiation length for shower containment at *BaBar* energies. The transverse size of the crystals is chosen to be comparable to the Molière radius achieving the required angular resolution at low energies while limiting the total number of crystals and readout channels.

The *BaBar* EMC (left plot in Fig. 2.14) consists of a cylindrical barrel and a conical forward end-cap: it has a full angle coverage in azimuth while in polar angle it extends from 15.8° to 141.8° corresponding to a solid angle coverage of 90% in the CM frame. Radially the barrel is located outside the particle ID system and within the magnet cryostat: the barrel has an inner radius of 92 *cm* and an outer radius of 137.5 *cm* and it's located asymmetrically about the interaction point, extending 112.7 *cm* in the backward direction and 180.1 *cm* in the forward direction. The barrel contains 5760 crystals arranged in 48

rings with 120 identical crystals each: the end-cap holds 820 crystals arranged in eight rings, adding up to a total of 6580 crystals. They are truncated-pyramid CsI(Tl) crystals (right plot in Fig. 2.14): they are tapered along their length with trapezoidal cross-sections with typical transverse dimensions of $4.7 \times 4.7\, cm^2$ at the front face, flaring out toward the back to about $6.1 \cdot 6.1\, cm^2$. All crystals in the backward half of the barrel have a length of $29.6\, cm$: toward the forward end of the barrel, crystal lengths increase up to $32.4\, cm$ in order to limit the effects of shower leakage from increasingly higher energy particles. All end-cap crystals are of $32.4\, cm$ length. The barrel and end-cap have total crystal volumes of $5.2\, m^3$ and $0.7\, m^3$, respectively. The CsI(Tl) scintillation light spectrum has a peak emission at $560\, nm$: two independent photodiodes collect this scintillation light from each crystal. The readout package consists of two silicon PIN diodes, closely coupled to the crystal and to two low-noise, charge-sensitive preamplifiers, all enclosed in a metallic housing.

A typical electromagnetic shower spreads over many adjacent crystals, forming a *cluster* of energy deposit: pattern recognition algorithms have been developed to identify these clusters and to discriminate single clusters with one energy maximum from merged clusters with more than one local energy maximum, referred to as *bumps*. The algorithms also determine whether a bump is generated by a charged or a neutral particle. Clusters are required to contain at least one seed crystal with an energy above 10 MeV: surrounding crystals are considered as part of the cluster if their energy exceeds a threshold of 1 MeV or if they are contiguous neighbors of a crystal with at least 3 MeV signal. The level of these thresholds depends on the current level of electronic noise and beam-generated background.

A bump is associated with a charged particle by projecting a track to the inner face of the calorimeter: the distance between the track impact point and the bump centroid is calculated and if it is consistent with the angle and momentum of the track, the bump is associated with this charged particle. Otherwise it is assumed to originate from a neutral particle.

On average, 15.8 clusters are detected per hadronic event: 10.2 are not associated to any charged particle. Currently, the beam-induced background contributes on average with 1.4 neutral clusters with energy above 20 MeV.

At low energy, the energy resolution of the EMC is measured directly with a 6.13 MeV radioactive photon source (a neutron-activated fluorocarbon fluid) yielding $\sigma_E/E =$

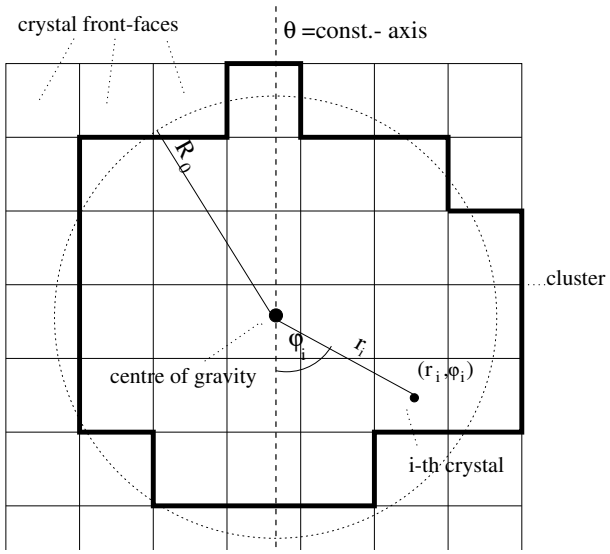


Figure 2.16: *Definition of the variables $r_i$, $\varphi_i$ and $R_0$*

$5.0 \pm 0.8\%$. At high energy, the resolution is derived from Bhabha scattering where the energy of the detected shower can be predicted from the polar angle of the electrons and positrons. The measured resolution is $\sigma_E/E = 1.9 \pm 0.1\%$ at 7.5 GeV. Fig. 2.15 shows the energy resolution on data compared with expectations from Monte Carlo. From a fit to the experimental results to eq. 2.4, $a = 2.32 \pm 0.30\%$ and $b = 1.85 \pm 0.12\%$ are obtained. The constant term comes out to be greater than expected: this is mainly caused by a cross talk effect, still not corrected, in the front-end electronics.

The measurement of the angular resolution is based on Bhabha events and ranges between 12 *mrad* and 3 *mrad* going from low to high energies. A fit to eq. 2.5 results in $c = (3.87 \pm 0.07)$ *mrad* and $d = (0.00 \pm 0.04)$ *mrad*.

### 2.6.1 Photon reconstruction

Neutral particles are selected as EMC local maxima energy depositions which are not matched to any track. These energy clusters originate mostly from photons, thus momenta and angles are assigned to be consistent with photons originating from the beam-beam interactions.

Bumps are required to be within the calorimeter acceptance of the detector: $0.410 < \theta < 2.54$ rad. A cut on the minimum energy $E_\gamma^{lab} > 30$ MeV of neutrals has been applied

to remove low energy photons associated with beam related backgrounds.

Additional backgrounds are due to hadronic interactions, either by $K_L$ or neutrons. These backgrounds can be fought by applying requests on the shape of the calorimeter clusters. In order to describe the lateral energy distributions of showers, the following variables are defined: $N$, the number of crystals associated with the shower, $E_i$, the energy deposited in the i-th crystal, numbering them such that $E_1 > E_2 > \ldots > E_N$, and $r_i, \varphi_i$, the polar coordinates in the plane perpendicular to the line pointing from the interaction point to the shower center centered in the cluster centroid (see Fig. 2.16). Using these variables, one can define the variable

$$LAT = \frac{\sum_{i=3}^{N} E_i r_i^2}{\sum_{i=3}^{N} E_i r_i^2 + E_1 r_0^2 + E_2 r_0^2}, \tag{2.6}$$

where $r_0$ is the average distance between two crystals, which is approximately $5\,cm$ for the *BaBar* calorimeter. This variable is constructed to discriminate between electromagnetic and hadronic showers based on their average properties. The sum starting from $i = 3$ omit the two crystals containing the highest amounts of energy. Electrons deposit most of their energy in two or three crystals, so that the value of LAT is small for electromagnetic showers. Multiplying the energies by the squared distances enhances the effect for hadronic showers, compared with electromagnetic ones. The request of $LAT < 0.8$ has been applied.

## 2.7 Instrumented Flux Return: IFR

IFR (*Instrumented Flux Return*) detector is dedicated to muon identification and neutral hadrons detection (mainly $K_L^0$) in a wide range of momentum and angles.

The IFR, as all the other *BaBar* subsystems, has an asymmetric structure with a polar angle coverage that is $17° \leq \theta_{lab} \leq 150°$. The IFR (Fig. 2.7) is made of 19 layers of Resistive Plate Chambers (RPC) in the barrel region and 18 layers in forward and backward regions, that are placed inside the iron layers used for the solenoidal magnetic field return joke. The iron structure is subdivided in three main parts: the barrel one surrounding the solenoid, made of 6 sextants covering the radial distance between 1.820 $m$ and 3.045 $m$ with a length of 3.750 $m$ (along the $z$ axis); the forward end-cap and backward end-cap covering the forward (positive $z$ axis) and backward regions. Moreover,

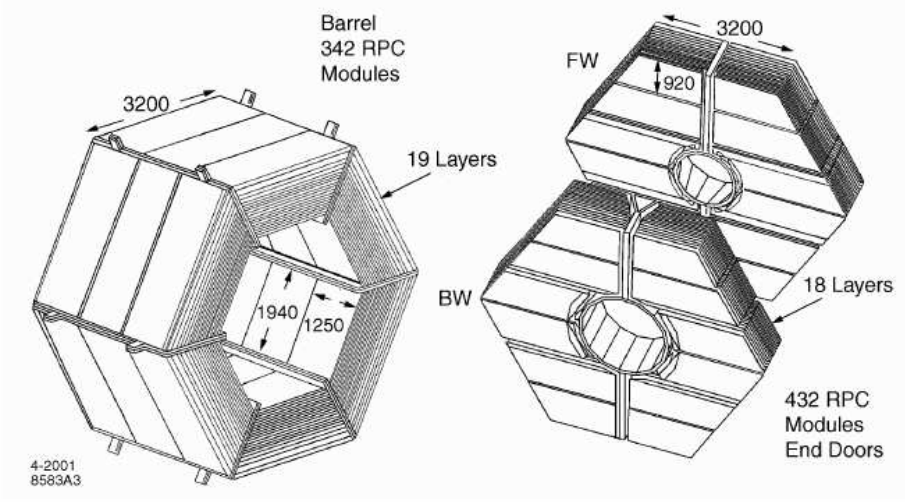


Figure 2.17: *IFR view*

| section | # di sectors | coor. | readout # layer | # strip layer/sector | strip len. (cm) | strip larg. (mm) | total # channel |
|---|---|---|---|---|---|---|---|
| barrel | 6 | $\phi$ | 19 | 96 | 350 | 19.7-32.8 | $\approx$ 11k |
| | | z | 19 | 96 | 190-318 | 38.5 | $\approx$ 11k |
| end-cap | 4 | y | 18 | 6x32 | 124-262 | 28.3 | 13,824 |
| | | x | 18 | 3x64 | 10-180 | 38.0 | $\approx$ 15k |
| cyl. | 4 | $\phi$ | 1 | 128 | 370 | 16.0 | 512 |
| | | z | 1 | 128 | 211 | 29.0 | 512 |
| | | u | 1 | 128 | 10-422 | 29.0 | 512 |
| | | v | 1 | 128 | 10-423 | 29.0 | 512 |

Table 2.5: *IFR readout segmentation. Total number of channels is* $\sim 53k$.

two cylindrical RPC layers have been installed between the calorimeter and the magnet cryostat in order to reveal particles exiting from the EMC. Those layers should cover the $\phi$ regions not covered by the barrel. Cylindrical layers are subdivided in four sections, each of them covering one fourth of the circumference: each of them has four RPC groups with orthogonal readout strips. $u - v$ helicoidal strips are placed inside along module's diagonals while $\phi$ and $z$ parallel strips are placed outside. The summary of IFR readout segmentation is given in Tab. 2.5.

Each end-cap has an hexagonal shape and is vertically subdivided in two halves in order to allow internal subsystems access, if necessary. Vacuum tube and PEP-II focusing

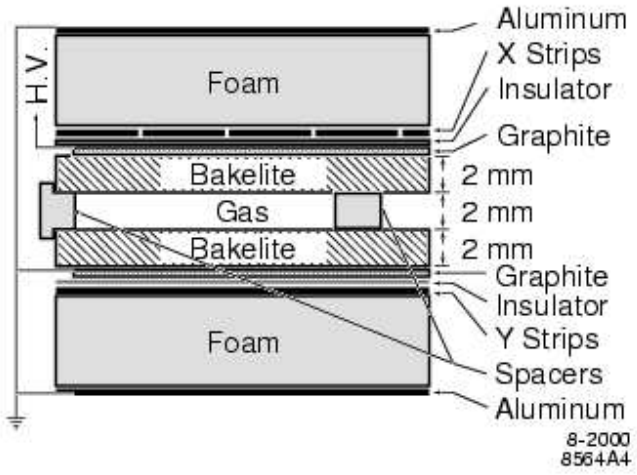


Figure 2.18: *Planar RPC section with HV connection scheme.*

elements are placed in the middle. Iron plates have a thickness ranging from 2 $cm$, for the inner ones placed nearest to the interaction region, to 10 $cm$ for the outer ones; this means a total thickness of steel at normal incidence of $\sim 65$ $cm$ (nearly corresponding to $\sim 4$ interaction lengths) in the barrel and $\sim 60$ $cm$ in the end-caps. Nominal distance between iron layers in the inner barrel region is 3.5 $cm$ while is 3.2 $cm$ everywhere else. The increased granularity of inner layers with respect to the outer ones is due to the fact that the largest part of particles detected inside the IFR are interacting in the very first material layers. Chosen segmentation is also the result of a compromise between the subsystem cost (proportional to the volume) and the need of a good efficiency for low momentum ($> 700$ MeV/$c$) muon detection, minimizing, at the same time, fraction of $K_L^0$'s that are not interacting inside the IFR. Result of this optimization is a not uniform segmentation with iron plates that have thickness increasing with distance from beam line. RPC section is shown in Fig. 2.18.

In each barrel sextant layers are kept together by a structure that reduces the coverage of solid angle with active detectors of $\sim 7\%$. Active coverage of IFR detector is $\approx 2000\ m^2$, for a total RPC modules number that is $\sim 900$. Signals produced by particles crossing the gas gap inside the RPCs are collected on both sides of the chamber by using thin strips (thickness $\sim 40\ \mu m$) with width of the order of a centimeter. Strips are applied in two orthogonal directions on insulating planes 200 $\mu m$ thick, in order to have a bi-dimensional view. In each barrel sextant each gap is hosting a chamber. This consist of a set of 3

RPC modules of rectangular shape. Each module is $\sim 125$ *cm* long along beams direction with variable width in order to completely fill the gap. Each chamber is equipped with 96 $\phi - strip$ placed along $z$ axis that are measuring the $\phi$ angle inside the barrel and 96 $z - strip$ orthogonal to beams direction that are measuring $z$ coordinate. $z - strips$ are subdivided into 3 panels of 32 strips with largeness, function of chamber radial position, ranging between 1.78 and 3.37 *cm*. This projective geometry allows a constant number of strips for all the various layers without decreasing detector resolution (each strip covers the same azimuthal angle). The used gas mixture is made of 56.7% Argon, 38.8% Freon-134a and 4.5% Isobutane. Working voltage for RPCs is $\sim 7.5\ kV$. Iron layers keeping apart RPC planes are chilled by a water system that keeps the temperature $\sim 20^oC$.

RPC efficiencies have been measured by using cosmics taken on a weekly base. Mean efficiency during 2000 run has been $\sim$ 78% for the barrel and $\sim$ 87% for the forward end-cap, less than that one measured in June 1999 ($\sim$ 92%). During the Summer 1999 the ambient temperature increased very much reaching about 32° to 38° inside the iron. During such period the IFR had problems to run the full detector because the dark current drawn by the chambers exceeded the total current limit provided by the power supply. All the chambers drawing more than $200\mu A$ were disconnected. In October the chambers were re-connected but they didn't recover the full efficiency. The forward end-cap has been completely reconstructed and installed in the Summer 2002: 5 intermediate RPC layers were replaced by 2.54 *cm* of brass, 10 *cm* of steel were added after the last RPC layer, an RPC (layer 19) was added in front of the forward end-cap, an RPC belt was added in the barrel–end-cap overlap region. Barrel efficiencies are still decreasing and are at $\sim$ 40% level while in the new forward end-cap, they are greater than 90%.

Muons are identified by measuring the number of traversed interaction lengths in the entire detector and comparing it with the number of expected interaction lengths for a muon of a given momentum. Moreover, the projected intersections of a track with the RPC planes are computed and, for each readout plane, all strips clusters detected within a predefined distance from the predicted intersection are associated with the track: the average number and the r.m.s. of the distribution of RPC strips per layer gives additional $\mu/\pi$ discriminating power. It is expected in fact the average number of strips per layer to be larger for pions producing an hadronic interaction than for muons. Other variables exploiting clusters distribution shapes are constructed. Selection criteria based on all these variables are applied to select muons. The performance of the muon selection has

been tested on samples of kinematically identified muons from $\mu\mu ee$ and $\mu\mu\gamma$ final states and pions from three-prong $\tau$ decays and $K_S \to \pi^+\pi^-$ decays.

At the end of the summer 2004 RPC from Top and Bottom Barrel sextant have been substituted with limited streamer tube (LST). Data recording **Run-5** has been started only in the second half of April 2005 so there aren't still enough data to have a complete evaluation of the LST efficiency and performance.

The efficiency of the LST is monitored daily using $\mu\mu$ pairs from colliding beams and monthly from cosmic rays. The calculated efficiency results to be constant around 90%. The geometric efficiency is 92.5%. The fluctuation of the efficiency are mostly related to the fluctuation on the number of silent channels, but no loss of efficiency for each single LST is detected.

For the $\pi/\mu$ discrimination the LST appear to work better than RPC ever did.

# Chapter 3

# $D^0 \to K_S\pi^-\pi^+$ Dalitz amplitude parameterization

The dynamics of charmed-meson decays have been studied extensively during the past decade. Dalitz-plot analysis of three body $D$ decays have proven to be a powerful tool to investigate the effects of the resonance structure, interference pattern, and final-state interaction. Moreover, the Dalitz-amplitude parameterization of the $D^0 \to K_S\pi^-\pi^+$ decay is essential for the measurement of the angle $\gamma$ of the Unitarity triangle [22]. In this context, a Dalitz analysis of the $D^0 \to K_S\pi^-\pi^+$ decay has been performed. The Dalitz amplitude is parameterized as a sum of relativistic Breit-Wigner resonances (referred to as the "Breit-Wigner" model for the rest), including form factors and a term describing the angular distribution of the two body decay of each intermediate state.

Given the low statistics of the current data sample, the Breit-Wigner model proved sufficient for the measurement of $\gamma$. However, this parameterization gives a large systematic uncertainty to the measurement of $\gamma$ (see Sec. 5.3.7) and in general cannot give a satisfactory parameterization of the $D^0 \to K_S\pi^-\pi^+$ amplitude since it works well only in the case of narrow, isolated resonances. In fact, resonances are associated generally with the poles of the $S$ matrix in the complex energy plane, and the Breit-Wigner amplitude corresponds to only the most elementary type of the possible extrapolations from the physical region to an unphysical sheet pole. In the case of broad resonances that overlap significantly, a more complex formalism is required. This is particularly true for the S-wave component of the $D^0 \to K_S\pi^-\pi^+$ decay.

The $K$-matrix formalism is an approach ideally suited to the study of overlapping resonances in multichannel decays. Although this approach was developed specifically in the context of two body scattering, it can be generalized to the case of resonance

production in multi-body decays when the two body system in the final state is isolated, and the two particles do not interact simultaneously with the rest of the final state in the production process (isobar model). In addition, the $K$-matrix formalism provides a direct way of imposing the two body Unitarity constraint that is not guaranteed in the case of the Breit-Wigner model.

This chapter presents the parameterization of the $D^0 \to K_S\pi^-\pi^+$ Dalitz amplitude [1] with the Breit-Wigner model and a model with the $K$-matrix formalism applied to the $\pi^+\pi^-$ S-Wave (referred to as the "$K$-matrix" model for the rest).

## 3.1 $D^0 \to K_S\pi^-\pi^+$ selection

### 3.1.1 The $D^0$ and $D^{*+}$ reconstruction

The $D^0 \to K_S\pi^-\pi^+$ data sample is reconstructed from continuum $e^+e^- \to c\bar{c}$ events through the following decay chain:

$$\begin{aligned} D^{*+} &\to D^0\pi^+ \\ D^0 &\to K_s\pi^-\pi^+ \ . \end{aligned} \tag{3.1}$$

Selecting the data from the continuum allows to have a high statistics data sample with a high purity while reconstructing the $D^0$ from the $D^{*+}$ decay gives the possibility to determine the flavor of the $D^0$ from the charge of the pion coming from the $D^{*+}$ (slow pion).

The neutral kaon is constructed from pairs of oppositely charged pions satisfying the requests described in Sec. 2.4 The $K_S$ mass is required to be in the region $(0.488 - 0.508)$ GeV/$c^2$ corresponding to nearly 3 standard deviations around the fitted mean value. Fig. 3.1 shows the distribution of the $K_S$ mass and the fit result. In order to remove fake $K_S$ candidates, the $K_S$ decay distance from the $D^0$ vertex is required to be greater than 0.4 cm. The direction of the $K_S$ can be evaluated from the momentum of the two pions ($dir_1$) as well as from the direction of the flight distance from the $K_S$ and the $D^0$ decay vertexes ($dir_2$). For a real candidate these two directions coincides. Defining $\alpha_{K_S} = (dir_1, dir_2)$, a cut on $\cos(\alpha_{K_S}) > 0.99$ is required. These cuts have the property of rejecting the fake $K_S$ and in particular helps in removing possible contamination from

[1] $\bar{D}^0 \to K_S\pi^-\pi^+$ is implicit for the rest. The $\bar{D}^0$ Dalitz amplitude is obtained from the $D^0$ one swapping the two variables $M^2(K_S\pi^-) \leftrightarrow M^2(K_S\pi^+)$. The data sample contains both $D^0$ and $\bar{D}^0$.

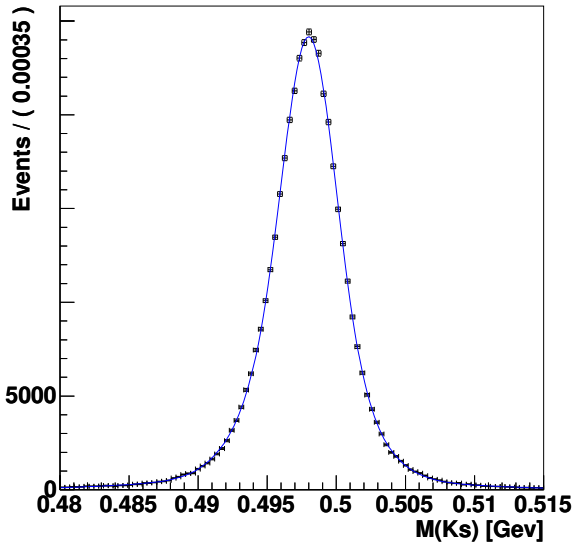


Figure 3.1: *Distribution of the $K_S$ mass and the fit result. The distribution is fitted with a sum of three Gaussian. The region $\pm 10$ MeV/$c^2$ around the fitted mean value is selected.*

decays of $D^0$ into four pions. In order to improve momentum resolution mass constraint is applied to the $K_S$ and the $D^0$.

The center-of-mass (CM) momentum of the $D^0$ candidate is required to be greater than 2.2 GeV/$c$ to remove $D^0$ coming from $B$ decays.

The $D^*$ candidate is reconstructed combining the $D^0$ candidate with pions with momentum below 0.6 GeV/$c$. Beam spot constraint is applied to the vertex fit.

### 3.1.2 Final selection

Since $D^{*+} \to D^0\pi^+$ and $D^{*-} \to \bar{D}^0\pi^-$, the charge of the slow pion tags the flavor of the neutral $D$ meson. For the selection of $D^0 \to K_S\pi^-\pi^+$ events the reconstructed $D^0$ mass $M_D$, and the mass difference $\Delta m = M_{D^*} - M_D$ are used, where $M_{D^*}$ is the reconstructed mass of the $D^0\pi$ combination. The $\Delta m$ distribution (Fig. 3.2) is fitted with a sum of two Gaussians for signal, and a threshold function

$$\Delta m_{\text{bkg}} = \left(1 - e^{\frac{-(\Delta m - \Delta m_0)}{c}}\right)\left(\frac{\Delta m}{\Delta m_0}\right)^a + b\left(\frac{\Delta m}{\Delta m_0} - 1\right) \tag{3.2}$$

for background. The region of $\pm 0.5$ MeV/$c^2$ ($\sim 2\sigma$) around the mean of the $\Delta m$ distribution is selected.

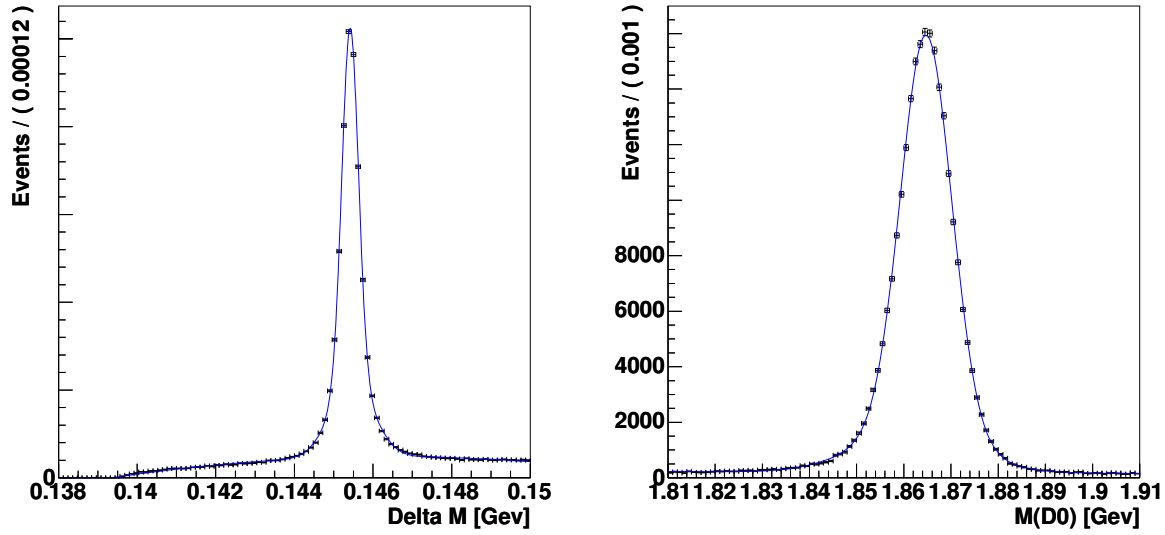


(a) $M(D^*) - M(D^0)$ (b) $M(K_s\pi^+\pi^-)_{D^0}$

Figure 3.2: *Distributions of* $\Delta m$ *and* $M(D^0)$ *(histograms), and the fit results (curves). The selected region is* $(144.93 - 195.93)$ $MeV/c^2$ *for* $\Delta m$ *and* $(1.8539 - 1.8755)$ $GeV/c^2$ *for* $M(D^0)$*. The* $M(D^0)$ *distribution is plotted in the selected* $\Delta m$ *region.*

The $M_D$ distribution is fitted with a sum of two Gaussians for signal and a first-order polynomial for the background. Fig. 3.2 shows the distribution of $D^0$ mass spectrum in the $\Delta M$ selected region and the result of the fit. The region of $2\sigma$ (10.8 MeV/$c^2$) around the mean value of $D^0$ mass distribution is selected. A sample of 215449 events is obtained. The purity of the data sample is estimated to be 98.1% from a $D^0$ mass fit where the signal component is parameterized with a sum of two Gaussians and the background component with a linear function. A detailed Monte Carlo study, described in Sec. 3.1.3 has confirmed the possibility to estimate the purity of the data sample from the $D^0$ mass fit. Fig. 3.3 shows the distribution of the Dalitz plot and projections on the three combinations of $m^2$ for the daughter particles.

### 3.1.3 Background Composition

In order to estimate the background composition, the selection criteria described in the previous section are applied to the $uds$, $c\bar{c}$, and $B\bar{B}$ generic Monte Carlo samples. The $M(D^0)$ distributions of the different Monte Carlo components and the Data-MC compar-

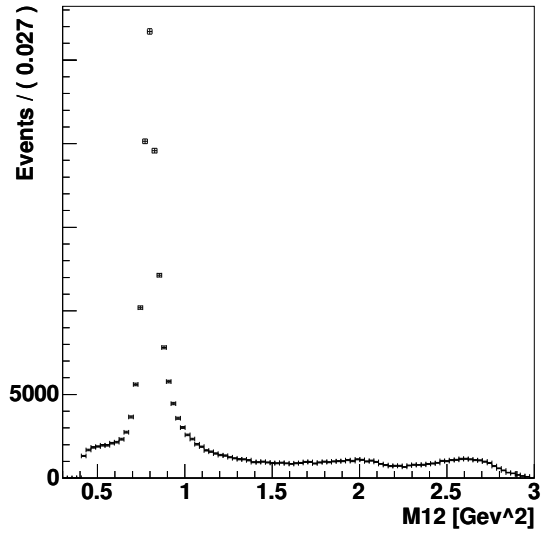


(a) $M^2_{K_S\pi^-}$

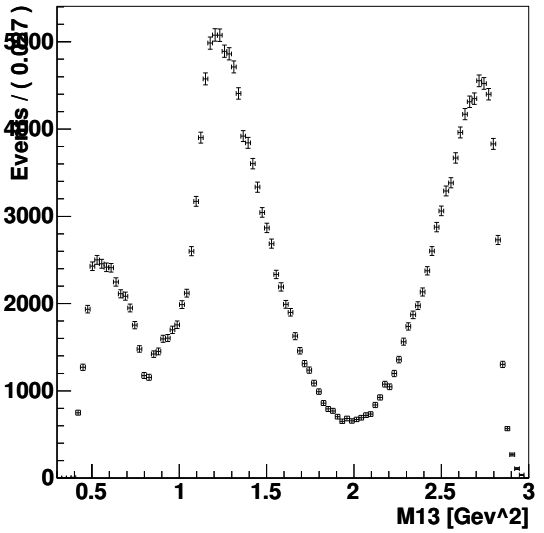


(b) $M^2_{K_S\pi^+}$

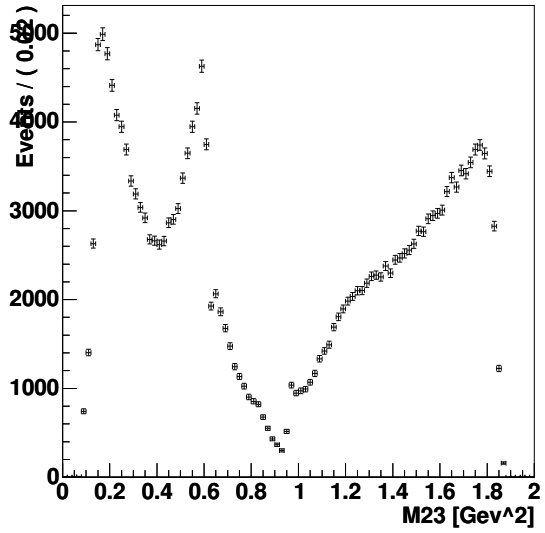


(c) $M^2_{pi^+\pi^-}$

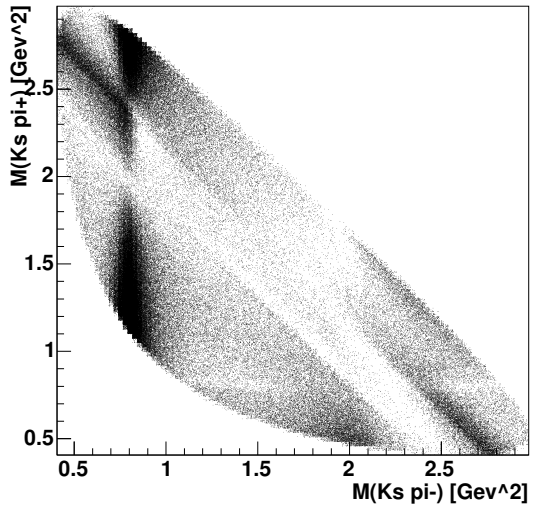


(d) Dalitz plot

Figure 3.3: *$D^0 \to K_S\pi^+\pi^-$ Dalitz plot projections, and the two-dimensional Dalitz plane. The data sample contains 215449 events with a purity of* 98.1%.

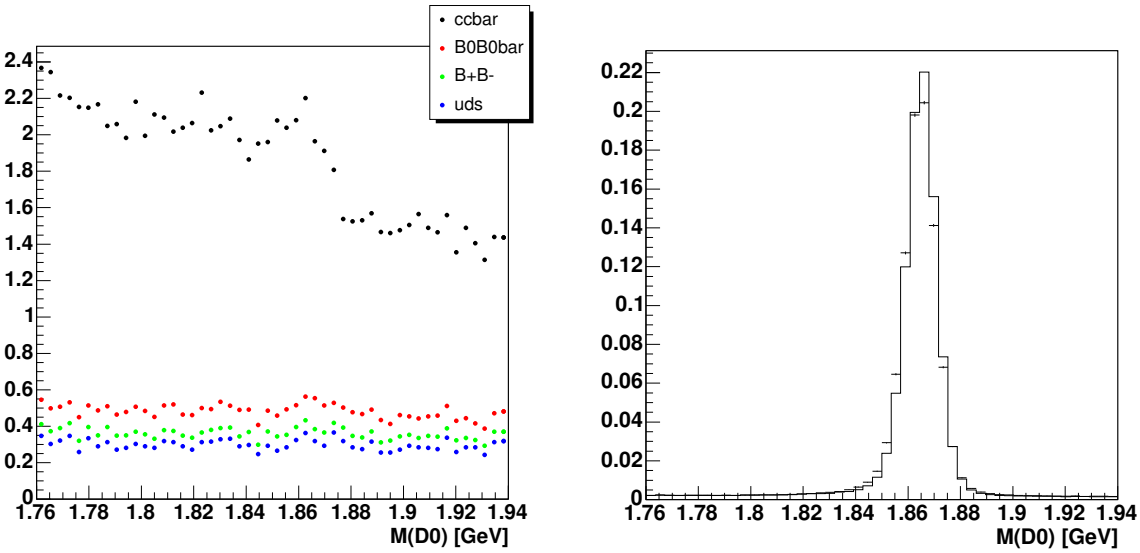


(a) $M(D^0)$ [GeV/$c^2$] MC background components

(b) $M(D^0)$ [GeV/$c^2$] Data-MC comparison: points=data, line=MC

Figure 3.4: *$M(D^0)$ distributions of the different Monte Carlo components and the Data-MC comparison. The small differences of the shapes of the two $M(D^0)$ distribution explains the small difference between the two purity values. The shapes of the background components don't present a peak in the $M(D^0)$ selected region.*

ison are shown in Fig. 3.4. The fraction of the wrong flavor $D^0$ is less than 0.1% and is neglected.

A Monte Carlo study gives a purity of 98.9 % very close to the one obtained with the $M(D^0)$ fit to the data sample then the value obtained from data is chosen. The small difference between the two values comes from the small difference of the two $D^0$ mass distribution shapes. Moreover the $M_D$ distributions of the background components don't present a peak in the selected region; the parameterization of the background distribution with a linear function represents then a good approximation.

### 3.1.4 Dalitz background parameterization

Since the $M(D^0)$ distributions of the background components don't present a peak in the selected signal region, the $M(D^0)$ sidebands can be used to parameterize the background Dalitz distribution. The $D^0$ mass constraint, in the sidebands regions, deforms the shape of the Dalitz distribution, in particular the value of the masses and the widths of the

resonances present in the background will be different from the real ones. To avoid this problem the $D^0$ mass constraint is removed for the Dalitz background parameterization. Two sidebands are chosen: the "left" sideband centered at $M(D^0) = 1.8$ GeV/$c^2$ and the "right" sideband centered at $M(D^0) = 1.92$ GeV/$c^2$. The width of both of them is chosen equal to 30 MeV/$c^2$; this value is small enough to avoid problems coming from the $D^0$ mass not constrained, and large enough to have a sufficient number of events to perform the Dalitz fit. The fraction of signal events in the sidebands is evaluated with a $D^0$ mass fit to the data sample.

The signal component is parameterized using the Breit-Wigner model described in detail in Sec. 3.2, The background component is parameterized with sum of two terms:

- Resonant component: since the background is a sum of many different components that don't interfere between them and there is not a dominant component, the Resonant component can be parameterized with an incoherent sum of Breit-Wigner functions. The resonances used are: $K^{*-}(892)$, $K^{*+}(892)$, $\rho^0(770)$ and a spin 0 $K_S\pi^+$ Breit-Wigner functions not corresponding to any real resonance but introduced to parameterize a sample of not well reconstructed events that give a Breit-Wigner shape in the Dalitz plot.

- Non resonant component: parameterized by a third-order polynomial in two dimensions.

The relative fraction of the two background components are evaluated from the data sample. In detail, the model of the background component is:

$$\begin{aligned} & f \cdot (|\rho^0(770)|^2 + c1 \cdot |K^{*-}(892)|^2 + c2 \cdot |K^{*+}(892)|^2 + c3 \cdot |BW(m_{13}, S=0)|^2) + \\ & (1-f) \cdot |1 + a1 \cdot m_{12} + a2 \cdot m_{13} + a3 \cdot m_{12}^2 + a4 \cdot m_{13}^2 + a5 \cdot m_{12} \cdot m_{13} + \\ & a6 \cdot m_{12}^3 + a7 \cdot m_{13}^3 + a8 \cdot m_{12} \cdot m_{13}^2 + a9 \cdot m_{13} \cdot m_{12}^2| \end{aligned} \tag{3.3}$$

where $BW$ represent the effective Breit-Wigner function, $S$ is the value of the spin, $m_{12}$, $m_{13}$ are the $K_S\pi^-$, $K_S\pi^+$ invariant masses respectively, and $f$ is the fraction of the resonant term.

Fig. 3.5 shows the left and right sideband data samples and the fits result. The mass and the width of the $K^{*-}(892)$, $K^{*+}(892)$, $\rho^0(770)$ are taken from the PDG [41], the mass and the width of the effective Breit-Wigner are extracted from the fit of the right sideband, where it is more visible, and fixed in the fit of the left sideband.

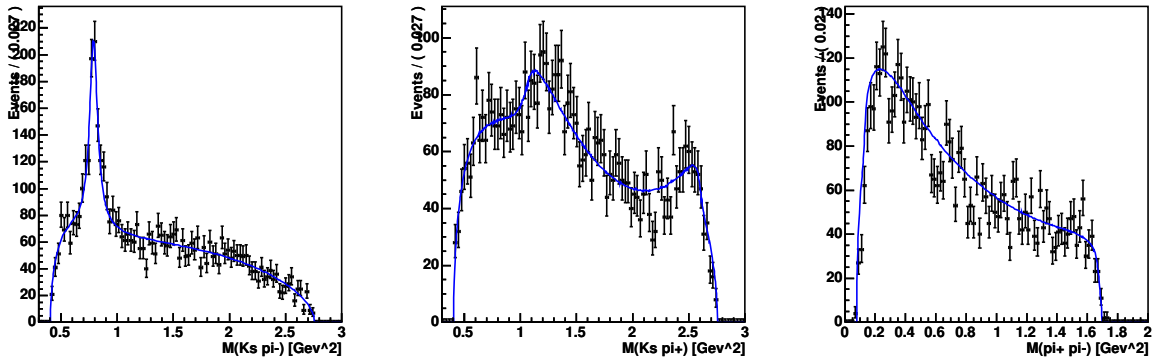


(a) $M^2_{K_S\pi^-}$, $M^2_{K_S\pi^+}$ and $M^2_{pi^+\pi^-}$ distribution of the left sideband

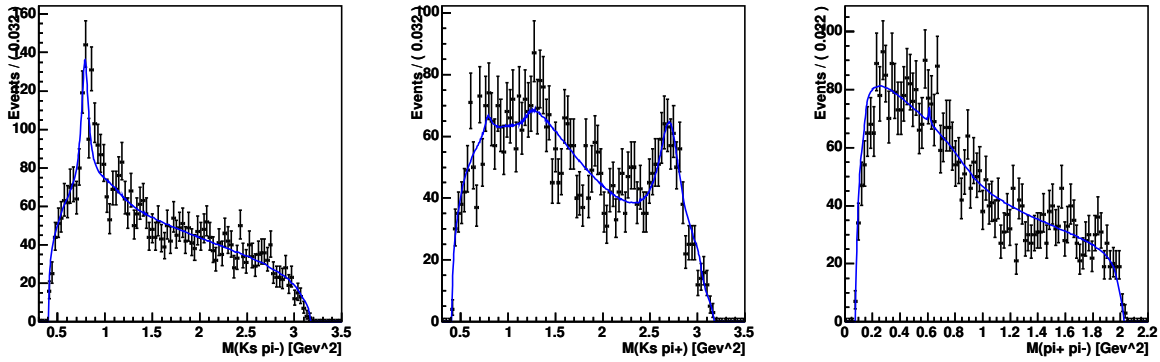


(b) $M^2_{K_S\pi^-}$, $M^2_{K_S\pi^+}$ and $M^2_{pi^+\pi^-}$ distribution of the right sideband

Figure 3.5: *Left and right sideband data samples and the fit results. The mass and the width of the* $K^{*-}(892)$, $K^{*+}(892)$, $\rho^0(770)$ *are taken from the PDG [41], the mass and the width of the effective Breit-Wigner are extracted from the fit of the right sideband, where it is more visible, and fixed in the fit of the left sideband.*

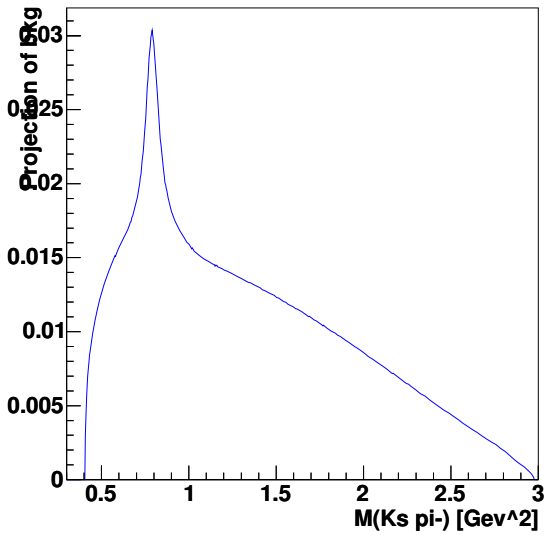


(a) $M^2_{K_S\pi^-}$

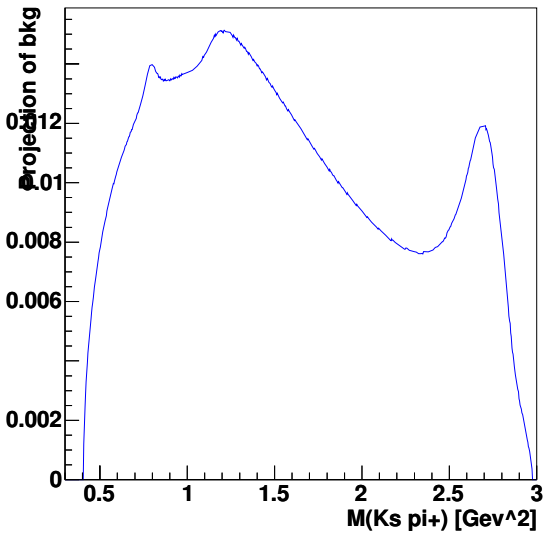


(b) $M^2_{K_S\pi^+}$

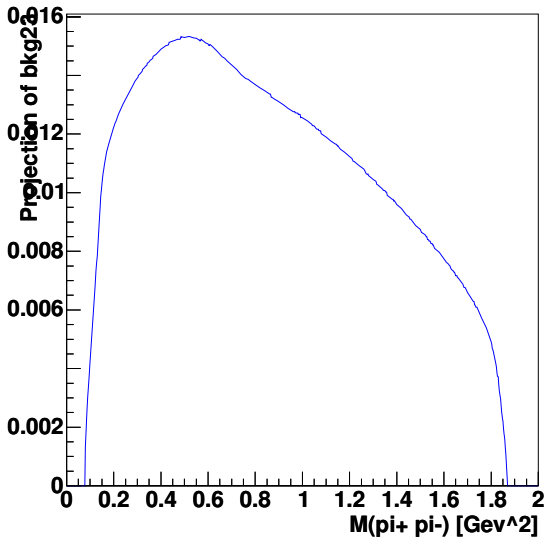


(c) $M^2_{pi^+\pi^-}$

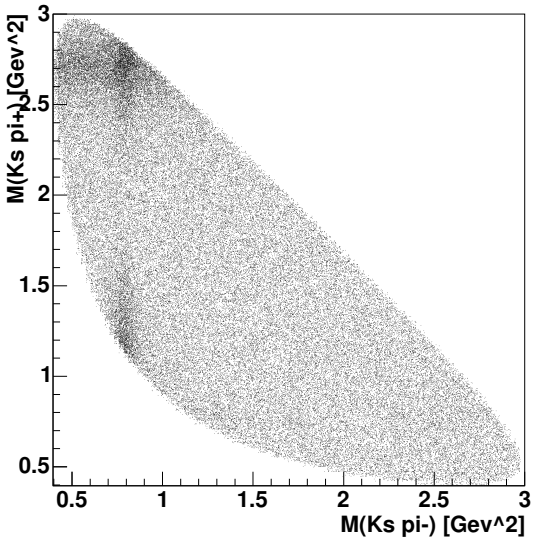


(d) Dalitz plot

Figure 3.6: *Background parameterization Dalitz plot projections, and the two-dimensional Dalitz plane.*

Fig. 3.6 shows the background parameterization Dalitz plot projections, and the two-dimensional Dalitz plane. The values of the coefficients of the resonant component and of the fraction $f$ are obtained with a linear interpolation of the values of the two sidebands. For the non resonant component, since the kinematically allowed region depends from the value of the $D^0$ mass, a more complicated technique must be used: two samples are generated according to the fit results of the two sidebands, a momentum rescaling is applied to the two samples in order to rescale them to the allowed Dalitz region, the rescaled samples are merged according to the number of events of the two data samples, then the merged sample is fitted with the third-order polynomial function.

### 3.1.5 Efficiency map

The Dalitz plot efficiency map is evaluated using a signal Monte Carlo sample of 2821000 events with the $D^0$ allowed to decay isotropically. The 334853 events remaining after all selection criteria are fitted to a third-order polynomial in two dimensions:

$$\epsilon(x,y) = |1 + a_1 \cdot x + a_2 \cdot y + a_3 \cdot x^2 + a_4 \cdot x^2 + a_5 \cdot x \cdot y + a_6 \cdot x^3 + a_7 \cdot y^3 + a_8 \cdot x \cdot y^2 + a_9 \cdot y \cdot x^2|, \tag{3.4}$$

where $x = m^2_{12}$ and $y = m^2_{13}$ are the squared $(K_s\pi^-)$ and $(K_s\pi^+)$ masses of the $D^0$ decay. Fig. 3.7 shows the Dalitz distribution of the Monte Carlo sample and the fit result. Fig. 3.8 shows the projections of signal Monte Carlo and a flat distribution is superimposed, the efficiency map is basically consistent with flat.

### 3.1.6 Resolution function

The imperfect momentum reconstruction of the tracks from the $D^0$ leads to a modification of the Dalitz structure. This effect worsens the agreement between the $D^0 \to K^0_S\pi^+\pi^-$ Dalitz plot distribution and the Dalitz model used to fit it, and causes about 2-3% of the reconstructed $D^0$ decays to lie outside the kinematically-allowed Dalitz region. In order to improve the $D^0$ daughters' momenta resolution, a $D^0$ mass constraint fit is applied during the reconstruction. There are two advantages: 1) the uncertainty of the four-momentum of the particles is reduced, giving a more precise measurement of the mass squared variables used to define an event position in the Dalitz plot, and 2) the decay position in these variables is guaranteed to respect the kinematic boundaries of the Dalitz plot.

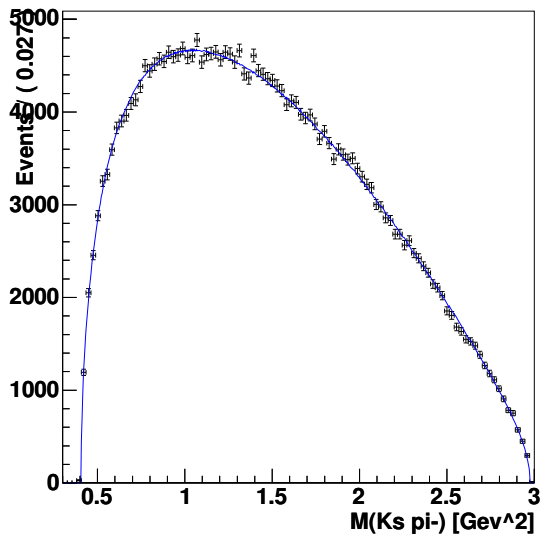


(a) $M^2_{K_S\pi^-}$

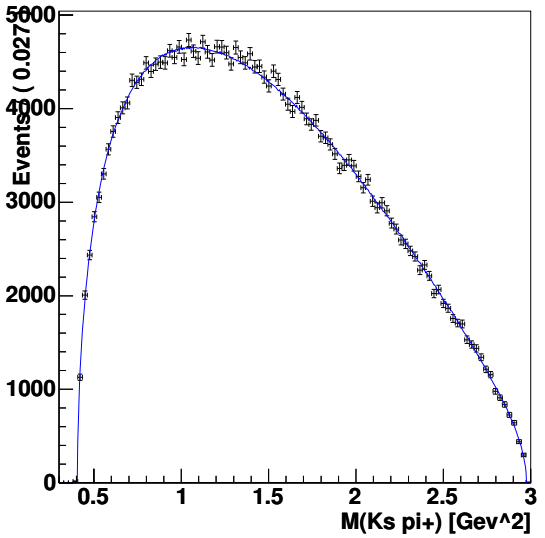


(b) $M^2_{K_S\pi^+}$

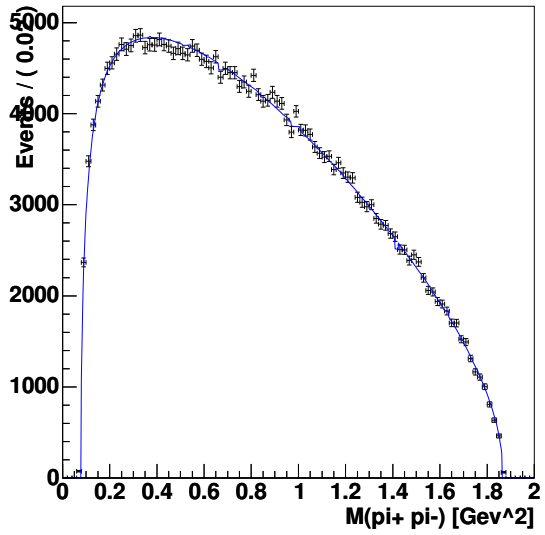


(c) $M^2_{pi^+\pi^-}$

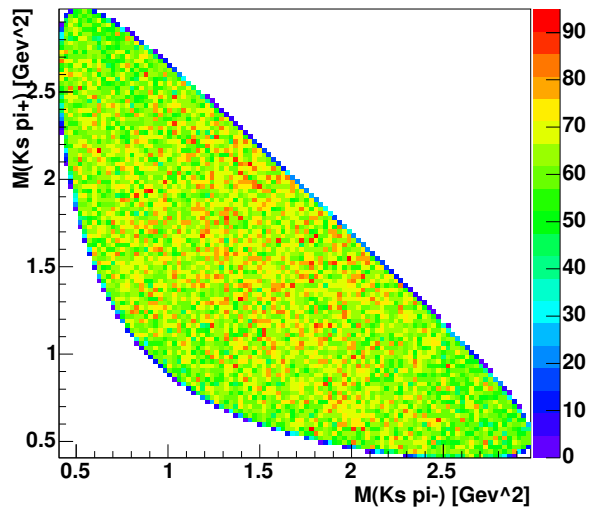


(d) Dalitz plot

Figure 3.7: *Projections of signal Monte Carlo and efficiency map.*

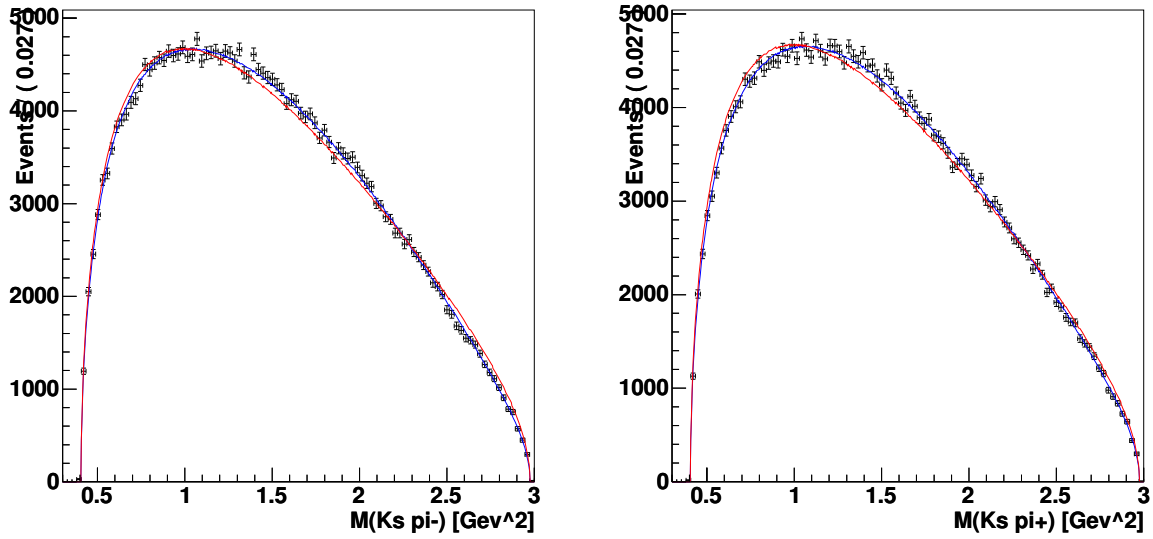


(a) $M^2_{K_S\pi^-}$ (b) $M^2_{K_S\pi^+}$

Figure 3.8: *Projections of signal Monte Carlo and the efficiency map (blue line). A flat distribution is superimposed (red line).*

Even after the mass constraint some resolution effects are present. To evaluate the effect of the of the resolution function on the shape of the Dalitz amplitude the event-by-event difference in the generated and reconstructed $(m_{12}, m_{13})$ distributions is calculated. Fig. 3.9 shows the distribution of the resolution function fitted with a sum of three Gaussians.

The resolution as a function of the Dalitz variables is obtained in bins of (0.1 GeV$^2\cdot$0.1 GeV$^2$) by fitting the resolution function for $(m_{12}, m_{13})$ with a sum of two Gaussians. Fig. 3.10 shows the value of the shift and the width in the $(m_{12}, m_{13})$. The width has a clear maximum in the region of the $K^*(892)$ (Cabibbo allowed and double Cabibbo suppressed).

In order to see the effect of the resolution function on the $K^*(892)$ shape a sample of $200k$ events is generated and the generated sample is smeared according to resolution function of the Dalitz plot. Then both the generated and the smeared samples are fitted. The $K^*(892)$ is chosen since it take up the region of the Dalitz plot where is maximum the resolution effect, moreover the $K^*(892)$, together with the $\rho^0(770)$, is the largest component of the Dalitz amplitude. The effect on the $\rho^0(770)$ is found not perceptible. In

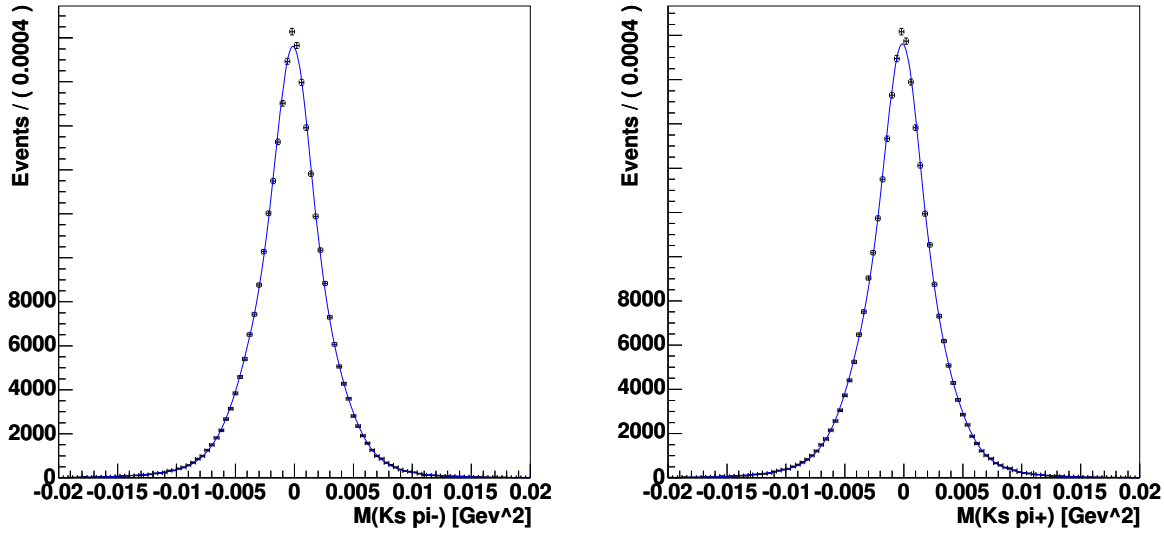


(a) $M^2_{K_S\pi^-}$ (b) $M^2_{K_S\pi^+}$

Figure 3.9: *Distribution of the resolution function.*

order to test the effect of the resolution function on a narrow resonance also the $\omega(782)$ is considered. The generated and the smeared samples of $K^*(892)$ and $\omega(782)$ are displayed in Figure 3.11.

Since the amplitude of the $\omega(782)$ is quite small, the very small effect on its width can be neglected. For $K^*(892)$ there is no perceptible effect.

## 3.2 Breit Wigner fit

The Breit Wigner fit is the first Dalitz fit performed in the context of the $\gamma$ analysis and it is still the Dalitz fit used for the extraction of $\gamma$ since the fit with the $K$-matrix model is still preliminary and lacks a complete evaluation of the systematics for all the components of the Dalitz amplitude. Even if it doesn't describe the case of broad resonances that overlap significantly, the Breit Wigner fit, given the low statistics of the current $B$ data sample, is proved sufficient for the measurement of $\gamma$ as it will be shown in Sec. 5.3.7. It is performed in a sub data sample of the one described in Sec. 3.1. This sample contains 81491 events with a purity of 97.64%. The efficiency map is parameterized using the same function described is Sec. 3.1; the background, instead, is parameterized with a flat

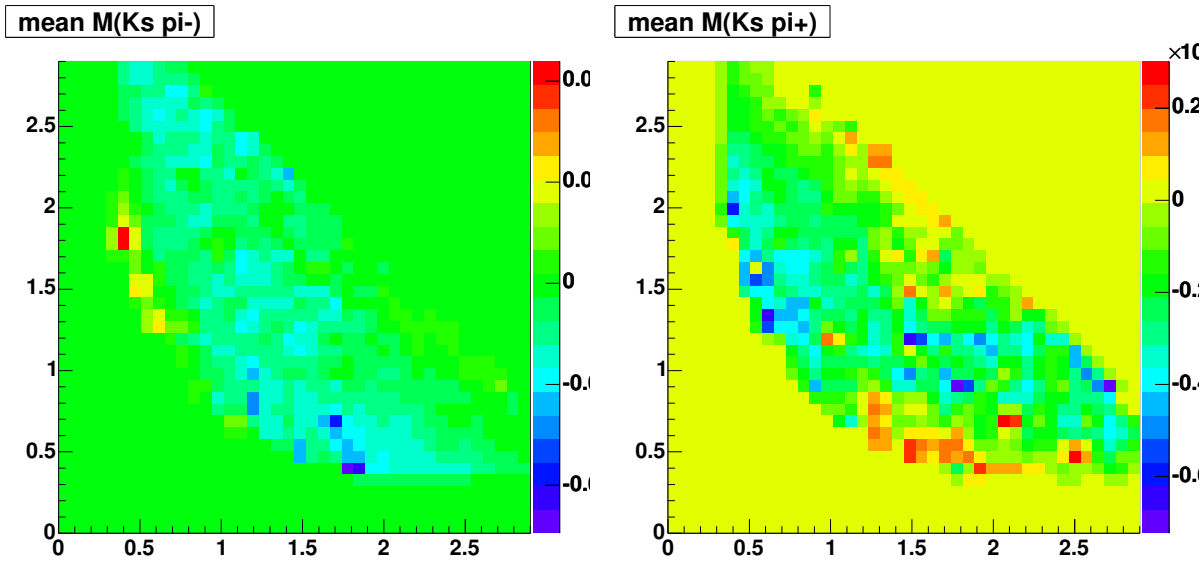


(a) $M^2_{K_S\pi^-}$ shift

(b) $M^2_{K_S\pi^+}$ shift

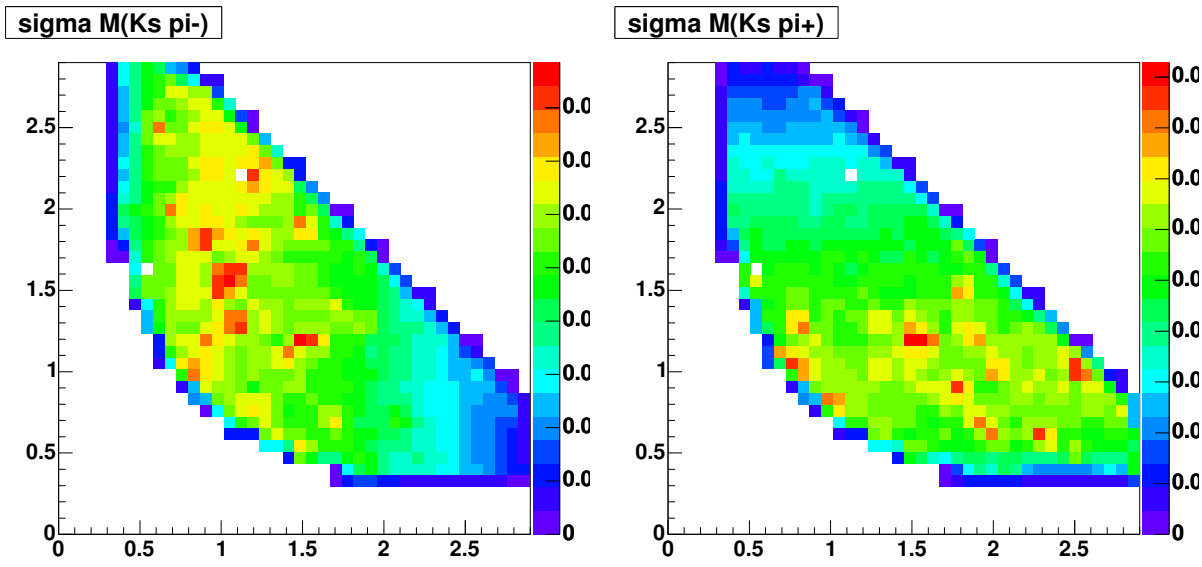


(c) $M^2_{K_S\pi^-}$ width

(d) $M^2_{K_S\pi^+}$ width

Figure 3.10: *Shift and the width of the resolution function as function of the Dalitz plot.*

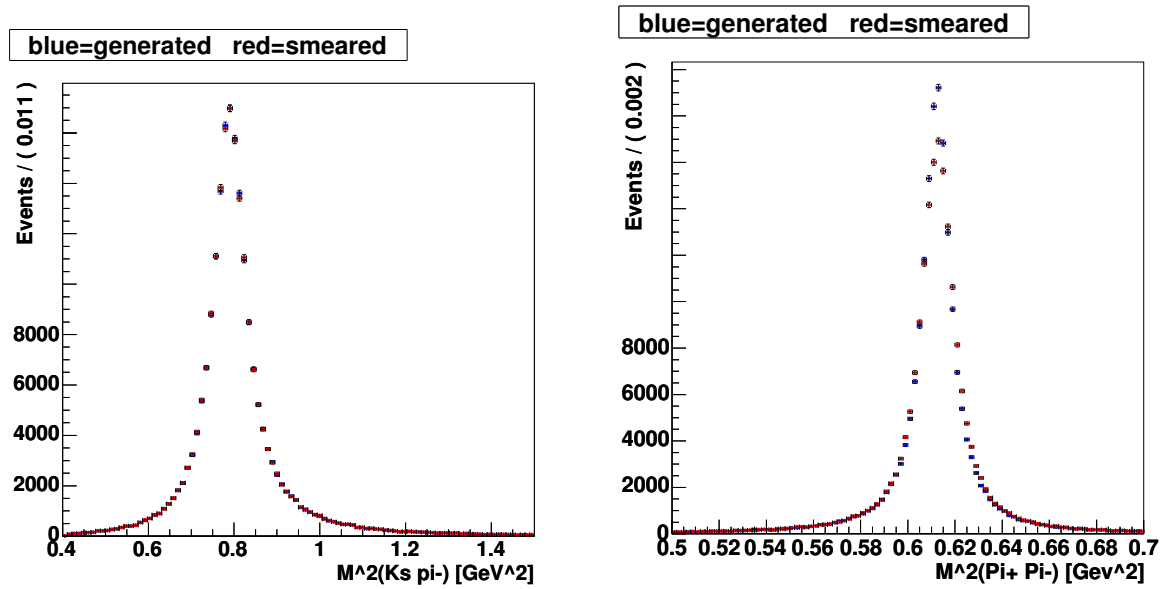


(a) $K^*(892)$ (b) $\omega(782)$

Figure 3.11: *Distribution of the generated* $K^*(892)$ *and* $\omega(782)$*sample (blue points) and smearing one (red points).*

distribution.

### 3.2.1 Decay Amplitude

The Dalitz plot distribution $(m_{12}, m_{13})$ is fitted using the Breit Wigner model [42] that uses the formalism of the *isobar* model. In this formalism, the decay amplitude $f$ can be written as a sum of two body matrix elements and a non-resonant term according to the following expression:

$$f = a_0 e^{i\phi_0} + \Sigma a_r e^{i\phi_r} \mathcal{A}_{\text{spin}}(ABC|r) \ . \tag{3.5}$$

Where $A$, $B$ and $C$ are referred to the $D^0 \to ABC$ decay through an $AB$ resonance $r$ (Fig. 3.12). The first term is the three body non-resonant term and the sum is over the contributions from the intermediate two body resonances. The form factors $\mathcal{A}_{\text{spin}}(ABC|r)$ are the usual Breit-Wigner terms.

For a spin zero resonance:

$$\mathcal{A}_0(ABC|r) = F_D F_r \frac{1}{M_r^2 - M_{AB}^2 - iM_r\Gamma_{AB}} \ , \tag{3.6}$$

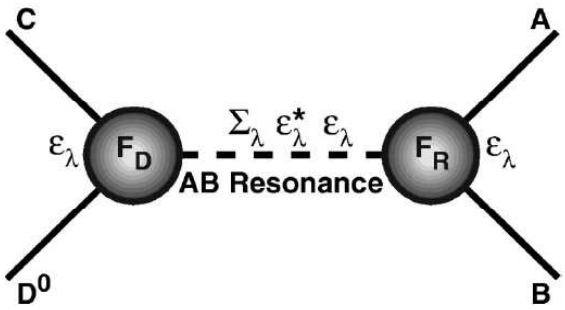


Figure 3.12: *Representation of the three-body decay of $D^0 \to ABC$ through an AB resonance. The spin sum is performed to obtain the angular dependence of the decay.*

where $M_r$ is the mass of the resonance and $M_{AB}$ the AB invariant mass. For a vector resonance:

$$\mathcal{A}_1(ABC|r) = F_D F_r \frac{M^2_{AC} - M^2_{BC} + \frac{(M^2_D - M^2_C)(M^2_B - M^2_A)}{M^2_r}}{M^2_r - M^2_{AB} - iM_r\Gamma_{AB}} \ . \tag{3.7}$$

Similar expressions hold for tensor particles:

$$\mathcal{A}_2(ABC|r) = \frac{F_D F_r}{M^2_r - M^2_{AB} - i\Gamma_{AB}M_r} \left[ \left( M^2_{BC} - M^2_{AC} + \frac{(M^2_D - M^2_C)(M^2_A - M^2_B)}{M^2_r} \right)^2 \right]$$

$$-\frac{1}{3}\left( M^2_{AB} - 2M^2_D - 2M^2_C + \frac{(M^2_D - M^2_C)^2}{M^2_r} \right) \left( M^2_{AB} - 2M^2_A - 2M^2_B + \frac{(M^2_A - M^2_B)^2}{M^2_r} \right) \Bigg] \ . \tag{3.8}$$

Here, $\Gamma_{AB}$ is a function of the mass $M_{AB}$, the momentum $p_{AB}$ of either daughter in the $AB$ rest frame, the momentum $p_r$ of either daughter in the resonance rest frame, the spin $J$ of the resonance, and the width $\Gamma_r$ of the resonance. The explicit expression is:

$$\Gamma_{AB} = \Gamma_r \left( \frac{p_{AB}}{p_r} \right)^{2J+1} \left( \frac{M_r}{M_{AB}} \right) F_r^2 \ . \tag{3.9}$$

For $\pi\pi$ vector resonances ($\rho(770)$ and $\rho(1450)$) the Gounaris-Sakurai (GS) Breit-Wigner parameterization [43] is used.

The form factors $F_D$ and $F_r$ attempt to model the underlying quark structure of the $D^0$ meson and the intermediate resonances. The Blatt-Weisskopf penetration factors shown in Tab. 3.1 are used. The one free parameter $R$ represents the "radius" of the meson and depends on the momentum $p_r$ of the decay particles in the parent rest frame. $F_D = 1$ for the $D^0$ and $R = 1.5$ GeV$^{-1}$ for the intermediate resonances are assumed.

| Spin | Form Factor $F_r$ |
|---|---|
| 0 | 1 |
| 1 | $\frac{\sqrt{1+R^2p_r^2}}{\sqrt{1+R^2p_{AB}^2}}$ |
| 2 | $\frac{\sqrt{9+3R^2p_r^2+R^4p_r^4}}{\sqrt{9+3R^2p_{AB}^2+R^4p_{AB}^4}}$ |

Table 3.1: *Summary of the Blatt-Weisskopf penetration form factors.*

### 3.2.2 Fit results

An unbinned maximum likelihood fit is made in order to describe the population on the Dalitz plot and to extract amplitudes $a_{nr}, a_j$ and phases $\phi_{nr}, \phi_j$. The likelihood function is written in the following way:

$$L = x \cdot \frac{\epsilon(m_\pm^2, m_\mp^2) \left| f(m_\pm^2, m_\mp^2) \right|^2}{\int \left| f(m_\pm^2, m_\mp^2) \right|^2 \epsilon(m_\pm^2, m_\mp^2) d\mathcal{DP}} + (1 - x) \ , \tag{3.10}$$

where $1 - x$ is the fraction of background events in the sample whose distribution is assumed to be flat and $\epsilon(m_\pm^2, m_\mp^2)$ is the efficiency map determined in Monte Carlo simulation where the $D^0$ was allowed to decay isotropically. The mass resolution effect is found to be negligible all over the Dalitz plane if compared with intermediate resonance width.

The fit fraction is defined as the integral of a single component divided by the coherent sum of all components:

$$\text{Fit Fraction} = \frac{\int \left| a_r e^{i\phi_r} \mathcal{A}(ABC|r) \right|^2 d\mathcal{DP}}{\int \left| \sum_j a_j e^{i\phi_j} \mathcal{A}(ABC|j) \right|^2 d\mathcal{DP}} \ , \tag{3.11}$$

where $d\mathcal{DP}$ indicates that the integral is performed over the Dalitz Plot. The sum of the fit fractions for all components of a fit will in general not be one because of interference.

For fitting the Dalitz plot a model with twelve resonances is considered. This model is described by the masses and widths listed in the PDG [41] (see Tab. 3.2). This leads to 18 two body decay amplitudes and phases, eight of which are $K_S + \pi\pi$ with $\pi\pi = \sigma$, $\rho^0(770)$, $\omega(782)$, $f_0(980)$, $\sigma'$, $f_2(1270)$, $f_0(1370)$, and $\rho(1450)$; five are $K_S\pi^- + \pi^+$ with $K_S\pi^- = K^*(892)$, $K_0^*(1430)$, $K_2^*(1430)$, $K^*(1410)$, and $K^*(1680)$; and three are $K_S\pi^+ + \pi^-$ with $K_S\pi^+ = K^*(892)$, $K_0^*(1430)$, and $K_2^*(1430)$.

All the considered resonances are well established but the two scalar $(\pi, \pi)$ resonances $\sigma$ and $\sigma'$, which were proposed by Belle [44]. The masses and widths of these two scalars have been obtained from a fit with all phases and amplitudes floated together with the masses and widths of the two resonances. Since there is an arbitrary overall normalization factor and phase, the $K_S\rho$ mode is chosen as reference and its amplitude is set to unity and phase to zero.

Tab. 3.3 gives the result of the Breit-Wigner Dalitz fit. Fig. 3.13 and Fig. 3.14 show the Dalitz distribution of the single resonances of the Breit-Wigner model. Fig. 3.15 shows projections of the fit result on top of data distributions and Fig. 3.16 shows zoom of particular regions of the Breit-Wigner fit result.

## 3.3 K-Matrix fit

It is well-known that the Breit-Wigner model is only suitable for relatively narrow and isolated resonances. The treatment of $S$-wave states in $D^0 \to K_S\pi^-\pi^+$ requires a more general formalism to account for non-trivial dynamics due to the presence of broad, overlapping resonances. The $K$-matrix approach, described in detail in Sec. 1.5 can be applied to the case of resonance production in multi-body decays when the two-body system in the final state is isolated, and the two particles do not interact simultaneously with the rest of the final state in the production process. In addition, it provides a direct way of imposing the unitarity constraint that is not guaranteed in the case of the Breit-Wigner model. Therefore, the $K$-matrix method is suited to the study of broad and overlapping resonances in multi-channel decays, solving the main limitation of the Breit-Wigner model to parameterize the $\pi\pi$ S-wave states in $D^0 \to K_S\pi^-\pi^+$ [45], and avoiding the need to introduce the two $\sigma$ scalars.

### 3.3.1 Decay Amplitude

The Dalitz amplitude $\mathcal{A}_D(m_-^2, m_+^2)$ is written in this case as a sum of two-body decay matrix elements for the spin-1, spin-2 and $K\pi$ spin-0 resonances (as in the Breit-Wigner model), and the $\pi\pi$ spin-0 piece denoted as $F_1$ is written in terms of the $K$-matrix:

$$\mathcal{A}_D(m_-^2, m_+^2) = F_1(s) + \Sigma_{r\neq\pi\pi\,\mathrm{S-wave}} a_r e^{i\phi_r} \mathcal{A}_r(m_-^2, m_+^2) \ , \tag{3.12}$$

| Resonance | Mass (MeV/c$^2$) | Width (MeV/c$^2$) | Spin |
|---|---|---|---|
| $K^*(892)$ | 891.66 | 50.8 | 1 |
| $K_0^*(1430)$ | 1412 | 294 | 0 |
| $K_2^*(1430)$ | 1425.6 | 98.5 | 2 |
| $K^*(1410)$ | 1414 | 232 | 1 |
| $K^*(1680)$ | 1717 | 322 | 1 |
| $\sigma$ | $484 \pm 9$ (from fit) | $383 \pm 14$ (from fit) | 0 |
| $\rho^0(770)$ | 775.8 | 146.4 | 1 |
| $\omega(782)$ | 782.6 | 8.5 | 1 |
| $f_0(980)$ | 975 | 44 | 0 |
| $\sigma'$ | $1014 \pm 7$ (from fit) | $88 \pm 13$ (from fit ) | 0 |
| $f_2(1270)$ | 1275.4 | 185.1 | 2 |
| $f_0(1370)$ | 1434 | 173 | 0 |
| $\rho(1450)$ | 1406 | 455 | 1 |

Table 3.2: *Values for the masses and widths of the resonances used for the fit of the* $D^0 \to K_s\pi^-\pi^+$ *Dalitz plot. The flavor tagged D sample from the continuum :* $D^{*\pm} \to D^0\pi_s^\pm$ *are used. The values and the width for the two scalars* $\sigma$ *and* $\sigma'$ *are obtained floating them in the fit, while the other are fixed according to the PDG2004 [41] values.*

| Resonance | Amplitude | phase (degrees) | fit fraction (%) |
|---|---|---|---|
| $K^*(892)$ | $1.777 \pm 0.018$ | $131.0 \pm 0.81$ | 58.51 |
| $\rho^0(770)$ | 1 (fixed) | 0(fixed) | 22.33 |
| $K^*(892)$ DCS | $0.1789 \pm 0.0080$ | $-44.0 \pm 2.4$ | 0.59 |
| $\omega(782)$ | $0.0391 \pm 0.0016$ | $114.8 \pm 2.5$ | 0.56 |
| $f_0(980)$ | $0.469 \pm 0.011$ | $213.4 \pm 2.2$ | 5.81 |
| $f_0(1370)$ | $2.32 \pm 0.31$ | $114.1 \pm 4.4$ | 3.39 |
| $f_2(1270)$ | $0.915 \pm 0.041$ | $-22.0 \pm 2.9$ | 2.95 |
| $K_0^*(1430)$ | $2.454 \pm 0.074$ | $-7.9 \pm 2.0$ | 8.37 |
| $K_0^*(1430)$ DCS | $0.350 \pm 0.069$ | $-344. \pm 10.$ | 0.60 |
| $K_2^*(1430)$ | $1.045 \pm 0.045$ | $-53.1 \pm 2.6$ | 2.70 |
| $K_2^*(1430)$ DCS | $0.074 \pm 0.038$ | $-98 \pm 30$ | 0.01 |
| $K^*(1410)$ | $0.524 \pm 0.073$ | $-157 \pm 10$ | 0.39 |
| $K^*(1680)$ | $0.99 \pm 0.31$ | $-144 \pm 18$ | 0.35 |
| $\rho(1450)$ | $0.554 \pm 0.097$ | $35 \pm 12.$ | 0.28 |
| $\sigma$ | $1.346 \pm 0.044$ | $-177.5 \pm 2.5$ | 9.11 |
| $\sigma'$ | $0.292 \pm 0.025$ | $-206.8 \pm 4.3$ | 0.98 |
| Non resonant | $3.41 \pm 0.48$ | $-233.9 \pm 5.0$ | 6.82 |

Table 3.3: *Amplitudes, phases and fit fraction of the different components obtained from the likelihood fit of the* $D^0 \to K_s\pi^-\pi^+$ *Dalitz plot. The flavor tagged D sample from the continuum :* $D^{*-} \to D^0\pi_s^\pm$ *are used. The total fit fraction is* 1.24.

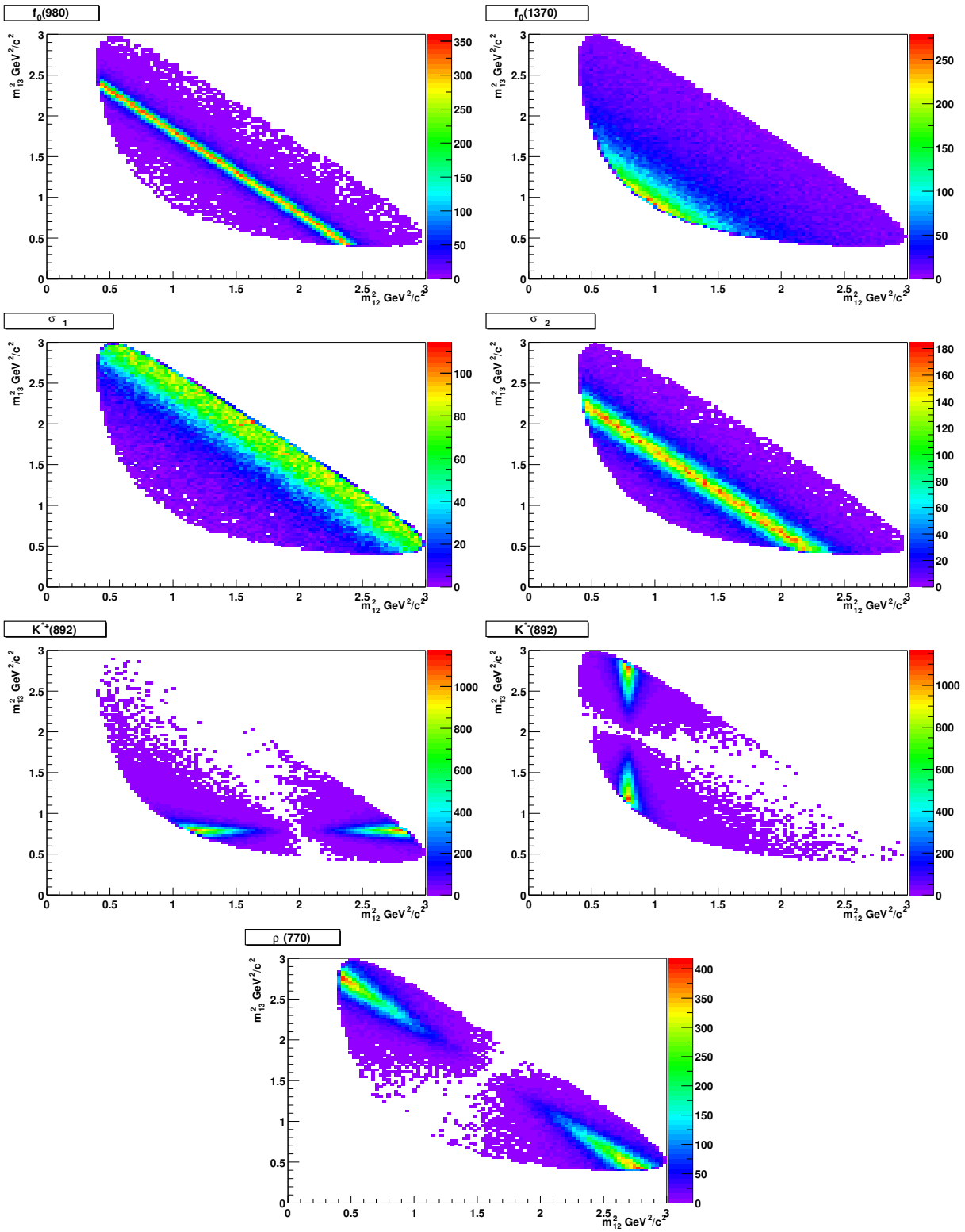


Figure 3.13: *Distribution of* $(m^2_{K_S\pi^+}, m^2_{K_S\pi^-})$ *for* $D^0$ *decaying into* $\pi\pi$ *S-wave* $K_S$*:* $f_0(980)$*,* $f_0(1370)$*,* $\sigma$*,* $\sigma$*', and* $K^{*-}(892)\pi^+$*,* $K^{*+}(892)$*[Doubly Cabibbo Suppressed],* $\rho(770)K_S$*.*

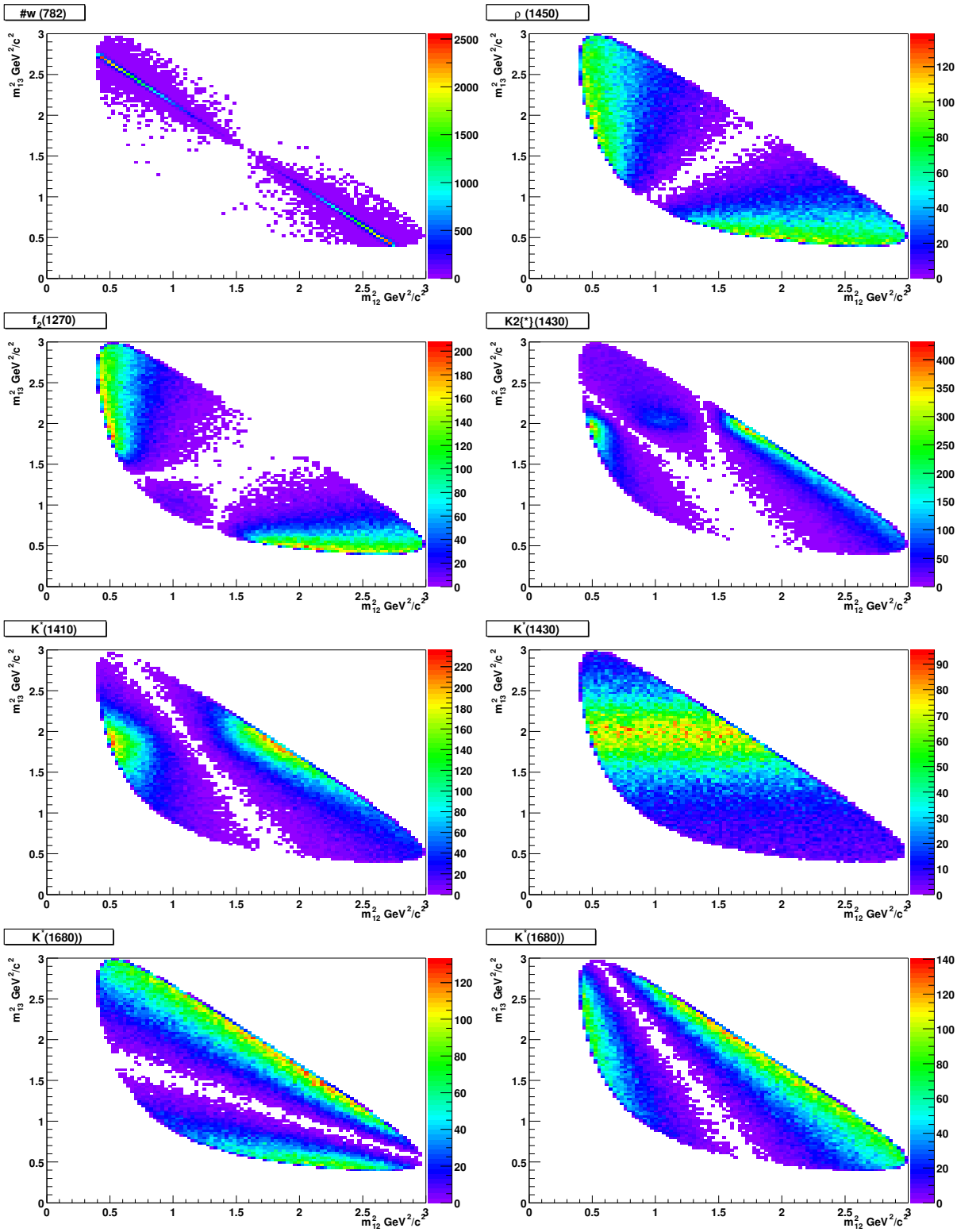


Figure 3.14: *Distribution of* ($m^2_{K_S\pi^+}$,$m^2_{K_S\pi^-}$) *for* $D^0$ *decaying into either* $\omega(782)K_S$, $\rho(1450)K_S$, $f_2(1270)K_S$, $K_2^{*-}(1430)\pi^+$, $K^{*-}(1410)\pi^+$, $K^{*-}(1430)\pi^+$, $K^{*-}(1680)\pi^+$ *or* $K^{*+}(1680)\pi^-$*[Doubly Cabibbo Suppressed decay].*

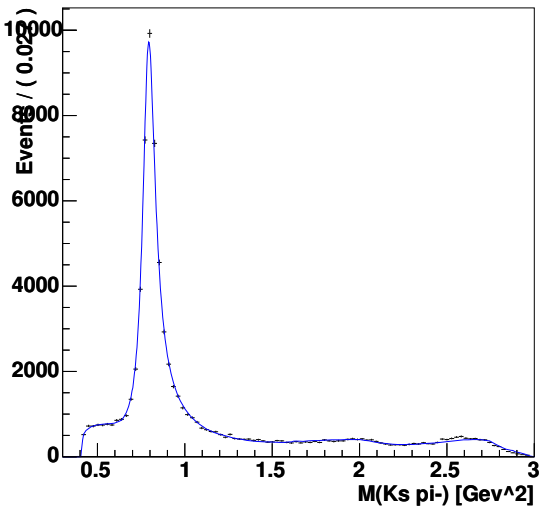


(a) $M^2_{K_S\pi^-}$

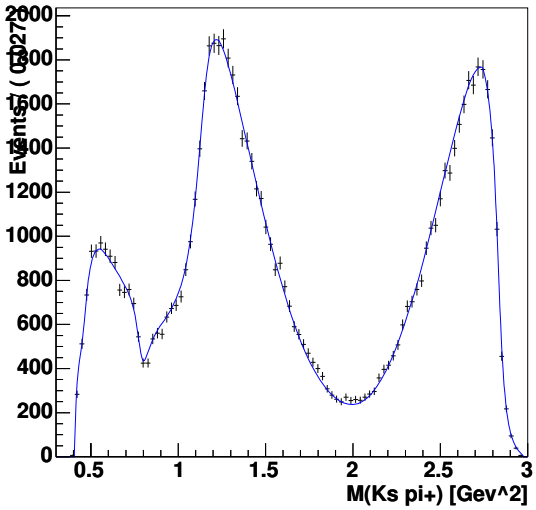


(b) $M^2_{K_S\pi^+}$

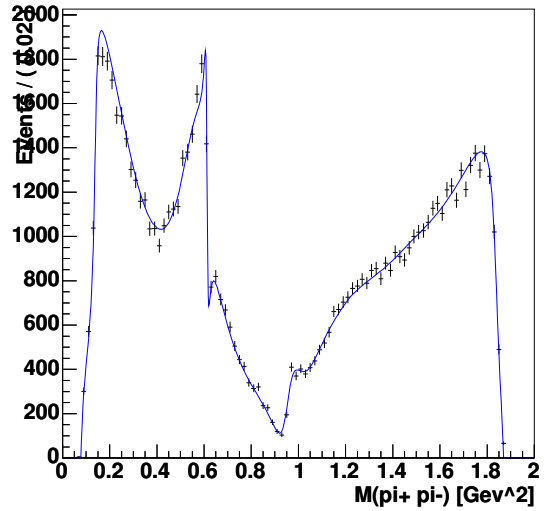


(c) $M^2_{pi^+\pi^-}$

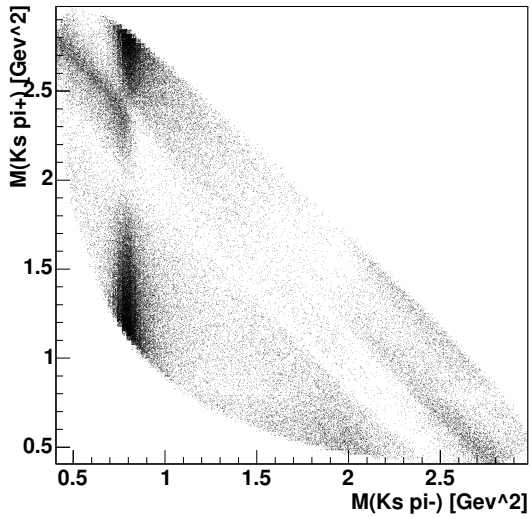


(d) Dalitz plot

Figure 3.15: *Result of the Breit-Wigner fit to the* $D^0 \to K_s\pi^-\pi^+$ *Dalitz plot, using the flavor tagged D sample from the continuum :* $D^{*\pm} \to D^0\pi^\pm_s$. *The three projections are displayed : Cabibbo allowed* $(K_s\pi^-)$, *the* $(K_s\pi^+)$ *and the* $(\pi^+\pi^-)$. *The Dalitz distribution of generated events according to the fit result is also shown.*